Ab initio modelling and experimental studies of order-disorder, hydration, and ionic conductivity of fluorite related oxides

Liv-Elisif Queseth Kalland

Dissertation for the degree of Philosophiae Doctor

Department of Chemistry
Faculty of Mathematics and Natural Sciences

UNIVERSITY OF OSLO

October 2020

Series of dissertations submitted to the
Faculty of Mathematics and Natural Sciences, University of Oslo
No. 2348

ISSN 1501-7710

Cover: Hanne Baadsgaard Utigard.
Print production: Reprosentralen, University of Oslo.

Preface

This thesis and dissertation represents part of the requirements for the degree of Philosophiae Doctor (Ph.D.) at the Department of Chemistry, Faculty of Mathematics and Natural Sciences, University of Oslo. The doctoral scholarship has been funded by the Norwegian Ministry of Education and Research, and the work carried out at the group for Solid State Electrochemistry (FASE) under the supervision of Prof. Truls E. Norby, Doctor Chris E. Mohn and Prof. Reidar Haugsrud.

Discussion and collaboration motivates me as it brings inspiration and new ideas, and I am utterly grateful to my three supervisors, for always having their door open for a short discussion and taking the time to listen and respond. This also goes to Andreas, Tor, Anna M., Einar, Ragnar, Shiyang, Matthias, the physicists and all others in the group, who never turned me down when I asked for a five minute discussion, on life or my research results, and offered me their reflections. You all inspired me, and created an encouraging work environment.

In addition, I want to express my gratitude to Chris Knee, for sharing his knowledge and introducing me to other peers, like Prof. Stephen Hull. Together they gave me important perspectives to guide me in my search for order within disorder on the boundary between short and long range order. I also want to acknowledge M. Sc. Jakob Kyrklund for the initial preparation of samples. I want to thank Prof. Saiful Islam for welcoming me to the University of Bath and teaching the theory and practical aspects of GULP. I am also grateful to Post doc Sandeep Gorantla and Prof. Anette Gunnæs from structure physics section at UiO, who took the time to perform HR-TEM investigations with me.

My family, friends, Xuemei and many from the group have offered comfort when needed, and I am grateful for the endless support. My current workplace, also deserve my gratitude for their flexibility and cheering the last years. Finally, I would especially like to thank my partner Kristian for being so patient and helping me through this long lasting period of finishing the thesis.

Liv-Elisif Queseth Kalland
Oslo, October 2020

Summary

In this thesis we investigate the structure of $La_{28-x}W_{4+x}O_{54+\delta}$ (x = 0, 1) and $La_{2-x}Nd_xCe_2O_7$ (x = 0, 0.5, 1, 1.5 and 2) and the ionic conductivity and hydration, which are defect related properties of $La_{2-x}Nd_xCe_2O_7$. The underlying goal is to strengthen the understanding of oxides with fluorite related structure, with respect to the main energetic contributions to transport properties and the hydration thermodynamics.

$La_2Ce_2O_7$ has previously been shown to exhibit pure ionic conductivity with contribution of proton conductivity at low temperatures, and $La_{28-x}W_{4+x}O_{54+\delta}$ show high proton conductivity at intermediate to high temperatures. However, the classic hydration model on the average structure determined by diffraction has failed to provide reasonable explanations for the observed water uptake and conductivity. By combining first principles calculations and a number of experimental techniques, we show how the local structure defines frameworks for the defect chemistry, and provide models that can rationalize the experimentally obtained results.

In the two first manuscripts/papers we have conducted a structural investigation of the two defective fluorites $La_2Ce_2O_7$ and $Nd_2Ce_2O_7$ and their intermediate phases when replacing La with Nd. In Paper I, "C-type related order in the defective fluorites $La_2Ce_2O_7$ and $Nd_2Ce_2O_7$ studied by neutron scattering and *ab initio* MD simulations", we focus on the average crystal structure and identify a compatible local structure. We perform X-ray and total scattering neutron powder diffraction and the diffraction data is analysed using Rietveld and reversed Monte Carlo method (RMC). We further construct atomic distribution functions from *ab initio* molecular dynamics (MD) results for different configurations to compare with the functions obtained by neutron total scattering. We find that $La_2Ce_2O_7$ is best refined as a disordered fluorite, but due to increasing intensity of additional C-type supercell peaks in the powder neutron diffraction (PND) data with increasing x in $La_{2-x}Nd_xCe_2O_7$, the Nd-containing compounds were best fitted using a combination of oxygen deficient fluorite and oxygen excess C-type structures. *Ab initio* molecular dynamics results confirm that oxygen vacancy order comparable to that in the C-type structure, is a plausible ordering scheme explaining the observed long range order. The results from MD modelling suggest that C-type related ordering might also be found in $La_2Ce_2O_7$, which is supported by the PND data. The Rietveld refinements indicate that the C-type superlattice peaks stem from domains with long range vacancy ordering. Further

evidence for this is given using HR-TEM (high resolution transmission electron microscopy).

In Paper II, "First principles calculations on order and disorder in $La_2Ce_2O_7$ and $Nd_2Ce_2O_7$", we explore the local structure by comparison of a large number of configurations in the static limit, and from Born-Oppenheimer Molecular dynamics calculation using density functional theory (DFT). C-type related ordering of the oxygen vacancies reduce the energy for both compounds, and the ordering is largely independent of how the cations are arranged in the configuration. The ordering is identified by a high fractions of <210> vacancy pairs which is optimized when combining <110> and <111> vacancy pairs in ordered patterns. As discussed in this thesis long range ordering results in even distribution of vacancies, ensuring a relatively cubic oxygen sublattice and cation coordination numbers between 6 and 8.

Computationally we find C-type related ordering to be favourable for both $La_2Ce_2O_7$ and $Nd_2Ce_2O_7$, but experiments show significant differences in the extent of ordering. To resolve this apparent contradiction, the summarizing discussion proposes that the vibrational and configurational entropy contributions in the Gibbs energy of the systems be different based on different lattice constant for the two compounds. Stabilization of disorder to quite low temperatures could rationalize the observed extent of ordering, and the degree of ordering is expected to increase with decreasing temperatures. We further support this by analysing the temperature dependence of the activation energy of oxide ion conductivity in the summarizing discussion. Partial vacancy order and disorder at diffraction temperatures, is proposed explained due to equilibrium concentrations of ordered vacancies or frozen-in disorder due to kinetic limitations.

In Paper III, "Structure, hydration, and proton conductivity in 50% La and Nd doped CeO_2 – $La_2Ce_2O_7$ and $Nd_2Ce_2O_7$ – and their solid solutions", we use TG-DSC and electrical conductivity measurements to investigate the hydration properties and the proton conductivity of $La_{2-x}Nd_xCe_2O_7$. The high amount of vacancies leads to a potential of 1 mol H_2O uptake per mole $La_{2-x}Nd_xCe_2O_7$. However, we find the hydration is strongly limited with respect to the expected potential, even in 1 atm of water. The limited water uptake is explained by two models. First we identify long range ordering of vacancies to restrict the effective concentration of available, or "free", vacancies that can be hydrated in order to explain the evolving decrease in water uptake with increasing Nd^{3+} content. Secondly, we propose a model for the disordered domains of $La_{2-x}Nd_xCe_2O_7$, where protons associate to the statistical number of fully acceptor-coordinated oxide ions, due to the higher basicity of La^{3+} and Nd^{3+} compared to Ce^{4+}. The basicity of La and Nd thus enables hydration in the heavily doped ceria, and in the summarizing discussion we further argue that proton trapping is the main contribution to the hydration enthalpy. As such, the trapping also

impose a site restriction for protons, creating a limitation on the maximum amount of hydration. This second model obtains a good fit to the mainly disordered $La_2Ce_2O_7$.

In Paper IV, "Local Structure of Proton-Conducting Lanthanum Tungstate $La_{28-x}W_{4+x}O_{54+\delta}$: a Combined Density Functional Theory and Pair Distribution Function Study", we present the local nature of the most stable compounds within the cubic fluorite structure. We use classical force field calculations and first principles to study the local structure. Similar to the method used in the first paper, we compare pair distribution functions based on first principles calculations and from total scattering neutron diffraction.

The computational study of $La_{28-x}W_{4+x}O_{54+\delta}$ for $x = 0$ and 1, shows that strongly bonded and regular WO_6 polyhedra result in strong local ordering of two vacancies coordinating tungsten. This results in only a small part of the vacancies to be considered as charged defects available for diffusion and hydration. We further establish that the excess tungsten in $La_{27}W_5O_{55.5}$ will be situated on the La site that shares oxide ions with the cations on the W specific site. As such, the additional WO_6 polyhedra are corner sharing with the WO_6 polyhedra in W sites. The reduced vacancy concentration resulting from W self-doping limits the effective concentration of free vacancies, and the additional WO_6 polyhedra influence the direction of the two connected tungsten polyhedra, limiting the rotation and transport of oxygen. The structural model of $La_{28-x}W_{4+x}O_{54+\delta}$ is used to explain experimental observations from literature.

In the discussion of this thesis, the modelled and observed vacancy ordering is connected to the observation of defect related properties. Similarities and differences between the studied compounds are highlighted, and from this, possible trends describing how structural properties, ionic conductivity and hydration change for the compounds are identified.

Table of Contents

1 Introduction

"The more I learn, the more I realize how much I don't know."

— Albert Einstein

Over the last decade, proton conducting oxides have gained massive interest as promising candidates for next-generation materials in electrochemical devices for energy conversion and storage [1, 2]. These materials exhibit properties that could drastically reduce cost and increase durability in several electrochemical applications important for the hydrogen economy. Hydrogen will play a key role in developing a carbon neutral and carbon negative society. Hydrogen can function as a fuel for the transport sector, either as pure H_2 or though hydrogen carriers such as ammonia or liquid organic hydrogen carriers (LOHC). Energy conversion of electricity into hydrogen, and vice versa, can contribute with flexibility in renewable energy production to manage large peak variations. Hydrogen is also an important factor for upgrading bio-oils or CO_2 into hydrocarbons, necessary in order to produce fuels or other carbon-containing products such as plastics. Green carbon from biomass and CO_2 extracted from the atmosphere or from large point sources of emission (carbon capture and usage) are needed in order to mitigate the use of fossil factors to the petrochemical industry.

Proton conducting oxides can be used for a variety of electrochemical devices: proton ceramic fuel cells (PCFCs) for converting hydrogen to electricity, proton ceramic electrolysis cells (PCECs) for hydrogen production, ammonia synthesis or even co-conversion of CO_2 and H_2O, reversible protonic ceramic electrochemical cells (RePCEC) for energy conversion and grid-scale storage and protonic ceramic electrochemical reactors (PCERs) for natural gas upgrading [1-3].

Proton conducting oxides that conduct electrons or oxide ions as well as protons are called mixed conductors. Mixed conductors are applicable for electrodes in SOFCs[4], and mixed electronic-protonic conductors can be used as hydrogen gas separation membranes in addition to being candidates for PCFC electrodes [5]. Triple conducting oxides (electrons, oxide ions and protons) can function as cathode material for dual-ion SOFCs [6].

Hydrogen is the energy carrier with the highest energy density, and can be converted to electricity in a fuel cell without CO_2 emission. Fuel cells are classified according to the types of electrolytes and their major ionic charge carriers. In solid oxide fuel cells (SOFC) oxide ions or protons are transported through an oxide electrolyte due to a chemical potential gradient and an electric current is drawn over the cell. State-of-the-art oxide ion conductors offer the best ionic conductivities at high temperatures. However, proton conductors have higher ionic conductivity at low and intermediate temperatures. Today's proton exchange membrane (or polymer electrolyte membrane, PEM) fuel cells are commercialized for use in fuel cell electrical vehicles and small scale electricity generation from hydrogen. The PEM electrolyte, however, need high purity H_2 fuel to avoid fast degradation of the electrolyte. Proton conducting oxides, on the other hand, tolerate coking and contaminants better, making them more durable as well as suitable for different types of hydrogen-containing fuels [1-3]. Proton conducting ceramics also obtain higher efficiency in reversible electrochemical cells. In order for proton ceramic fuel cells to reach commercialization the large scale production methods must be developed in order to reduce the cost of production, and more efficient electrode materials must be developed [1].

The state-of-the-art proton conductors known today are doped ABO_3 perovskites with Ba for the A site and Ce and-or Zr for the B site nominally [1-3, 7-9]. These materials absorb protons through a hydration reaction creating hydroxide defects. This is an exothermic reaction that creates a limitation to the temperature range in which protons will be present, due to dehydration [7]. Doping (usually acceptor doping) of these materials can in most cases increase the concentration of vacancies, and subsequently protons upon hydration.

Zirconia and ceria based oxides but with the fluorite structure, yield state-of-the-art solid oxide ion conductors such as yttria stabilized zirconia (YSZ) and Gadolinium doped ceria (GDC) [10, 11]. High oxide ion diffusion upon doping with alkaline earth oxides or rare earth oxides is enabled by their high tolerance for disorder. Doped ceria and YSZ exhibit high oxide ion conductivity but show no or little proton conductivity in the bulk, only surface proton conductivity at room temperatures [12, 13]. However, heavily La doped ceria (i.e. $La_2Ce_2O_7$) has shown significant bulk proton conductivity at low to intermediate temperatures making it an interesting proton ceramic conductor [14-16]. La_6WO_{12} is another fluorite derived compound that has harvested interest due to its relatively high and predominate proton conductivity at intermediate to high temperatures, in addition to its mixed electronic-protonic conductor properties [17-19].

Status and motivation

In the search for new oxide materials for electrochemical devices we encounter different challenges in understanding the underlying principles of the materials chemistry. For some oxides, more basic properties like crystal structure and atomic ordering are also not yet

determined. These properties are closely related to the defect chemistry of oxides. Understanding the defect structure and investigating thermodynamic equilibria between different defects in proton conducting oxides, are important to gain knowledge that can be used to further improve material properties such as ionic conduction through doping and specialized synthesis methods.

The main goal of the work presented in this thesis is to strengthen the understanding of fluorite related oxides that can be considered highly oxygen deficient with respect to the perfect fluorite structure. The structure and defect structure are keys to the properties of oxides. The structures of some fluorite related oxides exhibiting oxide ion and proton conductivity, La_6WO_{12} (or in reality $La_{28-x}W_{4+x}O_{54+\delta}$ with $0.74 \leq x \leq 1.08$) and $Ln_2Ce_2O_7$ (Ln = La and/or Nd) are the focus. The compounds cannot be described by means of the average structure models available in the current literature, particularly for the oxygen environment and a disordered oxygen sublattice. The compounds possess cubic fluorite derived structures which are highly oxygen deficient with respect to the fluorite structure (i.e. high oxygen vacancy concentration). The understanding of when the compound exhibits defects in the dilute regime, defect association or short or long range order, is important to understanding the physical properties of the compound such as hydration, ionic conductivity and phase stability. Through experimental and computational methods we investigate the structure, hydration and ionic conductivity of these compounds.

$La_2Ce_2O_7$ and $Nd_2Ce_2O_7$

Conductivity measurements on $La_2Ce_2O_7$ [14-16] indicate pure ionic conductivity. The oxide ion conductivity is high at elevated temperatures, almost comparable to the state-of-the-art oxide ion conductors YSZ and GDC, and proton conductivity is found at lower temperatures. This raises the question of why $La_2Ce_2O_7$ shows significant proton conductivity when moderately doped ceria does not. The question further leads to the question of whether $La_2Ce_2O_7$ (and $Nd_2Ce_2O_7$) is best described as heavily doped ceria, a solid solution or an oxide with its own perfect crystal structure. Additional acceptor doping of $La_2Ce_2O_7$ with calcium, decreases the conductivity. Self-compensation with over-stoichiometry of cerium is suggested to be the reason, together with precipitation of La_2O_3 [20]. Another possible explanation is trapping of oxygen vacancies by the acceptor dopants or ordering of vacancies. Earlier studies on the related compound $Nd_2Ce_2O_7$, which has somewhat lower ionic conductivity than $La_2Ce_2O_7$, show indications of some long range ordering of vacancies in otherwise disordered fluorite structure [21-24]. However, the physical origin of the supercell diffraction peaks in $Nd_2Ce_2O_7$ is yet not fully understood. For $La_2Ce_2O_7$, however the debate has been whether pyrochlore structured $La_2Ce_2O_7$ will be formed [25, 26], or whether it will be a disordered fluorite [14, 27, 28]. It follows that

these two compounds are on the stability border between the pyrochlore, disordered fluorite and C-type structure.

Density functional theory (DFT) is an *ab initio* or first-principles, computational method which provides a powerful tool for determining the structural energy landscape. In this work, computational as well as experimental structure investigations will be presented, aiming to determine the order and disorder within the crystal structure. Ionic conductivity and hydration of the oxides are studied experimentally and correlated to the information on the atomic structure. The combined data is used to develop a full structural model that can explain the observed properties of $La_{2-x}Nd_xCe_2O_7$ (with x = 0, 0.5, 1, 1.5, and 2).

Crystal structure refinement of La_6WO_{12}

As previously mentioned, La_6WO_{12} exhibits high temperature proton conductivity. The crystal structure and stability range of lanthanum tungstate has been investigated with neutron diffraction prior to this work revealing the true stoichiometry to be $La_{28-x}W_{4+x}O_{54+\delta}$ (with $0.74 \leq x \leq 1.08$), within a cubic fluorite related structure [29]. The findings, however, leave some questions regarding the defect chemistry as to where the excess tungsten resides and why the hydration conductivity properties were limited with respect to the refined structure, which predicted about 1 out of 6 oxygen positions to be vacant [17, 30]. Through classical force field calculations with empirical pair potentials, we further investigate the crystal structure of $La_{28-x}W_{4+x}O_{54+\delta}$. Computational studies using simple atomistic calculations of the lattice energy have lower computational costs compared to first-principles techniques such as DFT. This opens up the possibility of studying large systems in the search for superstructures and good sampling of different structural configurations. The results form the basis for further and more accurate DFT-calculations in this study, which in turn are compared with neutron total scattering and the resulting pair distribution function. By altering the configurations we can also interpret facets of the experimentally obtained diffraction data.

2 Theory and background

"If I have seen further it is by standing on the shoulders of Giants."

— Isaac Newton

In this chapter, some of the basic principles and underlying theory of this work will be described together with literature relevant for this thesis. In addition, some connections to general methods will be drawn.

2.1 Crystal structures

In the work with crystalline materials and their material properties, it is alpha and omega to know and understand the crystal structure and the thermodynamics, since all physical and chemical properties can be understood through their thermodynamic states and equilibria. Therefore we will start with looking at the theory of perfect crystals and some relevant crystal structures for this work.

Perfect crystals and the ground state

A perfect crystal has perfect ordering of atoms in the lattice of the atoms and perfect translational symmetry (and of course no defects). If a crystal is perfect, the crystal (i.e. physical system) is in its one unique state (i.e. crystal structure) where it has the lowest possible energy. This is called the ground state and the third law of thermodynamics reveals that it will have zero entropy, S, at absolute zero degrees (0 K). If the system is not able to reach this equilibrium at 0 K, it will be frozen-in at another state or in other words a meta-stable structure. If there are several degenerate (i.e. having the same energy) states, the system has configurational entropy, and in principle, it is possible to have degenerate ground states, but this is rare for binary and ternary oxide compounds when looking only at the atomic structure. In this work a certain atomic structure or arrangement of the atoms in a crystal, is often referred to as a configuration. The system gains configurational entropy when other configurations are accessible due to available energy through increased temperature. In addition to the configurational entropy, crystalline compounds gain vibrational entropy when the temperature increases. The energy is related to the oscillating vibrations of atoms, which increase with temperature.

It is the ground state of a compound that atomistic simulation techniques are searching for when relaxing an atomic structure during energy minimization, either they are potential based models, simulating the potentials between atoms based on empirical values, or *first principles* calculations like DFT solving the Schrödinger equation including electrons using a functional of the electron density. Most atomistic simulation techniques entail iterative operations where the energy of the crystal (or molecule for non-crystalline materials) is calculated for a trial configuration. Then atoms are moved in small steps in different directions to see if the forces acting on the atoms or the total energy can be minimized. The energy gradients due to forces acting on the atoms tell the program where to continue its search for the configuration with a global minimum energy which is the ground state. If the computational method also calculates the electronic structure, the electron energy is minimized for each atomic step. The calculated energy for the resulting atomic (and electronic) structure is called the *total energy*. From the total energy, the change in enthalpy ΔH of reactions can also be calculated assuming constant pressure. For example, the formation enthalpy of an oxide can be found from the difference between the energy for the oxide and the energy of the constituents in their ground state (more about this later in Chapter 3 Methodology).

During synthesis crystals can get kinetically hindered from reaching the ground state structure when cooled down. The crystals are then frozen-in, in a meta-stable state. In a similar manner the infinite crystal simulated can be stuck in local minima. Therefore one has to search between in principle all possible structure candidates in some manner to be sure to succeed in reaching the global minimum. However, this would in turn demand significantly more computational effort and create a much more time-demanding calculation.

The atomic structure of the perfect crystal, the "ground state" or lowest energy configuration, is a central topic in this work defining properties we are interested in and serving as a starting point for calculations of defects. Before we look at relevant defects we will introduce the fluorite structure and superstructures of fluorites relevant for this work.

Crystal structure and the fluorite structure

Crystal structures describe the atom arrangements, and the smallest repeating pattern repeated infinitely in all directions is called the unit cell. The lattice constants describe the length and angles of the axis in the unit cell and the space group identifies the symmetry operations of the unit cell. The atomic positions are expressed in fractional coordinates within this cell, and due to symmetry, the sites in the unit cell are repeated according to the space group. These distinct sites are then reported using Wykoff sites. This type of structural information is the input and output for atomistic simulation techniques. There are several other ways of classifying a crystal structure than the space group, e.g. crystal families,

crystal systems and lattice systems. They all give a good impression of the lattice parameters, however space group is the classification scheme with most detailed information about the symmetry between the atomic positions.

The perfect fluorite structure is the basis of all the modelling of structure in this work, and CeO_2 is an example of a compound that exhibits this structure. The perfect fluorite structure has the space group Fm-3m and two Wyckoff sites 4a (0, 0, 0) and 8c (¼, ¼, ¼) for the cations and anions, respectively, which are fully occupied in CeO_2. Z = 4, meaning there are 4 formula units in the unit cell. The Bravais lattice and crystal family/lattice system for the fluorite structure is face-centred cubic. The term cubic, tells us the lattice parameter angles are all 90˚. The lattice parameters are a, b, and c = 5.4625 Å.

The lanthanides (Ln: La, […], Lu) and the rare earths (which in addition to Ln also include Y and Sc) with oxidation state 3+, adopt the A-type, B-type or C-type sesquioxides structure. Sesqui is latin and means 1.5 times referring to the 3:2 ratio of oxygen to cations. The binary oxides of the bigger rare earths such as La crystallize in the A-type crystal structure, and for the medium sized lanthanide the B-type will be found. The C-type structure is most stable for the sesquioxides formed by Gd and smaller rare earths. The A- B- and C-type are actually not closely related structurally, as they are hexagonal, monoclinic and cubic respectively. The C-type structure is, however, related to the perfect fluorite structure, it is a so-called super structure of fluorite.

Super structures of Fluorite; C-type and pyrochlore structure

There are several super structures that are derived from the perfect fluorite (see Figure 1 a-c). The cubic C-type structure (Ln_2O_3, space group Ia-3) has a higher symmetry, compared to the parent cubic perfect fluorite structure (see Figure 1 a)). Due to the lower oxygen stoichiometry in the c-type fluorite and the small cations favouring a 6-fold coordination, the parent 4a and 8c sites are split into two Wyckoff sites with the cations occupying 8b and 24d and the oxide ions occupying only 48e and not 16c. The unit cell is doubled in all directions correspondingly. The oxygen atoms, or rather the vacant sites, form a symmetrical pattern with ¼ <111> and ¼ <110> direction between the vacant 16c sites around the two cation sites 8b and 24d respectively (see Figure 2 d). Further, the next closest vacant site will have a ¼ <210> direction in this symmetry.

The pyrochlore structure, ($A_2B_2O_7$, space group Fd-3m), is also derived from the fluorite structure (see Figure 1c). Due to size mismatch and charge difference, the trivalent and tetravalent cation order into the different 16d and 16c sites. In addition the oxygen sublattice splits into the positions 8b, 48f and 8a, where the latter is vacant resulting in an 8-fold coordination of the trivalent A-cation and 6-fold coordination of the smaller tetravalent B-cation with the vacant oxygen sites aligned in the ¼ <111> direction (see Figure 1 e). Like

the C-type structure, the pyrochlore unit cell is therefore doubled in all crystallographic directions compared to the perfect fluorite unit cell (i.e. the lattice constant is doubled $a_{c\text{-}type/p\text{-}type} = 2*a_{f\text{-}type}$).

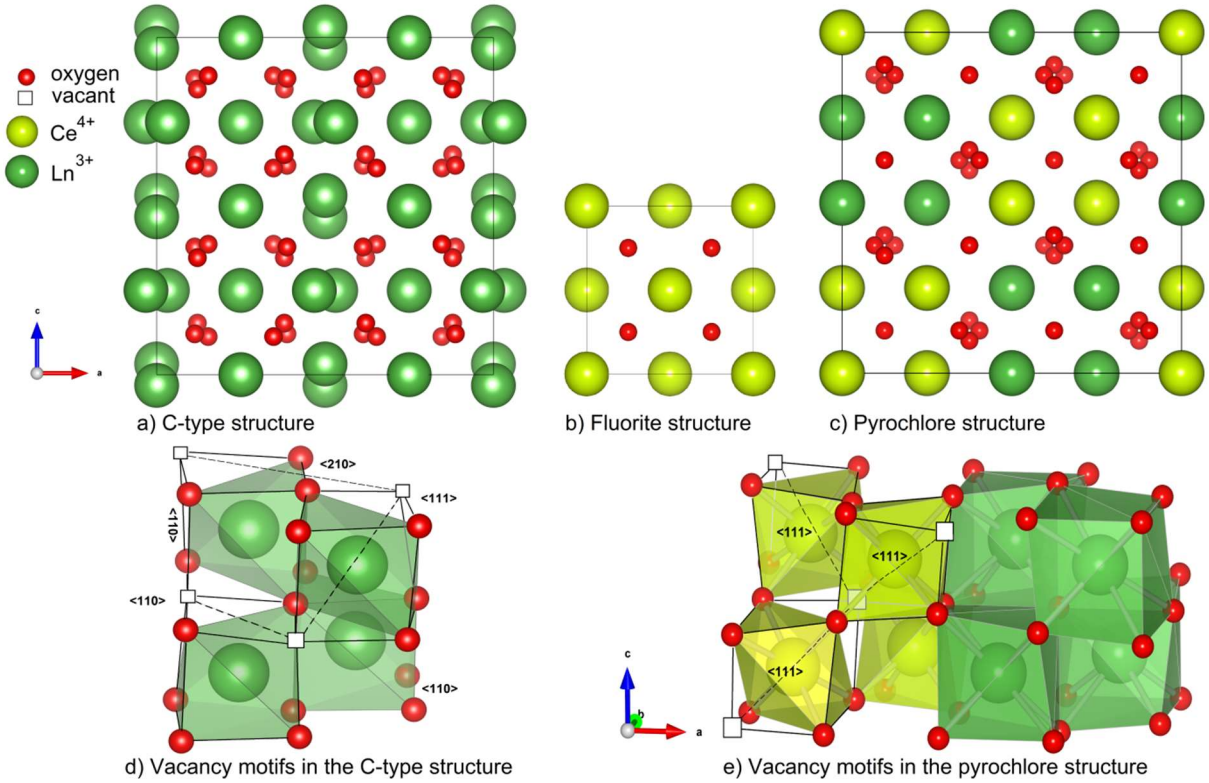

Figure 1 The a) c-type fluorite and c) p-type fluorite (pyrochlore) compared to the parent structure b) perfect fluorite, and the coordination polyhedron and vac-vac direction ¼ <111> and ¼ <110> in d) c-type fluorite and e) pyrochlore. (Modified from Paper I and II.)

In addition to these cubic super structures there are other related defect fluorite structures such as bixybite, weberite and several possible stoichiometric phases for lanthanides with varying oxidation states between 3+ and 4+ such as Pr_6O_{11}.

The vacancy alignments have until now in this thesis been described according to the unit cell size. In order to compare the same type of vacancy alignments in different structures with varying size of the unit cell we will from now refer to the vacancy pairs with respect to the oxygen cubes in the cubic fluorite structure (e.g. 4 <111> for the pyrochlore structure equals ½ <111> for the fluorite structure and is in this work denoted as only <111> like in figure 1 d) and e)).

2.2 Defects, hydration and thermodynamics

It is the point defects in the crystal structure that enable physical properties such as ionic and electronic conductivity, as well as hydration. The presence of oxygen vacancies in an oxide, for instance, usually enables oxide ion conductivity as well as hydration and subsequently proton conductivity. Understanding the defect chemistry of oxides is therefore important in this thesis.

Defects in oxides in fluorite related oxides

Defects form intrinsically, extrinsically, or they are incorporated into the structure by adding dopants or contamination. Intrinsic defects occur in charge compensating pairs as they involve the constituents present in the perfect crystal only and the compound remains stoichiometric. An example is anti-Frenkel defects often formed in pyrochlore structured oxides [27, 28, 31, 32], where an oxide ion swaps site to a nominally unoccupied Wykoff position. Using the Kröger-Vink notation [33], a typical anti-Frenkel defect in pyrochlores is written as:

$$v_{O\ 8a}^{x} + O_{O\ 48f}^{\times} = v_{O\ 48f}^{\bullet\bullet} + O_{int\ 8a}'' \qquad (1)$$

If this formation reaction is occurring spontaneously (i.e. is exothermic and $\Delta G < 0$), the defect structure is more stable than the perfects pyrochlore structure, and the pyrochlore structure is not the ground state. Minervini et al. predicted that $La_2Ce_2O_7$ will not exhibit the pyrochlore structure, since computational modelling found the formation of Frenkel and anti-Frenkel defects to be exothermic, causing cations and oxide ions to disorder [28]. In perfect crystals, formation of intrinsic defects is necessarily endothermic. Consequently, the concentration of oxygen vacancies formed in Equation (1) will increase with temperature.

Extrinsic reactions involve exchanging mass with the environment, e.g. releasing oxygen to the atmosphere forming pairs of ionic and electronic point defects. The electronic defects may be either delocalized or localized as cations, so called valence defects. The equilibrium depends on surrounding conditions; temperature and partial pressure. One example shown here, is reduction of ceria where oxygen vacancies charge compensate the reduced cerium ion, resulting in an oxygen deficient fluorite:

$$2Ce_{Ce}^{\times} + O_{O}^{\times} = 2Ce_{Ce}' + v_{O}^{\bullet\bullet} + \frac{1}{2}O_2(g) \qquad (2)$$

The concentration of these defects is rather small at ambient temperatures and pressures. By substituting in cations with lower valance for Ce^{4+}, the oxygen non-stoichiometry increases since oxygen vacancies charge compensate the dopant ions. The acceptor dopant

concentration will be constant provided that the concentration is below the solubility limit or frozen-in.

In the present work concerning $La_2Ce_2O_7$ and $Nd_2Ce_2O_7$ one may choose to regard these compounds as ceria substituted by trivalent lanthanides, i.e. as 50% acceptor doped ceria ($Ce_{1-x}Ln_xO_{2-0.5x}$ in the general form), in the Kröger-Vink notation:

$$Ln_2O_3 = 2Ln'_{Ce} + 3O_O^{\times} + v_O^{\bullet\bullet} \quad (3)$$

If a cation is substituted with a higher valent cation, the oxide is donor doped, and oxygen interstitials can be formed to charge compensate as they will have effectively negative charge. Self-donor doping occurs in another of the materials represented in this work, $La_{28-x}W_{4+x}O_{54+\delta}$:

$$WO_3 = W_{La}^{\bullet\bullet\bullet} + \frac{3}{2}O_O^{\times} + \frac{3}{2}O''_{int} \quad (4)$$

where the material is most stable at $0.74 \leq x \leq 1.08$ [30].

Defect thermodynamics

Defect formation and the thermodynamics of non-stoichiometric phases are analysed using the mass action law on quasi-chemical reactions like in Equation 1-4 and their quasi-chemical equilibrium constant, *K*. When writing defect equation one must take into account the three rules demanding conservation of mass, charge and site ratio. For the anti-Frenkel (AF) reaction in Equation (1) we can write the equilibrium constant as:

$$K_{AF} = \frac{[v_{O\,48f}^{\bullet\bullet}][O''_{int\,8a}]}{[v_{O\,8a}^{x}][O_{O\,48f}^{\times}]} = \exp\left(-\frac{\Delta_{AF}H^{\circ}}{RT}\right)\exp\left(\frac{\Delta_{AF}S^{\circ}}{R}\right) \quad (5)$$

By using the electroneutrality condition $[v_{O\,48f}^{\bullet\bullet}] = [O''_{int\,8a}]$, and assuming that the fractions $[v_{O\,8a}^{x}]$ and $[O_{O\,48f}^{\times}]$ are approximately 1 (low defect concentration), we see that the concentration of vacancies is dependent on the temperature through the enthalpy of defect formation:

$$[v_{O\,48f}^{\bullet\bullet}] = \exp\left(-\frac{\Delta H^{\circ}_{AF}}{2RT}\right)\exp\left(\frac{\Delta S^{\circ}_{AF}}{2R}\right) \quad (6)$$

Another relevant defect equilibrium for this work is hydration of oxygen vacancies forming two hydroxide defects:

$$H_2O_{(g)} + O_O^{\times} + v_O^{\bullet\bullet} = 2OH_O^{\bullet} \quad (7)$$

The equilibrium constant can be expressed as:

$$K_{Hydr} = \exp\left(-\frac{\Delta H^{\circ}_{Hydr}}{RT}\right)\exp\left(\frac{\Delta S^{\circ}_{Hydr}}{R}\right) = \frac{[OH_O^{\bullet}]^2}{[v_O^{\bullet\bullet}][O_O^{\times}]p_{H_2O}}, \quad (8)$$

showing the relationship between the enthalpy and entropy of hydration, ΔH°_{Hydr} and ΔS°_{Hydr}, the temperature T and the activity of the participating species, here given by the mole fraction of the species $[OH_O^{\bullet}]$ $[v_O^{\bullet\bullet}]$ and $[O_O^{\times}]$ as well as the partial pressure of water, p_{H_2O}/bar. By rearranging these equations we can find how the defect concentrations depend on the partial pressure of water or temperature.

If the vacancies involved in the reaction Equation (7), are introduced due to acceptor doping such as in Equation (3), then the electroneutrality condition reads:
$[Ln'_{Ce}] = 2\,[v_O^{\bullet\bullet}] + [OH_O^{\bullet}]$. These equations can be used to fit the concentration of the species, and therefore also the enthalpy and the entropy included in the hydration reaction, to measured water uptake from thermogravimetry measurements (TG). The electroneutrality conditions for the dominating defects can reduce the number of unknowns when solving these equations by fitting the variables to experimentally measured water uptake.

Protons are usually present in most oxides in hydrogenous atmospheres and can at times also dominate the material properties [34]. Hydration of most oxides usually yield an exothermic hydration reaction, although, in some oxides, like CeO_2, the hydration is theoretically found to be endothermic [35]. Since the hydration enthalpy is determined by change in energy between the dehydrated and hydrated state, it depends on the energy of the defects on the two sides of the equation. To illustrate that hydration constitutes both protonation of the oxide ions and filling of oxygen vacancies, we can split the hydration reaction into two reactions accordingly:

$$H_2O_{(g)} + 2\,O_O^{\times} = 2\,OH_O^{\bullet} + 2\,e' + \frac{1}{2}O_{2\,(g)} \qquad (9)$$

$$v_O^{\bullet\bullet} + 2\,e' + \frac{1}{2}\,O_{2\,(g)} = O_O^{\times} \qquad (10)$$

The two partial reactions can contribute differently to the total hydration enthalpy. Increasingly exothermic hydration enthalpies have for pyrochlores and sesquioxides been correlated with increasing stability of the oxide [32, 36]. This can be explained by the high energy needed to create vacancies in the more stable oxides, which means that more energy is released when the vacancies are filled during hydration. For the perovskite $BaCeO_3$, it has been proposed that filling of vacancies give a much lower energy contribution to the hydration enthalpy than the protonation of oxide ions [37]. Another work on $BaCeO_3$ show the importance of the dopant choice due to the interaction between dopants and vacancies or protons [38]. For doped oxides the dopant can affect the stability of the proton by for

example influencing the charge density on the neighbouring oxide ions, further altering the potential bond strength to the proton. In a recent computational work a new correlation model explaining hydration enthalpies in oxides is presented. They find that both the affinity (of the oxide ion) for protons and the hydroxide affinity (filling a vacancy in an oxide with OH^-) is correlated with the ionization potential of the oxide but with opposite trends. The proton affinity increases with decreasing ionization potential (the energy difference between the valence band maximum, usually from the oxygen, and the vacuum level) [39].

Hydration in fluorite derived structures containing rare-earth oxides

In order to predict the hydration enthalpy for the rare earth containing fluorite related oxides studied in this work, it is useful to understand the correlation between the materials chemistry and the hydration thermodynamic of other related oxides. As mentioned previously, the hydration enthalpy of Ca doped lanthanide sesquioxides (Ln_2O_3), generally becomes more exothermic with smaller Ln [36, 40] as seen in Figure 2 a). The correlation between the hydration enthalpy and the formation enthalpy of the oxide (as seen in Figure 2 c) is explained by the stronger bonds between the Ln/*RE* cation and oxygen. The enthalpy of formation for oxygen vacancies is then expected to become more positive, which means that the opposite direction of the reaction, filling of vacancies, will contribute significantly with exothermic enthalpy change when hydrated. That is, although oxygen vacancies are not formed intrinsically the theoretical formation enthalpy is relevant due to the opposite reaction; filling of a vacancy, which contributes to the hydration enthalpy as seen in Equation (10).

For the pyrochlore structure $RE_2X_2O_7$, computational studies have shown that smaller trivalent rare earth cations result in *less* stable oxides, further decreasing the (positive) formation energy of vacancies. This results in the hydration enthalpy becoming less exothermic [32]. The hydration enthalpy of doped $RE_2B_2O_7$ thus becomes more exothermic with larger *RE* size due to increased oxide stability.

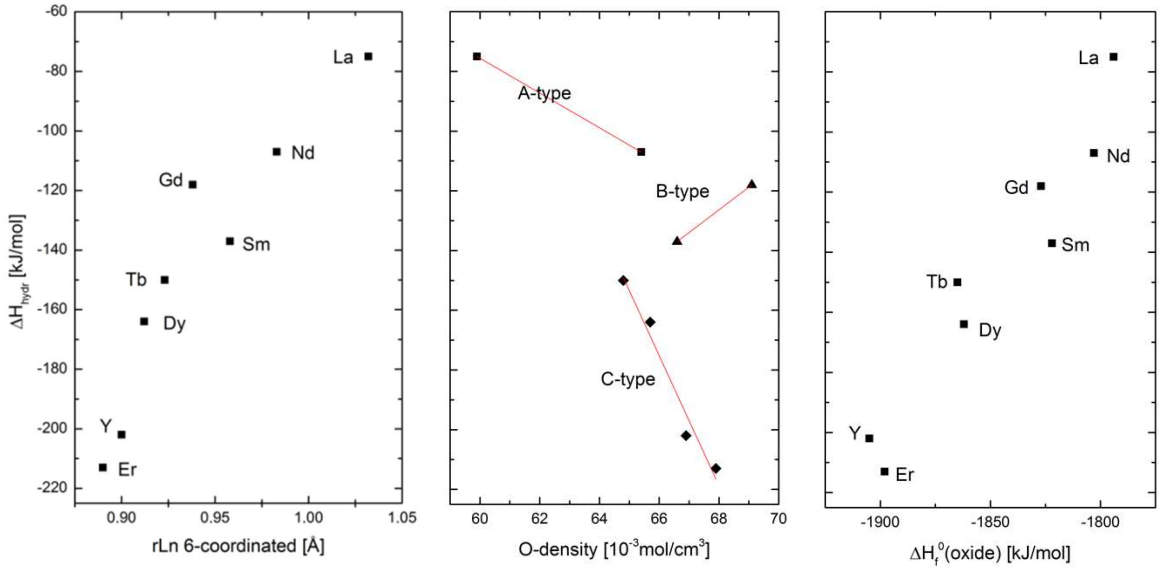

a) b) c)

Figure 2 The measured hydration enthalpy of Ca doped Ln_2O_3 from [36, 40] versus a) the Ln ionic radius, b) oxygen density and c) oxide formation enthalpy ΔH_f°

Hydration studies show that minute or moderate levels of acceptor doping of CeO_2 is not sufficient to result in hydration and proton conductivity at low to intermediate temperatures. Although acceptor doping of CeO_2 results in increased vacancy concentration and enhanced oxygen ion conductivity, it gives seemingly no effect on the hydration and formation of hydroxide defects. This is in line with the computational studies of CeO_2 showing that hydration is endothermic [35]. However, heavily La doped CeO_2, with the stoichiometry $La_2Ce_2O_7$ hydrates and protons dominate the electrical conductivity in wet atmospheres at low temperatures [14, 16]. When heavily doped, the ability for CeO_2 to hydrate must therefore change, an issue that is addressed in this thesis.

Hydration and conductivity studies of $La_{28-x}W_{4+x}O_{54+\delta}$, show proton conductivity at quite high temperatures, which is explained by a fairly exothermic hydration enthalpy [18, 41-43]. The maximum hydration level, however, cannot be described by the average structure of $La_{28-x}W_{4+x}O_{54+\delta}$. When comparing previous studies, the hydration and proton conductivity decrease when $La_{28-x}W_{4+x}O_{54+\delta}$ is doped with Ca [17, 41] an issue we address in the discussion of this thesis. To understand the limitations to the maximum hydration level, investigations on the local structure is necessary. The investigations related to this work provide more insight on this issue.

2.3 Defects and ionic conductivity of fluorite related oxides

The conductivity, σ_i, of a species *i,* can be described:

$$\sigma_i = z_i e c_i u_i, \quad (11)$$

Where z_i is the charge of the species, *e* the elementary charge, the concentration c_i and the mobility u_i of the species *i.* When several charge carriers are present, the total conductivity is the sum of the partial conductivities:

$$\sigma_{tot} = \Sigma_i \sigma_i \quad (12)$$

The random diffusion coefficient in a cubic sublattice can be expressed by the jump frequency, Γ, for the jump distance *s*:

$$D_r = \frac{1}{6} s^2 \Gamma \quad (13)$$

The jumping frequency, Γ, is dependent on the frequency of jumps with sufficient energy and the number of sites the species can jump to. The number of sites is expressed by the number of nearest sites times the concentration of vacant sites, if the diffusion occurs through the vacancy mechanism. For oxide ion diffusion we can find the concentration of vacancies through the formation reaction. For example, the concentration of vacancies created through the anti-Frenkel defect in Equation (1), can be expressed through the equilibrium constant shown in Equation (5). Both the migration jump and the creation of vacancies are activated processes and the energy needed to perform a successful jump, $\Delta H_{mob,O^{2-}}$, and creating a vacancy, $\Delta H_{defect(vac)}$, thus constitute the activation energy for oxide ion diffusion through the vacancy diffusion mechanism. The diffusion coefficient for oxide ions can be generally expressed as:

$$D_{O^{2-}} = D_{0,O^{2-}} \exp\left(\frac{-E_{A,O^{2-}}}{RT}\right) = D_{0,O^{2-}} \exp\left(\frac{-\left(\Delta H_{mob,O^{2-}} + \Delta H_{defect(vac)}\right)}{RT}\right) \quad (14)$$

If the vacancies are created through the anti-Frenkel reaction, the relation in Equation (5) can be used to write the diffusion coefficient more specifically, as:

$$D_{O^{2-}} = D_{0,O^{2-}} \exp\left(\frac{-E_{A,O^{2-}}}{RT}\right) = D_{0,O^{2-}} \exp\left(\frac{-\left(\Delta H_{mob,O^{2-}} + \frac{1}{2}\Delta H_{AF)}\right)}{RT}\right) \quad (15)$$

If the vacancy concentration is defined by the dopant concentration and therefore constant, $E_{A,O^{2-}}$ represents $\Delta H_{mob,O^{2-}}$only. Using the Nernst-Einstein relationship, we can combine Equation (11) with Equation (13) if we assume that random diffusion D_r of a species can be related to the conductivity (i.e. $D_{r,i} = D_i$):

$$D_i = u_i \frac{kT}{z_i e} = \sigma_i \frac{kT}{c_i z_i^2 e^2} \quad (16)$$

From Equation (16) we see that the temperature dependence for $\sigma_i T$ will be the same as the temperature dependence of D_i, and we can express the $\sigma_{O^{2-}} T$ as:

$$\sigma_{O^{2-}} T = A \exp\left(\frac{-E_{A,O^{2-}}}{RT}\right) = A \exp\left(\frac{-\left(\Delta H_{mob,O^{2-}} + \Delta H_{defect(vac)}\right)}{RT}\right), \quad (17)$$

and the pre-exponential can be written as:

$$A = D_{0,O^{2-}} \frac{c_{O^{2-}} z_{O^{2-}}^2 e^2}{k} \quad (18)$$

The $c_{O^{2-}}$ can for most cases be considered essentially constant since the relative concentration change will be insignificant unless the vacancy concentration is close to the concentration of oxide ions in the compound.

If we plot experimentally obtained conductivity in an Arrhenius plot $\sigma_i T$ vs $1/T$, we can find the value for the activation energy $E_{A,i}$ from the slope. If the curve has distinctly different activation energies at different temperatures it can be due to for example change in the activity of the constituents or changes in the mobility parameters. Distinctly different mobility can be connected to a phase transition, or associated species becoming fully dissociated (going from higher activation energy at lower temperatures to a region with lower activation energy at higher temperatures). In some cases the temperature can be too low to activate a process (e.g. intrinsic formation of vacancies) and the activation energy of this process will then only contribute at higher temperatures. This will result in the activation energy becoming higher at higher temperatures due to an additional contribution (e.g. from the activation of vacancy formation).

Proton transport is assumed to be faster than transport of oxide ions since they are smaller. The activated jumping mechanism that normally lies behind proton transport in oxide proton conductors, called the Grotthus-mechanism [34, 44] has in general a lower activation energy than oxide ions diffusion through the vacancy mechanism. The Grotthus-mechanism is an interstitial diffusion mechanism and then the number of potential sites the proton can jump to is not dependent on the concentration of any defect. The activation energy for diffusion therefore only contains the enthalpy of mobility $\Delta H_{mob,H+}$:

$$\sigma_{H+} T = A \exp\left(\frac{-E_{A(H^+)}}{RT}\right) = A \exp\left(\frac{-\left(\Delta H_{mob,(H^+)}\right)}{RT}\right) = D_0 \frac{c_{H+} e^2}{k} \exp\left(\frac{-\left(\Delta H_{mob,(H^+)}\right)}{RT}\right) \quad (19)$$

The enthalpy of mobility contains potential trapping or association between protons and for example a dopant, creating a higher jumping barrier to escape the trap. The enthalpy of mobility can therefore be expressed as the sum of $\Delta H_{0,mob,H+} + \Delta H_{trap,H+}$ being the inherent enthalpy for jumping as a free and untrapped proton, and the trapping enthalpy. As seen in Equation (19), the concentration of protons is a factor in the conductivity which

depends on temperature through the hydration enthalpy, as seen in Equation (8). If the concentration of protons is not constant for the temperature range where conductivity is measured, this will influence the apparent activation energy of proton conductivity.

Defect association and oxide ion conductivity in doped ceria

Some of the best oxide ion conductors known are acceptor doped ceria and zirconia with the fluorite structure such as Yttrium stabilized zirconia (YSZ) and Gadolinium doped ceria (GDC) [11]. The presence of oxygen vacancies is necessary in order to allow for the vacancy diffusion mechanism, and the effects of the properties of the dopant on the conductivity have been investigated for many decades. Size and concentration of the dopant in doped ceria, influence the oxide ion/vacancy diffusion, as we now will see.

Trivalent rare earth acceptor dopants and the charge compensation vacancies formed in ceria, interact even for dilute dopant concentrations (i.e. < ~1%) [45-47]. Several studies have shown how the binding energy between the acceptor and oxygen vacancy depends on the size of the rare earth dopant. Gerhardt- Anderson et al., reported that the ionic conductivity was highest and activation energy lowest for dopants with the most similar size compared to the ceria cation, which is Gd^{3+} for the rare earths (8-fold coordinated Ce^{4+} compared with 6-fold coordinated Gd^{3+}) [46]. This trend was later supported by Butler et al. using theoretical methods (Mott-Littleton ionic models) [48]. They argued that for cations smaller than Gd^{3+} (in this case Sc^{3+} and Y^{3+}) the association energies were due to electrostatic forces between dopant and vacancy. For the larger cations (La^{3+} and Gd^{3+}) the association energy was due to reduction of strain in the crystal structure initially caused by the size mismatch between the dopant and Ce. Atomistic simulation done by Minervini et al. [49] elucidated the trend observed related to the size of the RE dopant. They show that for smaller cations (than Gd^{3+}) the highest binding energy is obtained when the vacancy is on a 1st neighbour site of the dopant, and the binding energy decreases when the cation size increases (towards Gd). For the cations larger than Gd, the binding energy is highest when the vacancy is situated as a 2nd nearest neighbour to the dopant, and the energy decreases with decreasing RE^{+3} size (towards Gd). This means Gd^{3+} is the crossover point between the two trends which indicate whether vacancies prefer to be 1st or 2nd nearest neighbour to the dopant. It further explains that Gd^{3+} gives the minimum binding energy between dopants and the oxygen vacancies.

Wang et al. developed a model that connects the association energy between dopants and vacancies to the variation in activation energy measured for different dopant. They found that for Y_2O_3 dopant concentrations up to ~4%, the Arrhenius representation for the conductivity deviates from linearity. This was interpreted to reflect the association energy contributing to the effective activation energy for oxide ion conductivity at the lower temperatures of the conductivity measurements (i.e. $E_A = H_{mob} + H_{association}$) [45]. As the

temperature increase the system changes into a state where all vacancies are unassociated and activation energy only depends on the mobility of the free vacancies yielding lower effective activation energy. (i.e. $E_A = H_{mob}$). They further observed that the activation energy decreased with increasing dopant concentration up to ~4%, which they explain by fluctuating electrostatic fields between the dopant and the vacancies. The vacancies will be drawn towards new favourable locations close to a dopant, effectively reducing the enthalpy of association as the number of dopants increases. As the concentration increases above 4% Y_2O_3, the effective activation energy for conductivity increases rapidly which they suggest stems from deep traps of vacancies due to more than one Y^{3+} dopants in nearest or next nearest neighbouring site of the vacancies. The traps increase in strength and concentration with increasing yttria content. These observations and models were further shown to also apply for other rare earth dopants in a study on defect association and percolation by Faber et al. [47]. In the mentioned work, the conductivity maximum and activation energy minimum were for samples of ceria doped with 1-4% RE_2O_3 (*RE* = La, Nd, Gd, Y, Yb), and Gd exhibited the lowest activation energy for concentrations above 3%. The trends in association between vacancies and dopants depending on dopant size is supported by a more recent theoretical study of rare earth doped ceria [50], further emphasizing how similar size of the dopant and Ce is beneficial.

The studies mentioned above show that acceptor doping CeO_2 more than 10-15% $REO_{3/2}$ (when translated to Y^{3+} doping), does not result in increased conductivity due to trapping of the vacancies by dopants. We will continue to look into the vacancy interactions when ceria is heavily doped or reduced.

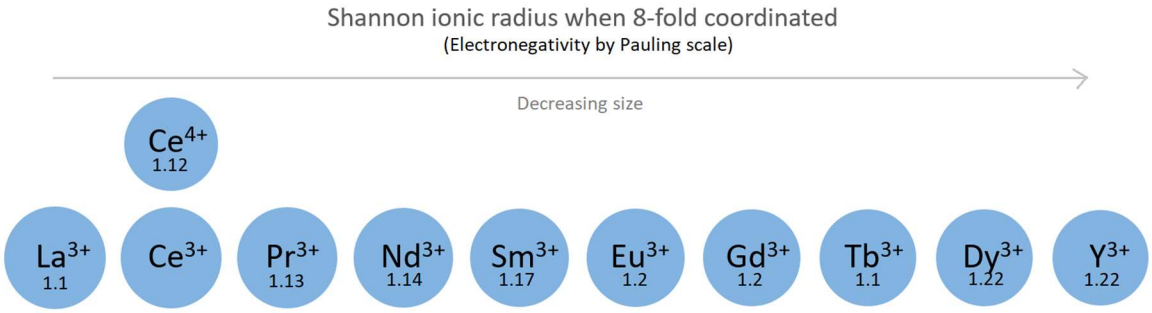

Figure 3 Size relation of 8-fold coordinated rare earth cations, and their electronegativity in the Pauling scale.

Order and disorder in fluorite related structures

When the concentration of dopants and/or oxygen vacancies increases, the increasing interactions result in short or even long range order. When ceria becomes sufficiently oxygen deficient due to reduction (as described in Equation 2) vacancies pair up with a ½ <111> alignment between them, as shown for $CeO_{2-\delta}$ when $\delta > 0.3$ by Hull et al. [51]. The short range ordering of the vacancies starts to occur when $CeO_{2-\delta}$ is closing up to the stoichiometry for the ordered structure of Ce_7O_{12}, and the vacancy ordering is similar. Ce_7O_{12} is the first ordered phase stable at high temperatures when $CeO_{2-\delta}$ is reduced, and the structure is described in the work of Ray et al. [52]. The vacancy ordering in ceria can therefore be seen as a seed of the transition to a fully ordered phase. The same type of vacancy ordering has been found for YSZ [53].

The type of vacancy ordering found in ceria has been found to be important for most fluorite related structures. As Rossell and Scott underlined, all superstructures of the fluorite structure were commonly believed to always exhibit vacancy ordering in <111> vacancy-vacancy pair (i.e. third next nearest ordering of vacancies) through a cube with a cation giving the cation a octahedral coordination [54]. A relevant example is the pyrochlore structure which can be described as <111> vacancy-vacancy pairs linked in zig-zag lines. Rossell and Scott also conclude that for the ordered superstructures of fluorites, no vacancies are situated closer than in the <111> alignment, except for in the C-type superstructure where the vacancies also are aligned in <110> direction [54]. This exception proves important for the ordering we discover for 50% doped ceria in this work.

When fluorite oxides such as CeO_2, are heavily doped with rare earth sesquioxides, the association between dopants and vacancies plays a role in the ordering into fluorite super structures. For dopant concentrations above 25% there are in principle no configurations where vacancies can be further away than as 3rd nearest and 2nd nearest neighbour to the dopant. The work by Minervini et al. also find that $Ln'_{Ce} - v_O^{\bullet\bullet} - Ln'_{Ce}$ trimers is likely to form when concentration of dopants is above a few percent [49]. When CeO_2 is doped with lanthanides, the smallest ion present generally prefers lower coordination, as described earlier, and this preference as well as the trimers described above, can be accommodated in the ordered structure of pyrochlore when CeO_2 is doped with 50% $LnO_{1.5}$ of the larger lanthanides, such as $LaO_{1.5}$. Thus the <111> vac-vac preference of reduced ceria as well as the structural relaxation when dopants larger than Ce^{4+} have vacancies as second nearest neighbour, predicts of the pyrochlore structure for $La_2Ce_2O_7$ and $Nd_2Ce_2O_7$.

However, most studies on $La_2Ce_2O_7$ do not find evidence of the pyrochlore structure [14, 21, 27, 31]. $La_2Ce_2O_7$ is rather found to be a disordered fluorite, although there are studies advocating the pyrochlore structure [25]. According to a model from Minervini et al., the cation radius ratio, rA^{3+}/rB^{4+}, of a $A_2B_2O_7$ pyrochlore must be above 1.4 in order to form a

stable pyrochlore structured oxide, if not disordering will be favourable [28]. Both $La_2Ce_2O_7$ and $Nd_2Ce_2O_7$, are as such outside the pyrochlore stability range, whereas $La_2Zr_2O_7$ with a smaller B-cation, will order in the pyrochlore structure. As predicted, $Nd_2Ce_2O_7$ is also not exhibiting the pyrochlore structure, instead evidence of C-type ordering has been indicated [21-24, 55].

C-type ordering severely decreases the conductivity as observed by Yamamura et al. for heavily doped ceria [21]. They find that the conductivity decreases with smaller Ln in $Ln_2Ce_2O_7$ and Gd is no longer the best dopant when the goal is to obtain the highest oxide ion conductivity due to C-type ordering. This is supported by the findings of Ou et al. when using HR-TEM. Diffuse scattering, additional to the fluorite Bragg peaks, show that formation of microdomains with order have an opposite trend correlated to dopant size than acceptor-dopant association (i.e. rare earth more similar to Ce form microdomains to a stronger degree [56]. A relevant study on the origin of partial vacancy ordering related to the C-type structure, is from Withers et al., where the compositional study of $(CeO_2)_{1-x}(YO_{1.5})_x$ using HR-TEM, shows evidence of C-type related vacancy ordering in microdomains for the ~50 $YO_{1.5}$ doped CeO_2. They further find that when there is a dual phase region between 60% and 75% $YO_{1.5}$, and above this concentration the sample obtains an oxygen excess C-type structure [57]. Some studies on $Ln_2Ce_2O_7$ compounds with Ln = Sm, Gd and smaller, have found ordering in hybrid structures between fluorite and C-type, and biphasic structure models where Ln cluster in regions with coordination numbers closer to the C-type structure [58, 59]. Biphasic models can be explained by the acceptor-vacancy association previously described for Gd and the smaller Ln cations, where the Ln^{3+} prefer vacancies being in a nearest neighbour position due to its smaller ionic size than the 8-fold coordinated Ce^{4+}. That is, the smallest cation is 6-fold coordinated. The local structure is then similar to that of the C-type structured Ln_2O_3.

3 Methodology

"Science is what scientist do, and there are as many scientific methods as there are individual scientists."

— Percy Williams Bridgman

In this chapter we will briefly go through the theory and practical implementation of some experimental techniques and computational approaches relevant for the work in this thesis. We will also elaborate on some methods and less conventional choices made in this work, and on specific challenges with some of the approaches. The most important computational and experimental details for our work are presented in the papers.

3.1 Sample preparations of $La_{2-x}Nd_xCe_2O_7$

Solid state reaction

In paper I we describe the sample preparation of the powders used for structural analysis of $La_{2-x}Nd_xCe_2O_7$ where x = 0, 0.5, 1, 1.5 and 2. The powder samples were prepared using solid state reaction with heating and regrinding steps, and sintered in pellets and re-grinded several times. These powders are further used for TG-DSC measurements presented in paper III. Numerous and long sintering processes are advantageous in that the chance of full reaction increases. Conversely, preparing dense samples for electrical characterization of the resulting powders gets more difficult, since the "reactivity" of the powder becomes very low. The pellet samples made for electrical characterization were prepared by pressing the powder into pellets, followed by sintering at 1400 ºC. After sintering, the samples exhibited a relative density of approximately 60%. As we shall see, this high porosity decreases the total conductivity. However, the temperature dependencies remain comparable with those measured in previous works, and the value of running experiments on the same samples that are subjected to in-depth structural analysis is considered greater than the disadvantages of a porous sample.

Electron microscopy

The grain size and morphology of the powders and pellets were analysed using scanning electron microscopy, (SEM, Quanta 200F), before and after measurements. The samples only showed small and expected changes after measurements, such as a small degree of sintering and the formation of some impurities on the surface due to the platinum electrodes. Semi-quantitative analysis of the composition of the samples was performed using the EDAX system integrated in the SEM using EDS-detector (energy dispersive spectroscopy).

To further study the origin of supercell lattice peaks found by diffraction methods, we studied a sample of $Nd_2Ce_2O_7$ using high resolution transmission electron microscopy (HR-TEM, JEOL2100F) to perform selected area diffraction (SAED). The observed extra satellite reflections are used to take dark field images in order to indicate the presence of domains with supercell reflections. We also performed energy dispersive X-ray analysis using the JEOL, for areas in the prepared sample in order to ensure that we were not looking at any impurities and that the stoichiometry between Nd and Ce does not deviate significantly from the $Nd_2Ce_2O_7$ compound.

3.2 Diffraction techniques and analysis

Powder X-ray diffraction (XRD) and Neutron powder diffraction (NPD) are widely used to investigate the long range structure of solid crystalline materials. X-rays and neutrons are scattered by the electrons and atoms nucleus respectively, giving rise to diffraction patterns according to the crystal structure of a crystalline material. The diffraction patterns are a product of symmetries resulting from repeating atomic arrangements constituting the long range order of atoms.

The X-rays in powder XRD, interacts with the electron cloud of the atoms in the crystal, and the scattering cross-section increases with the atomic number Z of atoms. For neutron diffraction the scattering length and the amount of incoherent and coherent scattering vary for all elements, and have no systematic trend, as is the case for X-ray scattering. This means that NPD is more suitable for detecting some light elements, such as hydrogen and oxygen, depending on the scattering length. Two elements with similar electron cloud may also have significantly different scattering cross-sections for neutrons

The X-rays may be absorbed and usual wavelengths give penetration depths in the micrometre range. During diffraction, neutrons interact weakly with most elements and are not absorbed, and typical penetration depths are in the millimetre range. This means that the neutron beam allows us to investigate the crystal structure in the internal region of both small and big samples.

The crystal structure can be solved by Rietveld [60] analysis of diffraction patterns obtained from XRD or NPD, and the Rietveld refinements describe the average long range structure of the sample investigated. In addition to a Rietveld refinement offering positions, symmetry and cell size, total scattering experiments can provide the pair distribution function, also called the radial distribution function, between atoms in the sample.

In Paper I neutron total scattering has been performed on the samples of $La_{2-x}Nd_xCe_2O_7$ by applying several detector banks covering a wide range of scattering vector Q (where $Q = 2\pi/d$ and d is the interplanar spacing). (The reader is referred to Paper I for more practical details of the scattering experiments and analysis methods.)

G(r) and analysis

After combining and normalizing the results to a total scattering structure factor, $S(Q)$, we obtain the corresponding total radial distribution function, $G(r)$, through Fourier transformation. $G(r)$ can be written as:

$$G(r) = \frac{1}{(2\pi)^3 \rho_0} \int_0^\infty 4\pi Q^2 S(Q) \frac{\sin Qr}{Qr} \mathrm{d}Q \quad , \qquad (20)$$

where ρ_0 is the average atom number density in atoms $Å^{-3}$ (for details, see Keen [61]).

G(r) is a distribution function describing the distribution of bond lengths for all atoms. Since the total distribution function $G(r)$ also can be expressed in terms of the individual partial radial distribution functions between pair of atoms, $g_{ij}(r)$, we can compare the distribution function obtained from a modelled structure configuration tot the total G(r):

$$G(r) = \frac{\sum_{i,j=1}^{n} c_i c_j \bar{b}_i \bar{b}_j g_{ij}(r)}{\sum_{i=1}^{n} \left(c_i \bar{b}_i\right)^2} \quad , \qquad (21)$$

where n is the number of ionic species, and the function is weighted by the concentrations of the two species, c_i and c_j, and their coherent bound neutron scattering lengths, $\bar{b}_i$ and $\bar{b}_j$. The partial radial distribution function can then be written as:

$$g_{ij}(r) = \frac{1}{4\pi r^2 \Delta r} \frac{n_{ij}(r)}{\rho_j} \quad , \qquad (22)$$

with $n_{ij}(r)$ equal to the number of atoms of type j located at a distance between r and $r + \Delta r$ from an atom of type i and ρ_j is the number density of atoms of type j, given by $\rho_j = c_j \rho_0$.

Long range structure is the result of local structure and the two properties are linked as seen by the partial and total radial distribution functions above. Although diffraction methods do not offer explicit pictures of the local structure through refinements, the total distribution function from total scattering creates a frame that the local structure must fit into.

One way of analysing the radial distribution function in order to look for possible local structure is Reversed Monte Carlo modelling RMC, implemented in the RMCProfile software [62]. RMC probes for the atomic configurations giving the individual partial distribution functions, $g_{ij}(r)$, which together result in the $G(r)$ that best fits the experimentally obtained $G(r)$. RMC simultaneously probes both the long range and short range structural properties within the user defined limitations such as possible lattice sites and properties of the ions. Structure configurations found by DFT can also be compared with the total radial distribution function, a topic we will come back to in Section 3.6.

3.3 Thermogravimetry (TG) and differential scanning calorimetry (DSC), TG-DSC

Combined thermogravimetry and differential scanning calorimetry, TG-DSC, allows us to simultaneously measure the mass change and heat flow occurring as a response on changes in temperature (or partial pressure when connected to a flowmeter or similar). Conceptually, TG can be thought of as a scale that measures mass change of the sample while the temperature is changed over time using a heating element. DSC enables measurements of the heat exchange occurring during for example a hydration process, by measuring the voltage needed to sustain the same temperature for a reference crucible as for the crucible containing the sample. When combined we obtain energy released or captured during the weight change. When connected to a wetting stage or water vapour generator, TG-DSC can be used to investigate hydration processes. The TG gives data on the water uptake, and the hydration enthalpy can be found by dividing the total heat exchange by the number of moles of water incorporated.

The DSC signal exhibits a baseline shift during the hydration process leading to a potentially significant source of uncertainty. It has previously been proposed that the shift in the heat exchange signal is due to a change in the thermal conductivity of the sample when hydrated [63]. To take into account the baseline shift we have used a sigmoidal shape during the integration of the DSC data. By changing the limits of the integral and accounting for small changes in the measured mass, we obtain a statistical mean value and standard deviation of the hydration enthalpy, as reported in Paper III.

In the preparations for the TG-DSC measurements on $La_{2-x}Nd_xCe_2O_7$ we found that the resulting signals from water uptake become more significant when changing the conditions from dry to wet atmosphere with ~1 atm of water vapor, compared to the uptake found in atmospheres with a partial water vapour pressure of 0.025 atm, as obtained by a typical wetting stage.

3.4 Electrical characterization

In this work, electrical characterization of samples of the $La_{2-x}Nd_xCe_2O_7$ series is performed as a function of temperature and partial pressure of oxygen or water (pO_2 and pH_2O). The conductivity was measured under controlled atmosphere and temperature using a ProboStat^{TM} (NorECs, Norway) measurement cell, coupled with a furnace with temperature controller, and a gas-mixer [64].

By using a 2-point 4-wire setup and an impedance analyser (Solartron 1260), both constant frequency measurements at 10 kHz and impedance sweeps in the frequency range 0.5 - 10^6 Hz, are performed. Prior to all impedance measurements the samples are equilibrated with the surrounding gas at each temperature. When the conductivity is measured while ramping the temperature down to room temperature, the ramping rate is slow in order to allow the sample to reach equilibrium.

The conductivity of a sample depends both on the bulk and grain boundary conductivity. The grain boundary capacitance in oxides is often 1-2 orders of magnitude higher than the bulk capacitance. Impedance spectra plotted in a Nyquist plot, where the real and imaginary part of the impedance are plotted over frequency, may result in one or two semicircles depending on the impedance and characteristic frequency of bulk and grain boundary. The impedance spectra collected for the $La_{2-x}Nd_xCe_2O_7$ samples display two semicircles at lower temperatures, which can be fitted by a series of two parallel circuits comprising a resistor and a capacitive constant phase element (RQ) (i.e. resulting series $(R_1Q_1)(R_2Q_2)$ for the bulk and grain boundary). For more details on impedance spectroscopy or the Brick Layer Model, the reader is referred to for example Irvine et al. [65] or Haile et al. [66]. The first semicircle given by the highest frequencies is considered as bulk due to the capacitance found to be around 10^{-12} - 10^{-11} F for all samples. For the second element, the capacitance is only 1-2 magnitudes greater and the resistance is low compared to bulk ($R_1 > R_2$), which usually indicates a grain boundary contribution. A potential third semi-circle would be the result of the electrode process. At higher temperatures the two semicircles become indistinguishable, and by assuming that the bulk resistance exceeds the resistance of the grain boundary we can ascribe the remaining semicircle to bulk.

The conductivity measured at 10 kHz represents the bulk well at most temperatures in the temperature window of these measurements. This can be seen by identifying where the 10 kHz point is located within the bulk semicircle, and checking that the real part of the admittance at 10 kHz equals that of the main part of the bulk semicircle. For instance, at temperatures below 400°C, the admittance will be higher compared to the admittance of the first circuit element when the 10 kHz point is approaching the origin. This is due to the effect of short circuiting of the capacitance part of the equivalent circuit. At high temperatures above 800 °C, only the electrode contribution is visible in the impedance spectra, and the measured conductivity will be lower than the bulk conductivity when the 10 kHz point includes resistance from the electrode contribution.

In Paper III, and for the additional conductivity data presented in Chapter 6 Discussion, the constant frequency data at 10 kHz is presented, but due to the limitations just explained we correct the data for the highest and lowest temperatures by analysing the impedance spectra to obtain the bulk conductivity.

The samples analysed are quite porous, and the deviation in conductivity predicted due to low density may not necessarily be directly proportional to relative density when the porosity is high [67]. Therefore, the conductivity data are only corrected for thickness of the sample and the electrode area, and not for porosity. However, the densities for all the samples are relatively similar, and close to 60%. Therefore, the total conductivities measured are expected to be suitable for comparison between the samples. Furthermore, we do not expect the porosity to affect the temperature dependence used to investigate the activation energies, since the porosity usually has a stronger influence on the low frequency semicircle. That is, using the Brick Layer Model on the impedance data for porous samples mainly affects the deconvolution of the grain boundary [68, 69].

3.5 Classical force field calculations

Classical force field calculations are a rather simple atomistic simulation technique different from DFT, which simulates the forces between ions based on typical simple “pair potentials” to describe interactions between atoms. The potentials are described in mathematical terms, numerical or analytical as a function of particle coordinates. It is an empirical method and the reliability depends on how well the potentials describe the modelled system. The main advantage is low computational cost giving the possibility of studying large systems or numerous configurations quickly, compared to simulation techniques using electron density or atomic orbitals which demand more computational effort.

GULP estimates the lattice energy as the sum of short and long term interactions between ions. A general expression for the lattice energy of a static lattice:

$$E_L = \sum_{ij} \frac{q_i q_j}{r_{ij}} + \sum_{ij} \Phi_{ij}(r_{ij}) + \sum_{ijk} \Phi_{ijk}(r_{ijk}) + \ldots \quad (23)$$

where *i, j, k,* etc. denote different atoms, q and r their charge and interatomic separation. The first term is the sum of Coulomb interactions between pairs of atoms i and j describing the local environment. The second term is the two-body, central-force part of the short range interactions between pairs of atoms and is the dominant part of the short range energy of the system. The third term is the same for three-body interactions, which gives little contribution to the lattice energy, but is significant when calculating vibrational properties. For ionic materials, the interactions between pairs of atoms can be assumed to dominate the total energy so that all interactions between a higher number of atoms can be considered negligible [70].

The interatomic potentials frequently used are the Buckingham potential (other popular ones are Morse potentials, especially in oxides with hydrogen defects present). The Buckingham potential includes an exponential repulsion term and an attractive $1/r^6$ term:

$$\Phi_{ij}(r_{ij}) = A\, e^{-r_{ij}/\rho_{ij}} - \frac{C}{r_{ij}^6} \quad (24)$$

Ionic polarization can in addition be described with the shell model, first developed nu Dick and Overhauser [71]. In the shell model polarizable valence shell electrons are represented by a mass-less shell connected to the core by a harmonic spring. The model provides more accurate values for elastic and dielectric properties, which is valuable when modelling defects since the response of the surrounding crystal is largely elastic and dielectric when a defect is included.

There are mainly three types of properties that can be studied; structural, physical and defect properties. The method iteratively calculates forces between all ions and relaxes the structure in order to minimize the energy, and can thus be used to predict the crystal structure and rearrangements around structural and point defects. Both bulk and surface can be studied with this technique. When modelling the energy in the system and interactions between the ions, the physical properties of a system, such as dielectric and elastic constants and phonon dispersion curves can be calculated at the same time. Comparing the results to experimental results, can be a good reference point to whether a as the potentials used are adequate.

In Paper IV we use configurations found using GULP, general utility lattice program [72], as a first approximation to determine which type of site the excess W is located on in the structure of $La_{28-x}W_{4+x}O_{54+\delta}$ (*i.e.* if W prefer a interstitial site or if it substitutes La). We

know the stability range of x in $La_{28-x}W_{4+x}O_{54+\delta}$ and the average crystal structure from the work of Margasó et al. [30].

In this work we have used a combination of Buckingham potentials and shell models giving a coupling between polarization and short-range repulsion. As the first adequate parameters for the potentials of La, W and O, in $La_{28-x}W_{4+x}O_{54+\delta}$, we use the potentials earlier used for Bi_2WO_6 [73] and $Sc_2(WO_4)_3$ [74]. We performed calculations on numerous different configurations for $La_{28-x}W_{4+x}O_{54+\delta}$ where $x = 0$ and 1. We could rule out configurations that have phonon modes with negative frequencies, since these configurations are dynamically instable. Finally we selected a set of promising configurations based on final structural parameters and phonon calculations which we investigated further using DFT.

3.6 Density functional theory (DFT)

Density functional theory is an approach that aims to solve the many particle, time independent Schrödinger equation, and find the total energy of a system using first principles calculations. The foundation of DFT is the Hohenberg-Kohn theorems [75] which state that the electron density $n(\boldsymbol{r})$ of a system with interacting particles in an external potential $V_{ext}(\mathbf{r})$, can be used as a variable to find the non-degenerate ground state of the system and all related physical properties. They further state that there is a universal electron density functional $F_{HK}[n(\boldsymbol{r})]$ independent of the external potential, which together with the energy from the external potential give an energy functional of the system, $E[n(\boldsymbol{r})]$:

$$E[n(\boldsymbol{r})] = F_{HK}[n(\boldsymbol{r})] + \int n(\boldsymbol{r})\, V_{ext}(\mathbf{r})\mathrm{d}\mathbf{r} \qquad (25)$$

When the electron density is minimized to the ground state electron density, $n_0(\boldsymbol{r})$, the energy functional gives the ground state energy of the system.

Kohn and Sham [76] further developed a practical scheme for solving for the ground state, given by the universal functional, by expressing the electron density as a set of non-interacting particle orbitals. For this system the kinetic energy of non-interacting electrons $T_{ni}[n(\boldsymbol{r})]$ and the Coulombic electron-electron interactions $J_C[n(\boldsymbol{r})]$ of the electron density functional $F_{HK}[n(\boldsymbol{r})]$ can be found without any approximations. The non-classical electron-electron interactions that are unknown and not possible to solve exactly, are left in the Exchange-correlation functional $E_{XC}[n(\boldsymbol{r})]$:

$$E[n(\boldsymbol{r})] = T_{ni}[n(\boldsymbol{r})] + J_C[n(\boldsymbol{r})] + E_{XC}[n(\boldsymbol{r})] + \int n(\boldsymbol{r})\, V_{ext}(\mathbf{r})\mathrm{d}\mathbf{r} \qquad (26)$$

The electron exchange can be solved by the Hartee-Fock approximation, but the approximation does not include the electron correlation. Thus only the exchange-correlation

functional in equation (26) cannot be solved exactly. The development of DFT has since then mostly been on optimising the exchange correlation functional, and there now exist several approaches.

First principles calculations have in the last decade become a powerful tool for investigating the energetics of structures and defects of solid state oxides. The development of exchange correlation functionals and implementations in calculations packages such as the Vienna Ab-initio simulation package (VASP [77]) utilized in this work, have accelerated simultaneously with the increasing computational resources available worldwide.

In this thesis we have performed structural optimisations and MD simulations on configurationally disordered $La_2Ce_2O_7$, $Nd_2Ce_2O_7$ and $La_{28-x}W_{4+x}O_{54+\delta}$ (for x = 0, 1). Structural optimisations of many possible structural candidates which also represent local snapshot of bulk in the disordered state are performed. Our main objective of the structural optimisations has been to search for the lowest energy configurations of these disordered compounds, as well as to look at their local structure and how the different arrangements of cations and oxygen/vacancies are arranged energetically. For systems with unknown ordering and possible high degree of disorder, the search for representative configurations demands testing of numerous configurations including predictions of possible favourable configurations based on iterative procedure as well as trial and error. Atomistic calculations using classical potentials are less computationally demanding and can be used for an initial search for favourable configurations, which we have done for the $La_{28-x}W_{4+x}O_{54+\delta}$ system. *Ab inito* molecular dynamics simulations also contribute in the search for favourable configurations by quenching configurations along the trajectory. In this section we will briefly go through the chosen approaches and parameters in this work.

Exchange correlation functional

The approximation first proposed to the exchange correlation functional is the simple local density approximation (LDA) [76]. In LDA the electron density is described as a uniform electron gas at a given point in order to calculate the exchange correlation energy. In other words, the density depends only on the value of the electronic density at each point in space. The approximation is in general in good agreement with experiment for many properties of many compounds. For the crystal structure the deviation in cell parameters and equilibrium volumes are a few per cent away from those found experimentally. That is, LDA is known to often over-estimate the binding energies resulting in too small lattice parameters.

The generalized gradient approximation, GGA, is in general, an improvement over LDA, the gradient of the electron density is included to estimate the exchange correlation energy. This can better describe systems with less homogenous electron density. There exist both semi-empirical and *ab initio* derived GGA functionals and for calculations on crystal

structures the PW91 [78] and PBE [79] functional is most often used. In contrast to LDA, GGA is often found to overestimate the lattice constants. GGA also usually underestimates the bandgap significantly. However, in this work the main interest is not the band structure but the structure (i.e. how the ions arrange themselves locally), and therefore we have used the GGA-PBE functional [79]. We do carry out some test calculations where an additional Hubbard type +U correction term is included to check if the structure is sensitive to such correlations. The empirical +U term uses orbital dependent interactions to describe the strong in-site Coulomb interaction of localized electrons which may occur for d- and f-electrons.

Practical implementation of DFT

Two popular methods for describing the electron density; are the linear combination of atomic orbitals, LCAO, and plane waves, PW. Linearized augmented plane waves, LAPW, is a combination of the two methods. LCAO gives a good approximation to molecular orbitals and is therefore mostly used to study molecules. Plane-waves methods are mostly used for crystalline inorganic materials, because they are easy to implement and demand a smaller set of functions, which results in fast energy convergence. VASP, uses plane-waves as basis set, and a particular efficient implementation in VASP is the Projected Augmented Wave method, PAW[80], which is a generalization of the LAWP method and the use of pseudoptensials. In PAW, pseudopotentials are used to describe a simplified potential around the atomic core where the core electrons are described by the frozen-core approximation. In the frozen-core approximation only the outer electrons, such as the valence electrons, are included in solving the Kohn-Sham equations. The PAW method further includes a projection of the pseudopotentials into an all-electron wave function which gives a smooth plane-wave function throughout the system.

In order to reduce the computational effort needed to reach a satisfactory energy convergence, the plane-wave expansion can be limited to a maximum kinetic energy, E_{cut}. Additional simplifications can be made based on the similarity of wave functions close to each other in the Brillouin zone, and the system can be evaluated at a finite number of at **k**-points, instead of at an infinite number. The number of **k**-points needed in each orthogonal direction, the **k**-point density, is dependent on the cell size and a suitable k-point density that balance cost and accuracy can be found by analysing the convergence of the energy (and other properties) with number of k-points used.

Chosen ensembles and limitations

For structural relaxation in the static limit we can choose to relax the atomic positions by setting the volume constant (consistent with an MD carried out in the NVT ensamble) or to relax also the lattice constants as for constant pressure (in line with the use of NPT ensamble

in MD). Allowing for full relaxation of the structure, lattice parameters, cell volume, basic atomic positions, is preferred when searching for the ground state configuration. However, in many cases comparison of configurations and analysis of oxygen ordering in the oxygen sublattice is simplified by keeping the volume fixed (cubic) during the structural optimizations. We find that the relative order of the different configurations for $La_2Ce_2O_7$ and $Nd_2Ce_2O_7$ does not change when we carry out a full structural optimisation allowing both the cell volume and the cell shape to relax compared to if the volume is kept fixed The experimentally observed cubic lattice parameters with relatively sharp peaks in XRD and NPD support the idea that we can fix the cubic cell volume during the structural optimisations.

The cation and oxygen sites in the pyrochlore and C-type structure are quite comparable to the sites in the perfect fluorite as seen in Figure 1 a-c, the main difference is shifts of the sites and lower oxygen stoichiometry for pyrochlore and C-type structures. The alignments and ordering of the vacancies (vac-vac configurations) in the oxygen lattice are easily analysed by dividing the unit cell into boxes around the initial (oxygen) 8*c* sites in the perfect fluorite and identifying whether there is an oxygen atom there or not. We then identify the space group symmetry, the coordination numbers and the bond lengths of this configuration using PLATON [81]. The distance and direction between the vacancies are categorized with reference to the perfect fluorite. The notation representing the types of alignments between pairs of vacancies is <100>, <110>, <111>, <200> and so forth and refers to the distance and direction of a cube of oxygen positions with a cation site in the cube centre (e.g. a <111> vacancy pair will create an octahedron instead of a cube). Note, that since the counting method searches for vacant neighbours from each vacant cube, every pair will be counted twice.

DFT and thermodynamics

DFT calculations, as well as other atomistic simulation techniques, can be used to estimate the Gibbs energy of formation for defects and oxides [82-84] through the relationship to the equilibrium constant for the formation reaction, *K* (e.g. Equation (8) for the hydration reaction). That is, if we disregard the temperature dependent contributions and thermal expansion, the Gibbs energy for the defect formation, ΔG^{f}_{defect} , can be found by:

$$\Delta G^{f}_{defect} = E^{tot}_{defect} - E^{tot}_{perfect} - \sum_i \Delta n_i \mu_i + q_i(\epsilon_f + \Delta\epsilon) \quad (27)$$

where E^{tot}_{defect} and $E^{tot}_{perfect}$ is the total electronic energy of the defective and perfect supercell describing the energy difference with and without a defect, as described by Oba et al. [85]. The two latter contributions arise from species being incorporated or extracted during the defect reaction, where Δn_i is the change in number of species *i* with the chemical potential

μ_i, q_i is the effective charge of the defect and ϵ_f the Fermi level. $\Delta\epsilon$ is the shift in core potential in the defective cell compared to the perfect one [86]. If relaxations are carried out within the static limit, the entropy of the reaction is not included and the energy difference represents the enthalpy of formation. In order to calculate the hydration enthalpy in an acceptor doped oxide with a perfect structure we first determine the most favourable position of a charge compensating vacancy and proton. The most favourable defect position is assumed to be dominating and the energy of the cell containing a proton and a cell containing an oxygen vacancy can be used for the calculation of the hydration enthalpy. For the hydration reaction the chemical potential of water can be expressed as the total electronic energy of the pure phase; $\mu^{\circ}_{H2O} = \mathrm{E}^{\mathrm{tot}}_{\mathrm{H_2O}}$. Defect-defect interactions should be accounted for since the charged defect is periodically repeated in all directions.

This method is a valuable way of investigating the thermodynamics of defects formation in the dilute limit for a compound that initially has a perfect crystal structure. However, the oxygen deficient and disordered fluorites studied here, impose more challenges in the evaluation of the Gibbs energy. First, for these compounds the concentration of vacant oxygen sites in the fluorite structure is very high and we cannot simplify by assuming an isolated oxygen defect approximation. Vacancies co-exist in the supercell and this influences the structural relaxation and charge distribution and, hence, the total energy. Second, the effective charge of the vacancies is defined according to the perfect reference structure. Finding a perfect crystal structure can prove difficult and for these disordered fluorite compounds there are most likely several possible configurations that can co-exist in the relevant temperature regime for hydration. Using only the single most energetically favourable configuration we have been able to find from DFT, might be severely misleading unless we know for a fact that it represents the ground state. For $La_{28-x}W_{4+x}O_{54+\delta}$ the complex structure forces us to use the "perfect structure" of $La_{28}W_4O_{54}$ which is not stable, as the starting point for describing the defects caused by self-doping, resulting in oxide ions and vacancies with a charge less than +2 as described in the publication of Erdal et al. [41]. For these disordered systems one should calculate the energy of all possible configurations before and after hydration in order to determine the statistical hydration enthalpy. Including (configurational and vibrational) entropy would be even more challenging. This is in practice an enormous job when using DFT and has not been feasible within this study.

In this thesis we have done preliminary calculations in a number of supercell configurations with different oxygen and cation sublattices to illustrate the effects of vacancy ordering on the hydration properties in $La_2Ce_2O_7$ and $Nd_2Ce_2O_7$. We place two protons and one oxide ion into the crystal structure, which is the equivalent of hydration filling 12.5% of the vacancies. This also results in a neutral supercell and since electrons are not involved in the defect reaction, the bandgap and chemical potential of electrons need not be considered. In

order to predict favourable initial positions for the protons (distance and direction from adjacent oxygen) we used results from previous studies done on $La_2Ce_2O_7$ in the pyrochlore structure [32] and we avoid to position the protons in the vicinity of each other. Note that we have not performed tests to find converged calculations parameters and the results are thus preliminary giving us a first indication of trends and correlations, and are not meant to provide exact hydration enthalpies.

MD calculations using DFT

Ab-initio Born-Oppenheimer molecular dynamics follow the ionic motions by iteratively minimizing the electronic energy at each atomic step. The Born-Oppenheimer approximation assumes that the motion of the atomic nuclei and electrons can be treated separately due to the high difference in mass between the electrons and the nuclei. That is the electrons see the nuclei as stationary. Consequently the electrons will almost instantaneously respond to the forces and movement of the nuclei. The atomic movement is described by Nosé dynamics in a given ensemble [87, 88], for example the NVT ensemble, by adding a thermostat to the system.

Self-diffusion for mobile species can then be analysed based on the calculated jumping rate and jump distance in the MD calculations. Using MD-DFT calculations is mainly done for oxygen and protons as the system can be regarded as melted if also the cations start diffusing.

Generating PDF from DFT modelling:

Structure configurations obtained from DFT modelling can be used to provide atomic positions needed to calculate the pair distribution function (PDF), which is comparable to the total radial distribution function G(r) found from total scattering experiments. All the separation lengths between pairs of atoms in the configuration result in the partial radial distribution function $g_{ij}(r)$. By further applying the correct scattering lengths and concentrations we obtain the resulting G(r) which can be used for comparison to the G(r) from total neutron scattering.

DFT results of static relaxations (0 K) will result in peaks that will represent static pictures of atoms with no dynamical displacement from the origin of the position and become quite sharp with only static displacement contributing to any distribution of atomic positions. Only static disorder in the configuration will provide a distribution in the partial radial distribution function, creating less sharp peaks. The experimental results, on the other hand, reflect the conditions used during the scattering experiment at room temperature or similar. At these temperatures the atoms vibrate around their ground position creating a distribution around the position related to the oscillation. A generalized difference is illustrated in Figure 4.

To compare the experimentally and computationally obtained PDFs, there are two different approaches we have used in this work; 1) adding displacement factors to the static relaxation calculations creating Gaussian curves around the ground position (as in Paper IV) and 2) performing MD simulations in order to simulate atomic vibration (as in Paper I).

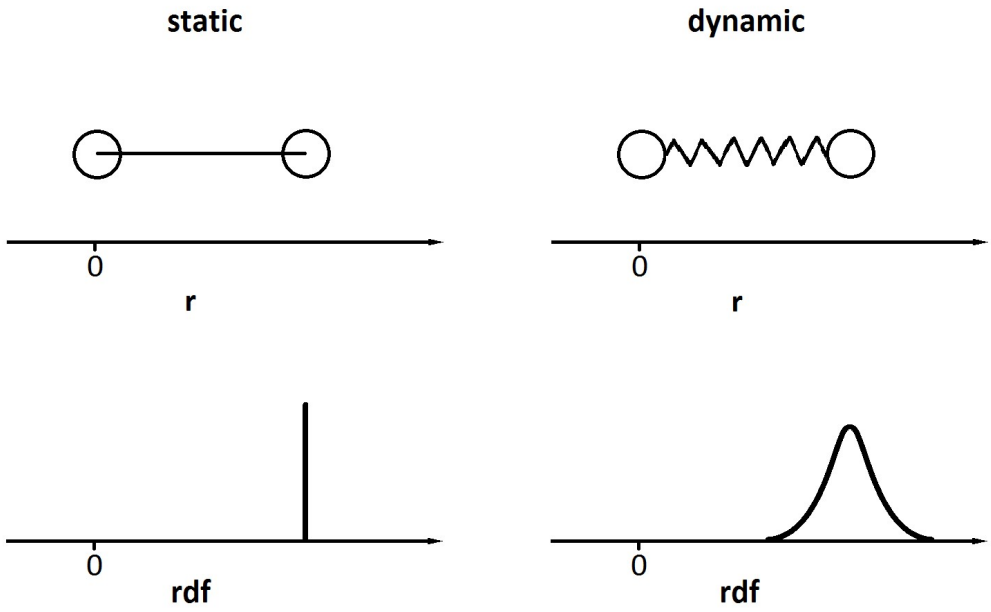

Figure 4 Schematic illustration of the connection between atomic movement and the resulting radial distribution function.

When Rietveld analysis of diffraction data is performed, the results include estimations of the atomic displacement factor for each atom from its crystallographic site. This displacement is either due to vibrations from the centred positions or from static displacement from a perfect position. Static relaxations of disordered structures such as those investigated in this work, often results in atoms with a wide range of displacements from perfect sites and lower symmetry. This diversity in positions and the resulting bond lengths are however a part of the reality. If using large enough supercells for the DFT calculations it can yield a good fit to the experimental distribution function by applying the atomic displacement factors (which could also be fitted) on the resulting positions. In Paper IV we used this method on $La_{28-x}W_{4+x}O_{54+\delta}$ (x = 1) and since the supercell is quite large 4x2x2 supercell of fluorite we obtain a lot of static disorder in the cation-oxide ion bonds of the configurations, which contribute to a good fit although the PDF has a lot of small details. However a large number of configurations were needed to understand the relationship between the different ways of arranging tungsten in the lattice and its surrounding oxygen nature and, further identify which configurations were most likely to

present in the oxide based on the comparison to the experimentally obtained distribution function.

In Paper I we use MD modelling of chosen structure configurations to obtain comparable distribution functions, a method used with success in previous works [89]. During the MD simulations atoms vibrate as they do at finite temperatures. The temperature used for the thermostat in the MD calculations should be comparable to the experimental one. Then the PDF obtained is based on both static displacements due to relaxation of the atomic positions as well as dynamic due to vibrations, and the result is only based on *ab initio,* or first principles, calculations.

The two approaches presented are useful methods to validate that PDFs from optimized configurations are consistent with the average structure in G(r) obtained by diffraction, and it further allows us to investigate indirectly how different local structures affect the average structure. Although the diffraction data may be unable to provide all details about the local structure, the average structure information obtained from diffraction acts as a frame to which the local structure models must fit. If there is a large mismatch between the obtained PDFs it is evident that the modelled structure configuration is not the dominating structure in the investigated sample.

4 Papers

I. **C-type related order in the defective fluorites $La_2Ce_2O_7$ and $Nd_2Ce_2O_7$ studied by neutron scattering and *ab initio* MD simulations**
L-E. Kalland, S. T. Norberg, J. Kyrklund, S. Hull, S. G. Eriksson, T. Norby, C. E. Mohn and C. S. Knee, Physical Chemistry Chemical Physics, 2016, 18, 24070-24080

II. **First principles calculations on order and disorder in $La_2Ce_2O_7$ and $Nd_2Ce_2O_7$**
L-E. Kalland and C. E. Mohn, Physical Chemistry Chemical Physics, 2020, 22, 13930-13941

III. **Structure, hydration, and proton conductivity in 50% La and Nd doped CeO_2 – $La_2Ce_2O_7$ and $Nd_2Ce_2O_7$ – and their solid solutions**
L-E. Kalland, A. Løken, T. S. Bjørheim, R. Haugsrud and T. Norby, Solid State Ionics, 2020, 354, 115401-115408

IV. **Local Structure of Proton-Conducting Lanthanum Tungstate $La_{28-x}W_{4+x}O_{54+\delta}$: a Combined Density Functional Theory and Pair Distribution Function Study**
L-E. Kalland, A. Magraso, A. Mancini, C. Tealdi, and L. Malavasi, Chemistry of Materials, 2013, 25 2378-2384

The work has also contributed to the following publications:

Defect structure and its nomenclature for mixed conducting lanthanum tungstates $La_{28-x}W_{4+x}O_{54+3x/2}$
S. Erdal, L-E. Kalland, R. Hancke, J. Polfus, R. Haugsrud and T. Norby
Int. J. Hydrogen Energy, 2012, 37(9) 8051-8055.

Complete structural model for lanthanum tungstate: a chemically stable hightemperature proton conductor by means of intrinsic defects
A. Magraso, J. M. Polfus, C. Frontera, J. Canales-Vazquez, L.E. Kalland, C. H. Hervoches, S. Erdal, R Hancke, M. S. Islam, T. Norby, R. Haugsrud, Journal of Materials Chemistry, 2012, 22 1762-1764

Paper I

C-type related order in the defective fluorites $La_2Ce_2O_7$ and $Nd_2Ce_2O_7$ studied by neutron scattering and *ab initio* MD simulations

L-E. Kalland, S. T. Norberg, J. Kyrklund, S. Hull, S. G. Eriksson, T. Norby, C. E. Mohn and C. S. Knee, Physical Chemistry Chemical Physics, 2016, 18, 24070-24080

DOI: 10.1039/c6cp04708d

PCCP

PAPER

View Article Online
View Journal | View Issue

Cite this: *Phys. Chem. Chem. Phys.*, 2016, **18**, 24070

C-type related order in the defective fluorites $La_2Ce_2O_7$ and $Nd_2Ce_2O_7$ studied by neutron scattering and *ab initio* MD simulations

Liv-Elisif Kalland,*[a] Stefan T. Norberg,[bc] Jakob Kyrklund,[d] Stephen Hull,[c] Sten G. Eriksson,[b] Truls Norby,[a] Chris E. Mohn*[ae] and Christopher S. Knee†[b]

This work presents a structural investigation of $La_{2-x}Nd_xCe_2O_7$ (x = 0.0, 0.5, 1.0, 1.5, 2.0) using X-ray powder diffraction and total scattering neutron powder diffraction, analysed using Rietveld and the reverse Monte Carlo method (RMC). *Ab initio* molecular dynamics (MD) modelling is also performed for further investigations of the local order. The main intensities in the neutron diffraction data for the $La_{2-x}Nd_xCe_2O_7$ series correspond to the fluorite structure. However, additional C-type superlattice peaks are visible for $x > 0$ and increase in intensity with increasing x. The Nd-containing compositions ($x > 0$) are best fitted with Rietveld analysis by using a combination of oxygen deficient fluorite and oxygen excess C-type structures. No indications of cation order are found in the RMC or Rietveld analysis, and the absence of cation order is supported by the MD modelling. We argue that the superlattice peaks originate from oxygen vacancy ordering and associated shift in the cation position away from the ideal fluorite site similar to that in the C-type structure, which is seen from the Rietveld refinements and the observed ordering in the MD modelling. The vacancies favour alignments in the ⟨110⟩, ⟨111⟩ and especially the ⟨210⟩ direction. Moreover, we find that such ordering might also be found to a small extent in $La_2Ce_2O_7$, explaining the discernible modulated background between the fluorite peaks. The observed overlap of the main Bragg peaks between the fluorite and C-type phase supports the co-existence of vacancy ordered and more disordered domains. This is further supported by the observed similarity of the radial distribution functions as modelled with MD. The increase in long range oxygen vacancy order with increasing Nd-content in $La_{2-x}Nd_xCe_2O_7$ corresponds well with the lower oxide ion conductivity in $Nd_2Ce_2O_7$ compared to $La_2Ce_2O_7$ reported earlier.

Received 6th July 2016,
Accepted 5th August 2016

DOI: 10.1039/c6cp04708d

www.rsc.org/pccp

1 Introduction

Rare earth doped ceria has a variety of applications within oxygen sensors, solid oxide fuel cells (SOFCs) and catalysis. The electrochemical properties and structure of doped ceria are studied with as much interest now[1–4] as a couple of decades ago.[5–8] The reduction and oxidation properties of ceria, its structural stability to changes in cation–oxygen stoichiometries and its ability to accommodate high concentrations of aliovalent dopants, make this compound highly versatile as an oxide ion conductor. However, at doping levels above ~15–20 mole% the ionic conductivity decreases.[8,9] Changes in the degree of local ordering, or clustering, are often suggested to rationalize the variations in the conducting properties with composition.[9–11] Identifying the underlying atomic structure is consequently essential to explain these macroscopic properties.

Ceria (CeO_2) possesses the perfect fluorite structure (space group $Fm\bar{3}m$) with both of the Wyckoff sites 4a and 8c being fully occupied (see Fig. 1b), and exhibits high solubility of C-type structured rare earth sesquioxides $RO_{1.5}$ (space group $Ia\bar{3}$, *e.g.* Y_2O_3, see Fig. 1a). Fluorite structured oxides were commonly believed to exhibit a third nearest neighbour ordering of the oxygen vacancies (*i.e.* ⟨111⟩ alignment within the oxygen cube around a cation‡) when sufficiently oxygen deficient.[12,13]

[a] *Centre for Materials Science and Nanotechnology, Department of Chemistry, University of Oslo, FERMiO, Gaustadalléen 21, NO-0349 Oslo, Norway. E-mail: l.e.kalland@smn.uio.no, c.e.mohn@geo.uio.no*
[b] *Department of Chemistry and Chemical Engineering, Chalmers University of Technology, SE-412 96 Gothenburg, Sweden*
[c] *The ISIS Facility, STFC Rutherford Appleton Laboratory, Chilton, Didcot, OX11 0QX, UK*
[d] *Department of Chemistry, University of Gothenburg, SE-405 30 Gothenburg, Sweden*
[e] *Center for Earth Evolution and Dynamics, University of Oslo, NO-0371 Oslo, Norway*
† Present address: ESAB AB, Lindholmsallén 9, SE-402 77 Gothenburg, Sweden.

‡ Note that ⟨111⟩ is the group of directions and the correct vector for this vac–vac distance in the fluorite structure would be 1/2 × ⟨111⟩, and for the pyrochlore 1/4 × ⟨111⟩. However, to avoid confusion when comparing different unit cells we only use the group of directions related to an oxygen cube as illustrated in Fig. 1.

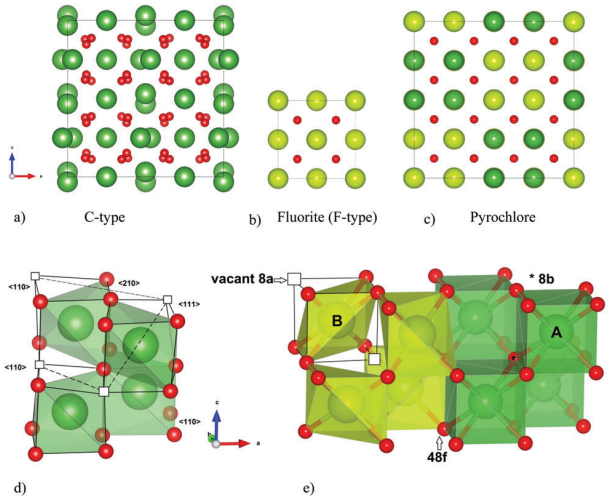

Fig. 1 The (a) C-type and (c) P-type (pyrochlore) compared to the parent structure (b) F-type (perfect fluorite). Coordination polyhedron and vacancy alignment ⟨111⟩, ⟨110⟩ and ⟨210⟩ in C-type (d), and (e) ⟨111⟩ in pyrochlore. All crystal structures are drawn with VESTA.[42]

This is indeed the case for $CeO_{2-\delta}$ when $\delta > 0.3$,[14] and such local vacancy ordering explains the significant decrease in oxide ion conductivity.[11,15] However, a former detailed analysis of the superstructure observed for CeO_2 doped with ~50 mole% $YO_{1.5}$ suggests that vacancy ordering exclusively in the ⟨111⟩ direction is not always the situation, and it is necessary to also consider other ordering possibilities.[6]

In this study we focus on two ceria-based systems, $La_2Ce_2O_7$ and $Nd_2Ce_2O_7$, and their intermediate phases ($La_{2-x}Nd_xCe_2O_7$). La_2O_3 and Nd_2O_3 possess the hexagonal A-type structure, rather than the cubic C-type structure. Nonetheless, when ceria is doped with La_2O_3 and Nd_2O_3 the trends in conductivity and lattice parameter due to doping levels are similar as when ceria is doped with C-type sesquioxides.[9,10,16] $La_2Ce_2O_7$ and $Nd_2Ce_2O_7$ are proposed as systems on the verge of transitioning into more ordered superstructures of the perfect fluorite structure; the pyrochlore and C-type structure respectively (see Fig. 1a–c). $La_2Ce_2O_7$ is most often reported as a disordered fluorite,[17–20] although a pyrochlore structure ($A_2B_2O_7$, space group $Fd\bar{3}m$) has also been advocated.[21] $Nd_2Ce_2O_7$ is reported as a more long range ordered system where C-type supercell diffraction patterns are observed.[9,17] Long range order will affect the conductivity properties of the compositions. The ionic conductivity is lower in $Nd_2Ce_2O_7$ compared to $La_2Ce_2O_7$[19,22] and we expect a decreasing oxygen ion conductivity with increasing Nd-content in $La_{2-x}Nd_xCe_2O_7$. Thus, a structural investigation of these systems can further elucidate the ordering mechanism for heavily doped ceria, as well as the effect of the average dopant size, and link variations in ionic conductivity to structural changes.

This work is part of a larger investigation, relating structure to hydration and conductivity properties, and the principal objective of this study is to capture local changes in the ordering patterns when going from $La_2Ce_2O_7$ with a disordered fluorite structure, to $Nd_2Ce_2O_7$ where superlattice diffraction peaks are observed. Both long and short range crystal structure of five different compositions of $La_{2-x}Nd_xCe_2O_7$ are studied (x = 0.0, 0.5, 1.0, 1.5, 2.0). The Rietveld method is used to analyse the long range order observed with powder X-ray diffraction (PXRD) and powder neutron diffraction (NPD) data. The local order is investigated with a reverse Monte Carlo (RMC) method to analyse both the Bragg and diffuse intensities based on the scattering factor $S(Q)$ and the real space radial distribution function $G(r)$ obtained by total scattering NPD. To further look at possible local order and investigate the preferred oxygen vacancy clustering, *ab initio* molecular dynamics (MD) modelling studies are performed.

2 Experimental and computational details

2.1 Synthesis

$La_{2-x}Nd_xCe_2O_7$ compositions in the range x = 0.0, 0.5, 1.0, 1.5 and 2.0 were prepared *via* solid state reaction of stoichiometric amounts of La_2O_3, Nd_2O_3 (both 99.99% Sigma Aldrich) and CeO_2 (99.9% Alfa Aesar). The reactants were dried at 800 °C prior to weighing and mixed under ethanol using an agate-mortar and pestle. The powders were then heated in high density and purity alumina crucibles at 1050 °C for 20 h, and subsequently at 1200 °C and 1300 °C for 8 h durations with re-grinding steps. The samples were then pressed into pellets (9/8 inch diameter) under a load of 20 tons and heated to 1400 °C for 8 h and subsequently grinded. This step was repeated three times, with the final heating time extended to 16 h, to yield phase pure samples as judged by Rietveld analysis of long scan PXRD data.

2.2 Structural characterisation

The long scan PXRD data were collected on a Bruker D8 Advance operating with Cu $K_{\alpha 1}$ radiation in the 2θ range 19° to 100° with a step size of 0.009° and count time of 4 s per step. The five samples were placed into thin walled vanadium cans of 8 mm diameter and loaded into a sample changer, along with an empty vanadium can for background correction. The neutron diffraction data was collected at room temperature on the newly upgraded Polaris diffractometer of the ISIS facility, Rutherford Appleton Laboratory, U.K., using the backscattering detector bank covering angles of ($135° < 2\theta < 167°$), the 90° detector bank ($75° < 2\theta < 113°$), and the two low angle detector banks ($40° < 2\theta < 66°$) and ($19° < 2\theta < 34°$), respectively. These cover a total range of 0.2–60 $Å^{-1}$ for the scattering vector Q (where $Q = 2\pi/d$ and d is the interplanar spacing). The measurements took approximately 6 hours in order to obtain counting statistics of sufficient statistical quality to allow analysis of the total scattering. The PXRD data and NPD data from the 90° detector (bank 4, providing the optimum balance of resolution and wide d-spacing range to cover all main reflections from the phases), were analysed with the Rietveld[23] method using the GSAS program.[24]

The NPD data from each detector bank were merged to form a single spectrum covering a wide Q range using the program Gudrun,[25] after background scattering and beam attenuation

correction. This process puts the scattered intensity onto an absolute scale of scattering cross-section. The resultant normalized total scattering structure factor, $S(Q)$, was used to generate the corresponding total radial distribution function, $G(r)$, *via* a Fourier transform (for details, see Keen[26]).

The $G(r)$ can also be expressed as the sum of the individual partial radial distribution functions, $g_{ij}(r)$, weighted by $c_i c_j \bar{b}_i \bar{b}_j$, where c_i and $\bar{b}_i$ are the concentration and the coherently bound neutron scattering lengths, respectively, for the species i. The partial radial distribution function can be extracted from the RMC modelling results, and is, in turn, given by

$$g_{ij}(r) = \frac{1}{4\pi r^2 \Delta r} \frac{n_{ij}(r)}{\rho_j}, \quad (1)$$

with $n_{ij}(r)$ equal to the number of atoms of type j located at a distance between r and $r + \Delta r$ from an atom of type i, and ρ_j is the number density of atoms of type j, given by $\rho_j = c_j \rho_0$.

RMC modelling of the neutron total scattering data was performed using the RMCProfile software.[27] A bond valence sum (BVS) soft constraint[28] was used to ensure that individual cation–anion coordination environments remain chemically reasonable, with parameters taken from Brese and O'Keefe.[29] The RMC modelling used both reciprocal space data, $S(Q)$, and real space data, $G(r)$. The former emphasises the long-range ordering, while the $G(r)$ focuses on the short-range interactions. Additionally, the $S(Q)$ used for RMC modelling is broadened by convolution with a box function to reflect the finite size of the configuration box (for details, see Tucker *et al.*[27]). An $8 \times 8 \times 8$ fluorite supercell was used as the initial atomic configuration for $La_{2-x}Nd_xCe_2O_7$ with $x = 0$, 0.5 and 1, with the vacancies and cations randomly distributed. For the more Nd-containing systems, $x = 1.5$ and 2.0, a $4 \times 4 \times 4$ C-type supercell with oxygen excess and randomly distributed cations was used. To test cation clustering preference a second set of modelling (RMC2) was performed on the end members $La_2Ce_2O_7$ and $Nd_2Ce_2O_7$, with the same initial configuration as previously mentioned, where cation swapping was allowed. Also the pyrochlore structure was tested as an initial configuration in a third set of RMC modelling (RMC3). Finally, a total of 10 RMC runs were performed to improve the statistical significance of extracted results, using the fitted configuration but with different seeds for the random number generator.

2.3 *Ab initio* molecular dynamics

Ab initio Born–Oppenheimer molecular dynamics was carried out within the *NVT* ensemble, with a step length of 2 fs, to investigate the local nature of different possible configurations. The temperature was controlled by a Nosé thermostat.[30,31] Only the end members, $La_2Ce_2O_7$ and $Nd_2Ce_2O_7$, were studied in detail using a careful selection of representative start configurations as described below. The structure, such as the partial radial distribution functions $g(r)$, was analysed by sampling many configurations during the MD run. From the $g(r)$s we calculate the neutron weighted total $G(r)$. Since there is no ionic migration occurring in MD runs at 300 K, we obtain the $G(r)$ resulting from the atomic positions for a fixed configuration of cations and oxygen and the dynamic vibrations similar to the experimental conditions from 10 ps long runs. Comparison of the obtained $G(r)$ gives us insight into the influence of different configurations on vibrational properties. The sampled configurations are studied using PLATON[32] to extract atomic distances and other relevant crystallographic data.

To collect sufficient statistics on coordination numbers and preferred vacancy orientation, MD runs at 1500 K have also been carried out. At this temperature the oxygen are migrating in the structure during the MD run, and several configurations of the oxygen lattice were sampled. Four different starting configurations with randomly distributed cations were used, giving statistics from a total of 0.64 ns after 0.04 ns of equilibration, for each composition (50 ps long MD runs were also performed on $3 \times 3 \times 3$ super cells). The location of the vacant oxygen sites was sampled to analyse the vacancy–vacancy (vac–vac) distribution in terms of distance and direction. The latter analysis has been done by dividing the whole simulation cell into space filling cubic boxes where each box contains one of the initial oxygen sites (*i.e.* the 8c position in $Fm\bar{3}m$). The vacant boxes and the distribution of vac–vac pairs from each box aligned in ⟨100⟩, ⟨110⟩, ⟨111⟩, ⟨200⟩, ⟨210⟩, ⟨211⟩ or ⟨220⟩ manner, are then identified. This resembles a pair distribution function with discrete distances for each type of pairs.

All MD runs were performed using the projector augmented wave (PAW)[33] method as implemented in the VASP code.[34] The generalized gradient approximation functional by Perdew, Burke and Ernzerhof (GGA-PBE)[35] was employed using a plane wave cut-off energy at 400 eV, and only the gamma point to sample the Brillouin zone. All MD runs have been performed at constant volume with a $2 \times 2 \times 2$ supercell ($N = 88$) of the cubic fluorite structure, which is equivalent to the size of a single unit cell of pyrochlore or C-type structure, using the cell parameters obtained experimentally from initial X-ray Rietveld refinements (*i.e.*, $a_{supercell} = 2 \times a_{fluorite} = 11.1325$ Å for $La_2Ce_2O_7$ and $a_{supercell} = 10.9639$ Å for $Nd_2Ce_2O_7$). To investigate the possible limitations due to the cell size, $3 \times 3 \times 3$ supercells with randomly distributed atoms within the fluorite structure were also used.

The start configurations chosen for the MD runs were based on those suggested in literature, random distribution configurations, and low energy configurations found within the static limit from full structural optimization. The configurations are described as combinations of different possible cation and anion sub-lattices. The cation sub-lattices were either exhibiting a random distribution, or a pyrochlore order. These cation sub-lattices were thereafter combined with an oxygen lattice with the 56 oxygen atoms randomly distributed on the 8c site. Two types of oxygen order were also tried; (1) one order in a manner similar to the C-type, and (2) an order proposed by Withers *et al.*[6] The first ordering scheme is related to the C-type structure where 8 of the positions equal to the 16c are vacant such that every second plane in the [001] direction has 4 vacant positions (see Fig. 2). This distribution results in a combination of ⟨110⟩ and ⟨210⟩ alignments between vacancies, but zero ⟨111⟩ alignments, which also would be present in the perfect

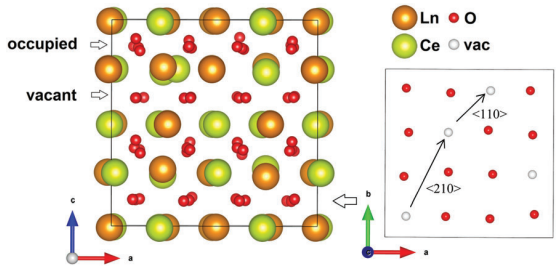

Fig. 2 Showing the order in the oxygen sub-lattice for one of the two (004) planes with vacant 16c positions in the chosen ordered oxygen configuration related to the C-type structure.

C-type structure. The second ordered arrangement is based on a tetragonal structure proposed by Withers *et al.* after TEM investigations, and the vacancies are ordered in a ⟨210⟩ manner in combination with ⟨200⟩ and ⟨220⟩ when translated into a cubic fluorite supercell.[6] For $La_2Ce_2O_7$ the perfect pyrochlore structure has also been tried.

3 Results and discussion

3.1 Rietveld refinement based on XRD and ND – long range order

The long scan PXRD data were analysed using the Rietveld method with the oxygen deficient, disordered fluorite structure (space group $Fm\bar{3}m$) previously reported for $La_2Ce_2O_7$[19] as the input for the initial model. This provided an adequate fit to the data sets, however, for the $x \geq 1.5$ samples, additional weak reflections consistent with a C-type structure (space group $Ia\bar{3}$) were apparent (see Fig. 3). The oxygen excess C-type structure reported for $Gd_{1-x}Ce_xO_{1.5+x/2}$[36] modified to give the correct Nd to Ce ratio was therefore used as the starting point for an analysis of $Nd_2Ce_2O_7$ that provided a satisfactory fit to the data set.

In contrast with the PXRD data, the neutron patterns revealed the emergence of the C-type supercell peaks occurring for lower x in $La_{2-x}Nd_xCe_2O_7$. As shown in Fig. 4, supercell intensity is apparent for $x \geq 0.5$, and the peaks associated with the doubled unit cell grow strongly with increasing Nd-content. Given the much greater sensitivity of the neutron diffraction data to the oxygen ion sub-lattice compared to the PXRD data, the following detailed structural investigations will focus exclusively on these data. Analysis of the neutron diffraction data proceeded using the models obtained from the PXRD as input with an initial focus on the end members $La_2Ce_2O_7$ and $Nd_2Ce_2O_7$.

The $La_2Ce_2O_7$ PND data was analysed successfully based on the disordered fluorite structure, with $Fm\bar{3}m$ symmetry, consistent with all previous neutron diffraction studies.[19,20,37] Refinement of the oxygen site occupancy yielded a value of 0.875(3) consistent with the nominal value 0.875, and the average structure of $La_2Ce_2O_7$ is best described as a cation disordered, oxygen deficient fluorite. In particular, no evidence for a pyrochlore superstructure characterised by perfectly ordered La and Ce positions that was predicted by DFT simulations of VanPoucke *et al.*[21] was found.

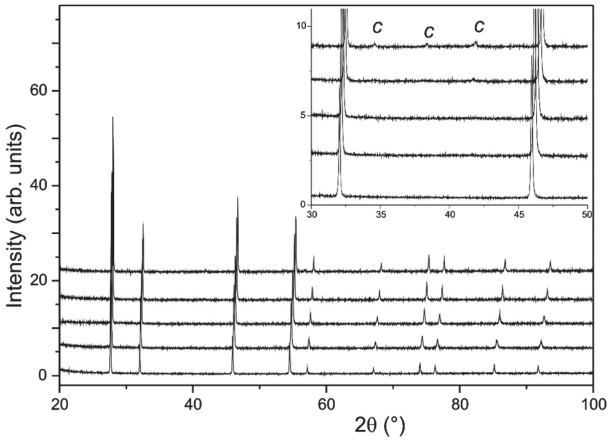

Fig. 3 Long scan PXRD data from $La_{2-x}Nd_xCe_2O_7$. Data is shown for x = 2.0 (top) to x = 0.0 (bottom). Inset shows the appearance of weak superlattice peaks from the C-type structure for the x = 1.5 and x = 2.0 samples.

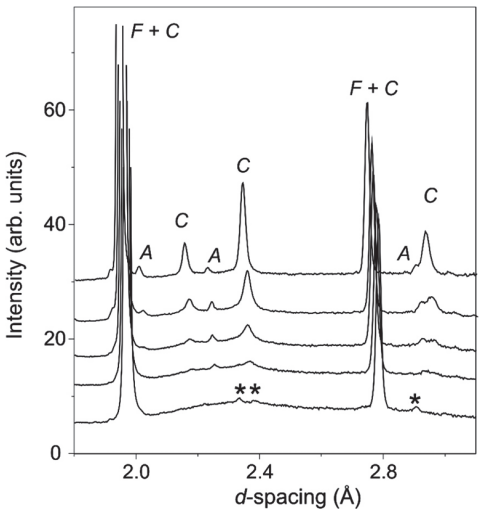

Fig. 4 Selected region of the diffraction patterns obtained from detector bank 4 of the Polaris neutron diffractometer. Data is shown in for $La_{2-x}Nd_xCe_2O_7$ for x = 2.0 (top) to x = 0.0 (bottom). Intensity from the C-type structure is labelled with a C and C + F where it coincides with the F-type fluorite peaks, and that arising from the minor A-type phase is labelled with an A. $La_{9.33}(SiO_4)_6O_2$ peaks are indicated by *.

As noted previously[19,20] the neutron diffraction pattern of $La_2Ce_2O_7$ displayed a strongly modulated background as seen in Fig. 4, indicative of significant deviations from the long range average structure determined from fitting of the Bragg diffraction intensities. The amplitude of the modulated background increased with the amount of La in $La_{2-x}Nd_xCe_2O_7$, and the broad humps were situated in the same region as the obtained C-type peaks which were diminishing. We therefore argue that the local structure of $La_2Ce_2O_7$ and the Nd-containing systems are similar and that therefore any ordering is likely to be of the same kind in the two compositions – the only difference being that in Nd-containing systems the ordering tendency is

more profound and the atoms crystallize in domains or phases to a larger extent producing well defined Bragg peaks (*i.e.* the incipient local order in $La_2Ce_2O_7$ is similar to ordering in $Nd_2Ce_2O_7$).

The modulated background was modelled using the shifted Chebyshev background function with the maximum number of 36 variables, and a close inspection of the diffraction pattern revealed very weak additional peaks in the *d*-spacing range 2–3 Å as is apparent in Fig. 4. These were found to originate from a silicate based apatite phase with an approximate composition of $La_{9.33}(SiO_4)_6O_2$[38] introduced from reaction of La_2O_3 and the agate material of the mortar and pestle used during the synthesis process. This phase also accounts for the peak seen in the long scan PXRD data at $2\theta \approx 30.5^\circ$ (Fig. 3). The phase was introduced into the Rietveld refinement and a refined content of 0.05 wt% was obtained, and we are therefore confident that it has a negligible influence on the stoichiometry of the disordered fluorite.

The diffraction pattern from $Nd_2Ce_2O_7$ was initially analysed with the oxygen excess C-type structure with the additional oxide ion, located at the 16c site ($Ia\bar{3}$ space group) and the cations statistically disordered over the 24d and 8b sites as suggested by Grover *et al.*[36] This produced a moderate quality fit to the data, with significant discrepancies between the calculated and observed intensities; in particular the relatively weak supercell reflections associated with the doubled fluorite cell were overestimated. Therefore, a two phase approach with the oxygen excess C-type and disordered fluorite phases was introduced, and a significant improvement to the agreement factors resulted with an approx. 50 : 50 distribution of the fluorite and C-type phase as judged by the refined weight fractions. Both phases contribute to the main intensity (fluorite 200, 220... *etc.*) and this leads to a high degree of correlation between the parameters. Nonetheless, through careful refinement it was possible to introduce the atomic variables from each phase, with particularly significant improvements in the fit associated with modelling the displacements of the 24d cation and 48e and 16c oxygen sites in the C-type structure.

Furthermore, the possibility of cation ordering was investigated by setting the extremes of the 8b site being occupied either completely by Nd or Ce ions with the occupancy of the 24d site adjusted to retain an overall 1 : 1 ratio of Nd and Ce, but this produced no evidence of long range cation ordering. Moreover, no significant deviation between the cation stoichiometry of the C-type related and disordered fluorite components were apparent from the Rietveld analysis.

Tests were also carried out to probe the most favourable location of the oxygen vacancy within the C-type structure, and a strong preference for deficiency on the 16c site was obtained. In particular the 321 reflection at *d*-spacing 2.9 Å was found to be sensitive to the occupation factor, *n*, of this position. Simultaneous refinement of *n* and the atomic displacement parameter (ADP) yielded a reduction to an approximate 0.4 occupancy that, combined with the full occupancy of the 48f site, would result in a significant deficiency, *e.g.* $\delta \approx 0.2$ for $Nd_2Ce_2O_{7-\delta}$. Given the high degree of correlation between *n* and the ADP, the occupancy factor was therefore set to 0.5 in the final cycles in order to preserve the expected O_7 stoichiometry.

From Fig. 4 it is clear that the relative intensities of the C-type peaks present in the intermediate compositions are more or less invariant, and we therefore judged that the type of oxygen vacancy order is also constant in the C-type related phase present in the $La_{2-x}Nd_xCe_2O_7$ samples where $0.5 \leq x \leq 1.5$. This was confirmed by the refinements of these samples which preceded using a statistical distribution of the three cationic species at the available cation positions. Given both the previously noted degree of correlation between the atomic parameters in the fluorite and C-type related phases, and the rapid decay of the C-type related phase with increasing lanthanum content, it was only possible to fully refine all atomic parameters of the C-type phase for the $x = 1.5$ and 2.0 data sets. For the $x \leq 1.0$ samples the ADPs of all sites in the C-type phase were set equal to unity. For the sake of completeness the minor Nd_2O_3 component (hexagonal A-type fluorite structure) present in all the Nd-containing samples was also modelled. Refinement of the data results in a content of 0.002–0.004 wt% of Nd_2O_3, which is too small to significantly impact the main phase compositions.

The refined structural parameters obtained from the Rietveld analyses are presented in Table 1. Fig. 5 shows the final Rietveld fit of the $Nd_2Ce_2O_7$ data. Note that the high χ^2 factors listed in Table 1 reflect the imperfect modelling of the modulated backgrounds and the quality of fit to the Bragg diffraction intensities is good as judged by the R_{wp} factors. The composition of the samples, extracted from the refined phase fractions of the fluorite and C-type phases, is presented in Fig. 6a, and the evolving cell parameters of the $La_{2-x}Nd_xCe_2O_7$ series are shown in Fig. 6b.

3.1.1 One or two phase approach. The two-phase approach (when disregarding the small amount of parasitic A-type structured phase) used for all the Nd-containing samples to reach the best Rietveld refinements can be consistent with two possibilities from a micro and macro structural viewpoint; (1) segregation of two phases with different symmetry, fluorite and C-type, exhibiting different cation and oxygen stoichiometries, or (2) existence of domains with oxygen vacancy ordering (sufficiently large to produce C-type supercell Bragg reflections) within the otherwise disordered fluorite structure. The latter case could be due to a kinetic limitation of either nucleation and growth of a C-type related structure (*i.e.*, second order phase transition), or an order–disorder transition within the oxygen lattice as described by the Bragg–Williams model.[39] No indications of compositional variation were found in the Rietveld refinements, and the lack of significant compositional segregation is supported by the minimum deviation between the cell parameters of the refined C-type and fluorite structure. The proposed co-existence of structures with an ordered and disordered oxygen lattice describes a system balanced between enthalpic and entropic terms. Therefore the thermal history will be crucial for the amount of supercell formation and that will explain the discrepancies between different studies involving the same compositions. In this study the refined C-type phase in $Nd_2Ce_2O_7$ comes out as more than 50 wt%, whereas a similar study done by Hagiwara *et al.* obtained ~32%.[9] The increased intensity of the supercell peaks when comparing PND

Table 1 Refined structural parameters for the $La_{2-x}Nd_xCe_2O_7$ series obtained from neutron diffraction data

	$La_2Ce_2O_7$	$La_{1.5}Nd_{0.5}Ce_2O_7$	$LaNdCe_2O_7$	$La_{0.5}Nd_{1.5}Ce_2O_7$	$Nd_2Ce_2O_7$
Fluorite phase					
Ln/Ce(1) 4a (0, 0, 0)					
$U_{iso} \times 100$ (Å^2)	1.905(14)	1.75(2)	1.98(3)	2.06(6)	2.07(9)
O(1) 8c (1/4, 1/4, 1/4)					
$U_{iso} \times 100$ (Å^2)	3.88(2)	3.71(2)	3.96(5)	3.88(9)	3.89(13)
Occupancy, n	0.875(3)	0.864(3)	0.874(4)	0.876(6)	0.863(10)
a (Å)	5.52429(3)	5.51031(8)	5.48810(6)	5.4693(1)	5.4437(2)
Wt%	100	94.3(1)	80.1(3)	73.4(4)	41.6(8)
C-type related phase					
Ln/Ce(1) 8b (1/4, 1/4, 1/4)					
$U_{iso} \times 100$ (Å^2)	—	1.0[a]	1.0[a]	1.8(4)	1.64(20)
Ln/Ce(2) 24d (x, 0, 1/4)					
x	—	−0.0215(18)	−0.0208(8)	−0.0194(6)	−0.0187(3)
$U_{iso} \times 100$ (Å^2)	—	1.0[a]	1.0[a]	0.25(8)	0.63(6)
O(1) 48e (x, y, z)					
x	—	0.3819	0.3834(6)	0.3837(4)	0.3825(3)
y	—	0.1422	0.1392(6)	0.1404(5)	0.1415(3)
z	—	0.3821	0.3836(5)	0.3829(4)	0.3821(2)
$U_{iso} \times 100$ (Å^2)	—	1.0[a]	1.0[a]	0.90(9)	1.15(6)
Occupancy, n	—	1.0	1.0	1.0	1.0
O(2) 16c (x, x, x)					
x	—	0.3842	0.3838(13)	0.3852(10)	0.3848(6)
$U_{iso} \times 100$ (Å^2)	—	1.0[a]	1.0[a]	1.3(3)	1.4(2)
Occupancy, n	—	0.5[b]	0.5[b]	0.5[b]	0.5[b]
Wt%	0.0	5.6(9)	19.6(7)	26.2(7)	58.1(5)
a (Å)	—	11.017(2)	10.9814(8)	10.9441(5)	10.8853(3)
R_{wp} (%)	2.52	3.02	3.30	3.15	3.21
χ^2	31.47	93.25	48.22	65.99	53.78
Variables	46	46	54	57	60

[a] ADP was not possible to refine. [b] In all cases a decrease in occupancy factor n was obtained and to maintain overall oxygen stoichiometry n was fixed at 0.5.

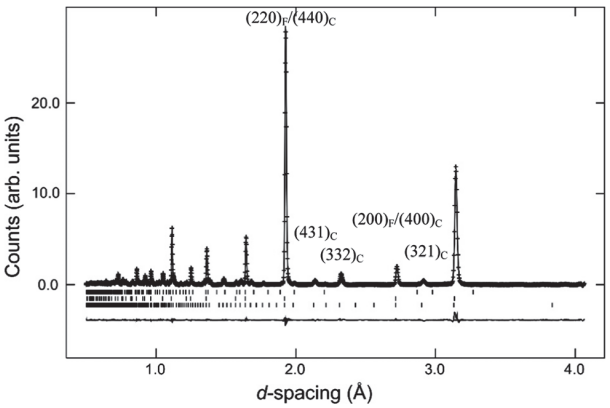

Fig. 5 Rietveld fit achieved to the neutron diffraction data from $Nd_2Ce_2O_7$. Crosses are observed data points, upper continuous line is the simulated diffraction profile and the lower continuous line is the difference between observed and calculated intensity. Vertical bars indicate the position of allowed diffraction peaks for $Nd_2Ce_2O_7$ (C-type), $Nd_2Ce_2O_7$ (fluorite) and Nd_2O_3 from bottom to top, respectively.

to PXRD data also suggests that the oxygen lattice is the key to the observation of a superstructure within these compositions. We therefore believe that there are two set of domains, with and without ordering, exhibiting close to the same stoichiometry. Further we believe the symmetry change is mainly due to oxygen vacancy ordering and proceed to discuss the local ordering.

3.2 Radial distribution functions – short range ordering

The total radial distribution functions, $G(r)$, obtained experimentally for the different compositions of $La_{2-x}Nd_xCe_2O_7$ are strikingly similar, as seen in Fig. 7. The peaks become slightly sharper when moving from $La_2Ce_2O_7$ to $Nd_2Ce_2O_7$ (see indent in Fig. 7), which could be interpreted as increasing configurational order or stiffer bonds. In addition, the peak positions are moved to lower r values due to the decreasing lattice parameter.

3.2.1 Distribution functions from RMC modelling. The $G(r)$ from RMC models are in good agreement with those obtained directly from experimental PND data (RMC set 1 is shown in indents in Fig. 8 for $La_2Ce_2O_7$ and $Nd_2Ce_2O_7$), and the RMC models for all five compositional systems predict a disordered fluorite structure. A test calculation where the cations are allowed to exchange cation positions gives no indication of cation clustering (RMC set 2), and a test calculation using a pyrochlore structure (RMC set 3) showed that such a model was not consistent with the collected data. The coordination numbers for the cations, listed in Table 2, are closest to 7, as expected from a random distribution of cations.

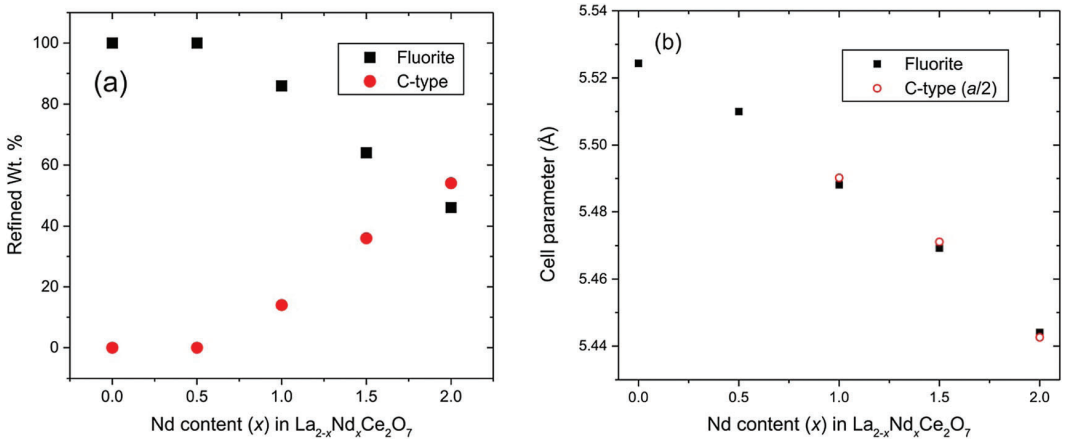

Fig. 6 (a) Refined content of disordered fluorite and C-type structure determined from Rietveld analysis of NPD data. (b) Cell parameters obtained from Rietveld analysis for fluorite and C-type phases. Cell parameters of C-type phases are divided by 2 to give direct comparison with the fluorite component. The error bars in both plots are smaller than the symbols.

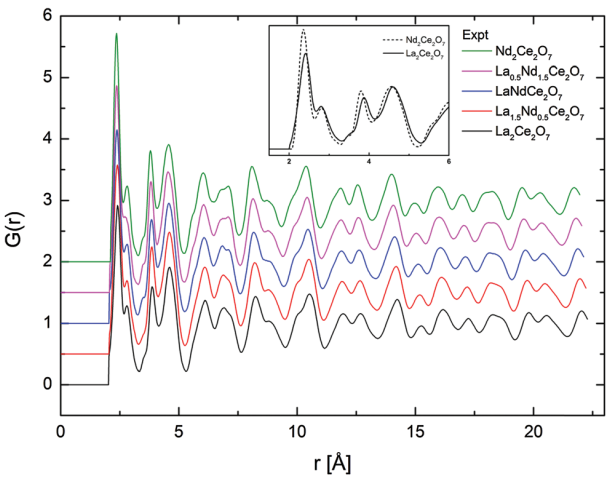

Fig. 7 $G(r)$ obtained from total scattering neutron diffraction for all compositions and for the two end-members at short r in inset.

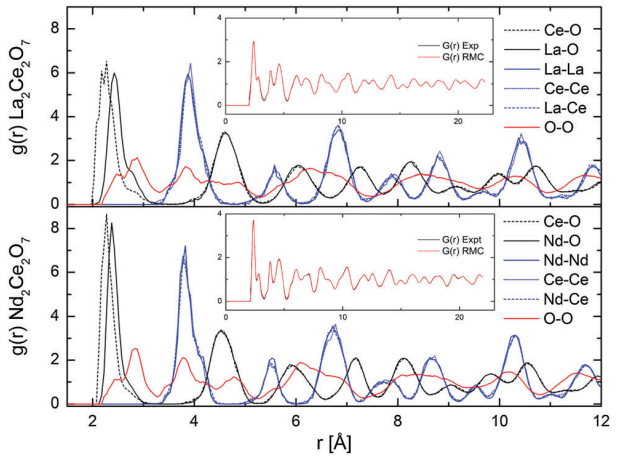

Fig. 8 Partial $g(r)$ from RMC (RMC set 1), and comparison of $G(r)$ from experimental NPD results and RMC fit (in inset), for $La_2Ce_2O_7$ and $Nd_2Ce_2O_7$.

The partial distribution functions, $g_{ij}(r)$, for the two end members $La_2Ce_2O_7$ and $Nd_2Ce_2O_7$ are shown in Fig. 8. Here we see that the difference between the $Ln_{(La/Nd)}$–O and Ce–O distance is smaller in $Nd_2Ce_2O_7$ since the ionic radii of Ln and Ce become more equal,[40] and thus the lattice strain decreases. When comparing the end members the first partial $g_{Ln/Ce-O}(r)$ and $g_{O-O}(r)$ peaks are broader in the $La_2Ce_2O_7$ system, pointing to either larger amplitudes of vibration in $La_2Ce_2O_7$ or more spread out oxygen positions and varying bond lengths between cations and oxygen compared to $Nd_2Ce_2O_7$. The partial $g_{O-O}(r)$s has a shoulder on the first peak in both $La_2Ce_2O_7$ and $Nd_2Ce_2O_7$, at around 2.5 Å, which could indicate that a fraction of the oxygen is more strongly correlated. However, the MD modelling does not support a structural model containing these split O–O as we will see later.

None of the RMC results showed any particular tendency for ordering within the sub-lattices for any of the systems. However, it is worth bearing in mind that RMC tends to give the most disordered configuration that is consistent with the experimental data as it is a Monte Carlo method. If there are only domains exhibiting ordering, the PND data might contains insufficient information for the RMC to capture any local ordering. However, an important observation, is that the peaks in the partial $g(r)$s become sharper when moving from $La_2Ce_2O_7$ to $Nd_2Ce_2O_7$, and this is either due to decreasing dynamic vibrations or static disorder. The latter is best described as more localised atom positions. Consequently we turn to MD modelling to investigate possible configurations that could result in similar $G(r)$ profiles.

3.2.2 Distribution functions from MD. Since no oxygen migrate in the MD simulations at 300 K, the obtained distribution functions allow us to study how the different oxygen and cation configurations influence the total and partial radial distributions. Most of the tested configurations result in similar radial distribution functions and are in quite good agreement with those found

Table 2 Average coordination numbers (CN) found with RMC and MD

Data set	CN La	CN Nd	CN Ce
$La_2Ce_2O_7$			
RMC1	7.12		7.02
RMC2	6.83		7.32
RMC3	7.09		7.04
MD	6.92		6.89
$La_{1.5}Nd_{0.5}Ce_2O_7$			
RMC1	7.02	7.02	7.02
RMC3	6.99	6.98	7.05
$LaNdCe_2O_7$			
RMC1	6.97	7.06	7.13
RMC3	6.83	6.93	7.31
$La_{0.5}Nd_{1.5}Ce_2O_7$			
RMC1	6.99	6.98	7.08
RMC3	6.90	6.93	7.16
$Nd_2Ce_2O_7$			
RMC1		7.07	7.05
RMC2		6.77	7.34
RMC3		6.98	7.18
MD		6.97	6.91

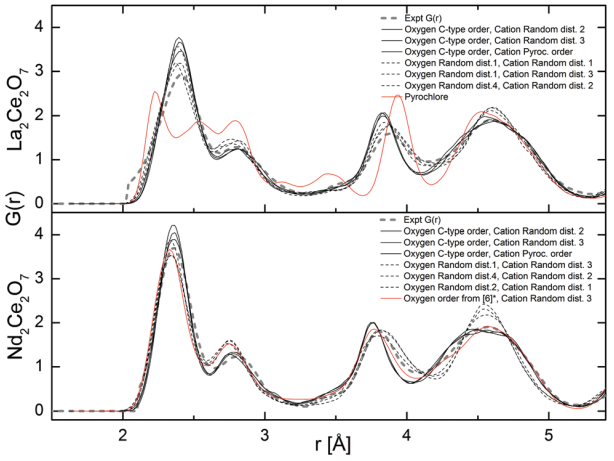

Fig. 9 Total neutron weighted $G(r)$ resulting from the MD runs at 300 K compared with the experimental results. * In ref. 6 a tetragonal structure is proposed with a ⟨210⟩ vacancy ordering and the symmetry has been translated into a cubic symmetry for a more direct comparison.

experimentally as can be seen in Fig. 9, where some of the neutron weighted total radial distribution functions $G(r)$ from MD runs at 300 K are plotted. A clear exception is the perfect pyrochlore configuration for $La_2Ce_2O_7$, which deviates considerably from the disordered oxygen deficient fluorite and oxygen excess C-type, supporting that such long range order is unlikely in any of the $La_{2-x}Nd_xCe_2O_7$ compositions, and will not be considered any further.

The broadening of the $G(r)$ peaks for $La_2Ce_2O_7$ compared to $Nd_2Ce_2O_7$ as found experimentally is also reproduced in the $G(r)$ from MD. Regardless of the choice of starting cation and anion configuration for both $La_2Ce_2O_7$ and $Nd_2Ce_2O_7$ the $G(r)$s are strikingly similar. There are, nevertheless, some small deviations between the configurations containing a randomly distributed oxygen sub-lattice, as indicated by RMC, compared to ordered oxygen configurations termed C-type ordering (see description in Section 2.3) which is an ordered oxygen excess C-type configuration.

In Fig. 9 we see that some of the peaks are either broadened or sharpened when comparing the ordered and random oxygen configurations, especially in the Nd_2Ce_2O system. The peak around 3.8 Å is broader and somewhat shifted to higher distance by around 0.1 Å for the disordered oxygen configurations, and the peak at ∼4.5 Å, which is dominated by cation–oxygen distances, is sharper when comparing with the ordered excess C-type configurations. Overall, the C-type related ordered oxygen configurations are more consistent with the experimental results for $Nd_2Ce_2O_7$ except around $r \sim 3.8$ Å, than the random oxygen configurations. The oxygen configuration containing a second type of ordering (proposed by Withers *et al.* in ref. 6) is also plotted for the $Nd_2Ce_2O_7$ system and resemble the random oxygen configurations at the shortest distances ($r < 3.5$) whereas they are closer to the C-type ordered configurations at longer distances ($r > 3.5$ Å). Although the same features and deviations are seen for the $La_2Ce_2O_7$ system, there is overall less deviation between ordered and random oxygen structures.

The partial distribution functions extracted from MD are in good agreement with those extracted from RMC with only some small deviations in the $g_{O-O}(r)$. The $g_{O-O}(r)$, from MD are plotted in Fig. 10 and show three well defined peaks corresponding to the ⟨100⟩, ⟨110⟩, and ⟨111⟩ alignments between the oxygen around the cations at approx. 2.8, 3.8, and 4.8 Å, respectively. The MD results appear more ordered than the $g_{O-O}(r)$ from RMC (Fig. 8), since the latter flattens out at higher r, especially in $La_2Ce_2O_7$. The shoulder at ∼2.5 Å found with RMC, is not seen in the MD results. The discrepancy can be explained by the modest cell size used in MD or uncertainties in the RMC result at short distances. Therefore, we also plot the results for a $3 \times 3 \times 3$ supercell in Fig. 10, where the atoms are distributed randomly to see how the cell size might influence the $g_{O-O}(r)$ and hopefully understand the deviation between RMC and MD. The disordered $3 \times 3 \times 3$ supercell reproduces the $g_{O-O}(r)$ from the $2 \times 2 \times 2$ supercell, suggesting that the RMC analysis is hampered by the presence of some artificial feature at the short O–O distances around 2.5 Å.

As for the total pair distribution functions from MD, there are also deviations between the ordered and the randomly distributed oxygen lattices, and the deviations are more visible for $Nd_2Ce_2O_7$. Although the random oxygen configurations are in better agreement with the RMC results around 4.8 Å (Fig. 10), the second peak at ∼3.8 Å corresponding to ⟨110⟩ alignment between oxygen, is clearly shifted to a higher r of about 0.2 Å when comparing with RMC, especially for $Nd_2Ce_2O_7$. The peak positions in the ordered oxygen configurations (*i.e.* denoted as C-type order in Fig. 9 and 10) in $Nd_2Ce_2O_7$ have an overall better agreement with the RMC results. Note that this ordered oxygen configuration derives from the oxygen excess C-type structure, where the vacant oxygen positions are ordered relative to each other in a similar manner as the 16c sites are in C-type structure. The ordered C-type related oxygen configurations is

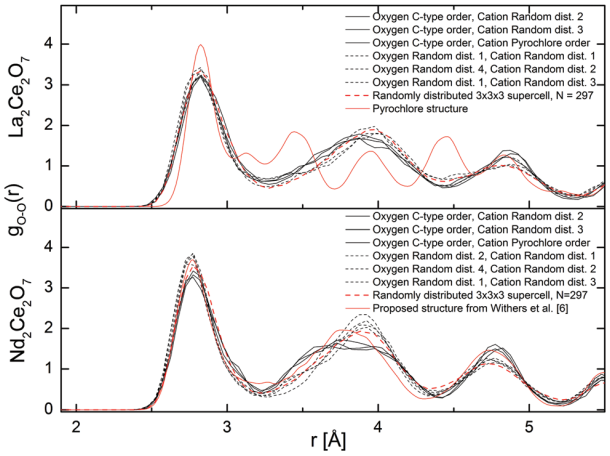

Fig. 10 Partial oxygen–oxygen $g_{O-O}(r)$ resulting from the MD runs at 300 K.

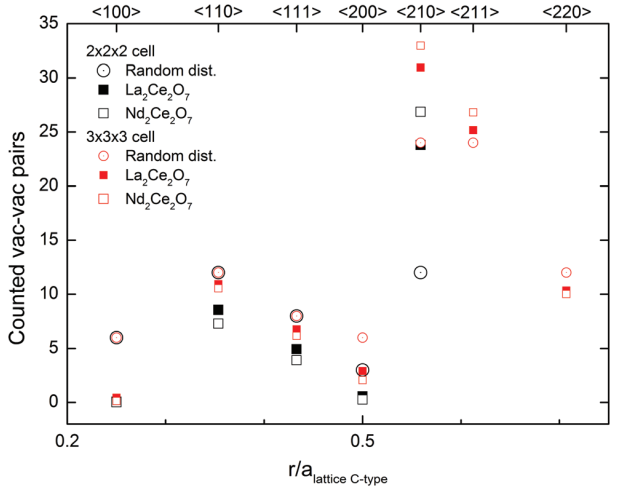

Fig. 11 The average occurrence of vac–vac pairs in $La_2Ce_2O_7$ (closed squares) and $Nd_2Ce_2O_7$ (open squares) from MD modelling using 2 × 2 × 2 cells (black) and 3 × 3 × 3 cells (red) at 1500 K, compared to the statistical distribution in a disordered system.

thus linked to the Rietveld results where the superlattice Bragg peaks were sensitive to the occupation of 16c. Since the vacancies are important to define the oxygen order we look further at vacancy ordering and alignments of vac–vac pairs in the systems.

3.3 Oxygen vacancy ordering

Oxide ion diffusion occurs during the MD runs at 1500 K, and therefore we can study how the oxygen sub-lattice evolves following diffusion. By sampling configurations from the run we then include numerous different oxygen configurations, further enabling us to look at statistics of the coordination numbers and the nature of oxygen vacancy order.

The coordination numbers from MD are around 7 for all cations (Table 2), supporting that vacancy–vacancy ordering is not driven by electrostatic forces between cations and oxygen. From the Rietveld refinement of the Nd-containing samples we know that the observed superlattice peaks in PND and PXRD can be associated with a C-type structure, and the stoichiometric C-type structure (*i.e.* R_2O_3) contains a specific ratio of vacancies oriented in the ⟨110⟩, ⟨111⟩ and ⟨210⟩ directions. So to understand the underlying nature of these Bragg-peaks found in $Nd_2Ce_2O_7$, the average vacancy–vacancy pair alignments found during the evolving MD runs in $Nd_2Ce_2O_7$ and $La_2Ce_2O_7$ are calculated.

The graph in Fig. 11 presents a pair distribution function with discrete values for the distances between the vacancies and shows the average number of vacancy pairs found in each set of directions within the supercell (N = 88 and 8 vacancies) of $Nd_2Ce_2O_7$ and $La_2Ce_2O_7$. For both compositions the closest vac–vac pairs are mostly observed in the ⟨110⟩ direction, as well as some in the ⟨111⟩ direction, which are the building blocks of the vacancy oxygen order found in the C-type structure.§ Almost no ⟨100⟩ pairs are found, and such alignments seem highly unfavourable. Furthermore, we found an unusually high amount of ⟨210⟩ alignments between the vacancies compared to a random vacancy distribution and almost no vac–vac pairs are aligned in the ⟨200⟩ direction. Since the 2 × 2 × 2 cell might be too small to correctly sample ⟨200⟩ and ⟨210⟩ pairs, additional MD runs were performed in a larger 3 × 3 × 3 cell, and the results confirm the high number of vac–vac pairs in the ⟨210⟩ direction (see Fig. 11).

In sufficiently reduced ceria an oxygen vacancy ordering with ⟨111⟩ vac–vac pairs is found.[14] Our results show that such ordering can be ruled out for both of the investigated systems. In the structure proposed by Withers *et al.*,[6] the preferred vac–vac alignment is also ⟨210⟩ together with some ⟨200⟩ and ⟨220⟩ alignments, based on the observed TEM diffraction pattern. However, they also suggest that first, second or third nearest neighbours should be avoided, which is not in agreement with our present MD simulations, since we see a significant amount of both ⟨110⟩ and ⟨111⟩ alignments. If we instead compare these results with the ratio between the typical alignments in C-type oxygen structures we see similarities. The ratios between the ⟨210⟩, ⟨110⟩ and ⟨111⟩ alignments observed in the MD runs for $Nd_2Ce_2O_7$ are between the ratios in the stoichiometric C-type and our oxygen excess C-type used as one of the starting configurations in MD at 300 K. The preferred vacancy alignments and ratio supports an oxygen vacancy ordering similar to that in C-type.

There is no doubt that the ⟨210⟩ directions between vacancies are important in these compositions, and this alignment between vacant 16c positions in the C-type structure is accommodated in the {321} plane, and is thus linked to the Rietveld results where this superlattice Bragg peak was sensitive to the occupation of 16c. The preference for ⟨210⟩ vacancy pairs is stronger for $Nd_2Ce_2O_7$ compared to $La_2Ce_2O_7$. This indicates that the tendency of intermediate range vacancy ordering is

§ There are indications towards the ⟨111⟩ vac–vac pairs being predominantly in empty cubes. However, a mix of empty and filled cubes is expected due to the resemblance to C-type structure and further studies are needed in order to determine the exact ratio.

stronger in $Nd_2Ce_2O_7$, although $La_2Ce_2O_7$ probably exhibits similar ordering to a small extent.

3.4 Summarizing discussion

The Rietveld refinements of the $La_{2-x}Nd_xCe_2O_7$ series show that $La_2Ce_2O_7$ exhibits a disordered oxygen deficient fluorite structure whereas additional super lattice peaks are apparent for the Nd-containing compositions. Therefore the best refinements for the Nd-containing compositions were reached with a two phase approach combining a C-type related structure with an oxygen deficient fluorite structure. Moreover, the Rietveld analysis revealed that the oxygen vacancies tend to be localised on the 16c site of the C-type structure, indicating that it can be viewed as an oxygen excess C-type phase. The increased intensity of the super-lattice peaks extracted from the PND data compared to the PXRD data indicates that oxygen order is the origin of the observed C-type supercell peaks. We find no evidence of cation order but the refinements show a small shift in one of the cation sites away from the perfect fluorite structure for the C-type related phase. The MD and RMC results are in good agreement and support the lack of cation clustering. Both techniques give an average coordination number around 7 for all cations in contrast to earlier suggested models.[2,3] Therefore, we trust that the observed supercell peaks appear mainly due to symmetry changes arising from oxygen vacancy ordering.

The observed vacancy ordering is described by vacancies aligning in the ⟨210⟩ direction combined with ⟨110⟩ and some ⟨111⟩ alignments, and can thus be termed an oxygen excess C-type structure where the remaining vacancies favour the 16c position. Such an order gives rise to symmetry planes equal to those in the C-type structure and can explain the superlattice peaks. Locally the ⟨110⟩ and ⟨111⟩ alignments of the vacancies induce small shifts in the cation position away from the perfect fluorite site for the 24d site as it is in the C-type structure. This shift in position will contribute to the additional superlattice peaks as supported by the Rietveld refinements.

The significant diffuse scattering observed for $La_2Ce_2O_7$ indicates that the local structure deviates from the average fluorite structure, and the background modulation is also consistent with the C-type peak positions suggesting that there is some short range order similar to that of the Nd-containing samples. MD modelling of $La_2Ce_2O_7$ supports this claim showing a tendency towards vacancy ordering.

Based on the diffraction data it is apparent that the amount, or degree, of long range order existing in $La_{2-x}Nd_xCe_2O_7$ increases with the Nd-content. In $La_{2-x}Nd_xCe_2O_7$ the lattice parameter decreases with Nd-content (see Fig. 6b), as expected, since the cation radius of Nd^{+3} is smaller than La^{+3}. The development is, however, not linear, and the additional size reduction is likely to occur due to the increase in long range order, which is in agreement with earlier studies on $Ce_{1-x}Nd_xO_{2-\delta}$.[9,16]

Some short range oxygen vacancy order seems to be preferred in both $La_2Ce_2O_7$ and $Nd_2Ce_2O_7$, but for long range order to appear, the building blocks of ⟨110⟩ and ⟨111⟩ alignments between the vacancies, further creating a high number of ⟨210⟩ alignments, must expand over several unit cells. The driving force towards long range order in $La_{2-x}Nd_xCe_2O_7$ is most likely due to structural relaxation based on vacancy interactions and changes in cation size, since the coordination numbers and vacancy concentrations are equal for all the compositions in the $La_{2-x}Nd_xCe_2O_7$ series. The decreasing cell size and free volume with increasing Nd-content could impose greater electrostatic forces between the vacancies, and oxide ions, making it more favourable for them to order. Structural relaxation in terms of long range ordering could also be facilitated by more similar ionic radius for the involved cations (*i.e.* Nd^{+3} more similar to Ce^{+4} than La^{+3}). In $La_2Ce_2O_7$, on the other hand, the strain caused by larger differences in cation size within the disordered cation lattice, obstructs the prevalence of long range order. This is consistent with the findings of Yamamura *et al.* in an earlier study of $Ln_2Ce_2O_7$ (Ln = La, Nd, Sm, Eu, Gd, Y, Yb).[17] They concluded that the ionic radius ratio $r(Ln^{3+})/r(Ce^{4+})$, using the 8-fold coordinated Shannon radii,[40] must be smaller than 1.17 for the C-type phase to be stabilized. This leaves $La_2Ce_2O_7$ outside the stability range. This correlation is also found in the work of Ou *et al.* in similar compositions.[41]

The two phase approach used in the Rietveld refinements does not contradict the existence of grains containing domains of vacancy ordering, and the refined unit cell parameters of the two phases are indeed almost identical (*i.e.* $a_{\text{fluorite}} \approx 1/2 \times a_{\text{c-type}}$). Also the $G(r)$s extracted from ordered and random oxygen configurations are quite similar, indicating that they could co-exist without considerable lattice mismatch. We therefore conclude that the samples of $La_{2-x}Nd_xCe_2O_7$ exhibit crystalline grains with the fluorite structure and the presence of anion ordered domains of increasing extent with the Nd-content and it is supported by findings in $Y_2Ce_2O_7$ by Withers *et al.*[6]

Vacancy ordering ultimately lowers the oxide ion conductivity. When a long range ordered sub-lattice is energetically favourable, the activation energy for an oxygen jump is higher than in a totally disordered lattice, as it can be compared to the formation of an anti-Frenkel defect. Oxygen transport might even depend on collective movements. If the more local forces are the dominating factor for the ordering, the oxygen (or vacancy) can be effectively trapped. In these compositions it is natural to assume that any oxygen movement inducing a vac–vac alignment in the ⟨100⟩ would have a high activation barrier, leading to a lower number of possible sites the oxygen (or vacancy) can jump to.

4 Conclusions

The $La_{2-x}Nd_xCe_2O_7$ series predominantly exhibits a disordered fluorite structure with increasing intensity of additional C-type supercell peaks in the PND data with increasing x. Rietveld refinements show that the Nd-containing ($x > 0$) compositions were best fitted using a combination of oxygen deficient fluorite and oxygen excess C-type structure, whereas $La_2Ce_2O_7$ was best refined as a disordered fluorite. The diffraction data and Rietveld refinements indicate that superlattice peaks stem from domains with vacancy ordering and associated shifts in the cation position away from the perfect fluorite structure, which is related to the C-type structure. *Ab initio* molecular dynamics

results confirm that oxygen vacancy order comparable to that in the C-type structure, is a plausible ordering scheme explaining the change in long range order and the observed C-type Bragg peaks. The oxygen vacancies prefer alignments in the ⟨210⟩ direction in combination with the ⟨110⟩ and ⟨111⟩ direction. The PND data and MD suggest that C-type related ordering might also be found in $La_2Ce_2O_7$. The radial distribution functions extracted from PND, RMC and MD is in good agreement, and show that oxygen ordered and disordered configurations can co-exist. The results show how these compositions are at the border between different structures where the stability is so finely balanced between enthalpic and entropic contributions, order and disorder. The extent of long range order gradually increases as the average cation size decreases with Nd-substitution. Finally, greater vacancy ordering can explain the low oxide ion conductivity in $Nd_2Ce_2O_7$ compared to $La_2Ce_2O_7$.

Acknowledgements

The authors gratefully acknowledge UNINETT Sigma2 – the National Infrastructure for High Performance Computing and Data Storage in Norway, for providing computational resources for the MD modelling. The UK Science and Technology Facilities Council is thanked for allocating neutron beamtime at the ISIS facility, Rutherford Appleton Laboratory, U.K.

References

1 J. P. Allen, P. R. Keating, D. O. Scanlon and G. W. Watson, *Doping CeO_2 with trivalent cations: defect structures and reducibility,* American Chemical Society, 2013, p. ENFL-418.
2 M. Coduri, M. Brunelli, M. Scavini, M. Allieta, P. Masala, L. Capogna, H. E. Fischer and C. Ferrero, *Z. Kristallogr.*, 2012, **227**, 272–279.
3 D. E. P. Vanpoucke, P. Bultinck, S. Cottenier, V. Van Speybroeck and I. Van Driessche, *J. Mater. Chem. A*, 2014, **2**, 13723–13737.
4 L. Pino, A. Vita, M. Lagana and V. Recupero, *Appl. Catal., B*, 2014, **148–149**, 91–105.
5 H. L. Tuller and A. S. Nowick, *J. Electrochem. Soc.*, 1975, **122**, 255–259.
6 R. L. Withers, J. G. Thompson, N. Gabbitas, L. R. Wallenberg and T. R. Welberry, *J. Solid State Chem.*, 1995, **120**, 290–298.
7 T. Kudo and H. Obayashi, *J. Electrochem. Soc.*, 1975, **122**, 142–147.
8 H. Yahiro, Y. Eguchi, K. Eguchi and H. Arai, *J. Appl. Electrochem.*, 1988, **18**, 527–531.
9 T. Hagiwara, Z. Kyo, A. Manabe, H. Yamamura and K. Nomura, *J. Ceram. Soc. Jpn.*, 2009, **117**, 1306–1310.
10 J. Faber, C. Geoffroy, A. Roux, A. Sylvestre and P. Abélard, *Appl. Phys. A: Solids Surf.*, 1989, **49**, 225–232.
11 H. L. Tuller and A. S. Norwick, *J. Electrochem. Soc.*, 1979, **126**, 209–217.
12 H. J. Rossell and H. G. Scott, *J. Phys. (Paris), Colloq.*, 1977, **38**(Colloq C-7), 28–31.
13 T. R. Welberry, B. D. Butler, J. G. Thompson and R. L. Withers, *J. Solid State Chem.*, 1993, **106**, 461–475.
14 S. Hull, S. T. Norberg, I. Ahmed, S. G. Eriksson, D. Marrocchelli and P. A. Madden, *J. Solid State Chem.*, 2009, **182**, 2815–2821.
15 M. Mogensen, T. Lindegaard, U. R. Hansen and G. Mogensen, *J. Electrochem. Soc.*, 1994, **141**, 2122–2128.
16 L. Li, R. Kasse, S. Phadke, W. Qiu, A. Huq and J. C. Nino, *Solid State Ionics*, 2012, **221**, 15–21.
17 H. Yamamura, H. Nishino, K. Kakinuma and K. Nomura, *J. Ceram. Soc. Jpn.*, 2003, **111**, 902–906.
18 H. Yamamura, H. Nishino and K. Kakinuma, *J. Ceram. Soc. Jpn.*, 2004, **112**, 553–558.
19 V. Besikiotis, C. S. Knee, I. Ahmed, R. Haugsrud and T. Norby, *Solid State Ionics*, 2012, **228**, 1–7.
20 E. Reynolds, P. E. R. Blanchard, Q. Zhou, B. J. Kennedy, Z. Zhang and L.-Y. Jang, *Phys. Rev. B: Condens. Matter Mater. Phys.*, 2012, **85**, 132101.
21 D. E. P. Vanpoucke, P. Bultinck, S. Cottenier, V. Van Speybroeck and I. Van Driessche, *Phys. Rev. B: Condens. Matter Mater. Phys.*, 2011, **84**, 054110.
22 S. Cheng, Master thesis, University of Oslo, 2012.
23 H. Rietveld, *J. Appl. Crystallogr.*, 1969, **2**, 65–71.
24 A. C. Larson and R. B. Von Dreele, General Structure Analysis System (GSAS), *Los Alamos National Laboratory Report*, 1994, LAUR 86-748.
25 A. K. Soper, Gudrun, http://www.isis.stfc.ac.uk/instruments/sandals/data-analysis/gudrun8864.html.
26 D. Keen, *J. Appl. Crystallogr.*, 2001, **34**, 172–177.
27 M. G. Tucker, D. A. Keen, M. T. Dove, A. L. Goodwin and Q. Hui, *J. Phys.: Condens. Matter*, 2007, **19**, 335218.
28 S. T. Norberg, M. G. Tucker and S. Hull, *J. Appl. Crystallogr.*, 2009, **42**, 179–184.
29 N. E. Brese and M. O'Keeffe, *Acta Crystallogr., Sect. B: Struct. Sci.*, 1991, **47**, 192–197.
30 S. Nosé, *J. Chem. Phys.*, 1984, **81**, 511–519.
31 G. Kresse and J. Hafner, *Phys. Rev. B: Condens. Matter Mater. Phys.*, 1993, **48**, 13115–13118.
32 A. Spek, *Acta Crystallogr., Sect. D: Biol. Crystallogr.*, 2009, **65**, 148–155.
33 P. E. Blochl, C. J. Forst and J. Schimpl, *Bull. Mater. Sci.*, 2003, **26**, 33–41.
34 G. Kresse and J. Furthmueller, *Phys. Rev. B: Condens. Matter Mater. Phys.*, 1996, **54**, 11169–11186.
35 J. P. Perdew, K. Burke and M. Ernzerhof, *Phys. Rev. Lett.*, 1996, **77**, 3865–3868.
36 V. Grover and A. K. Tyagi, *J. Solid State Chem.*, 2004, **177**, 4197–4204.
37 F. Brisse and O. Knop, *Can. J. Chem.*, 1967, **45**, 609–614.
38 J. E. H. Sansom, J. R. Tolchard, P. R. Slater and M. S. Islam, *Solid State Ionics*, 2004, **167**, 17–22.
39 W. L. Bragg and E. J. Williams, *Proc. R. Soc. London, Ser. A*, 1934, **145**, 699–730.
40 R. Shannon, *Acta Crystallogr., Sect. A: Cryst. Phys., Diffr., Theor. Gen. Crystallogr.*, 1976, **32**, 751–767.
41 D. R. Ou, T. Mori, F. Ye, T. Kobayashi, J. Zou, G. Auchterlonie and J. Drennan, *Appl. Phys. Lett.*, 2006, **89**, 171911.
42 K. Momma and F. Izumi, *J. Appl. Crystallogr.*, 2011, **44**, 1272–1276.

Paper II

First principles calculations on order and disorder in $La_2Ce_2O_7$ and $Nd_2Ce_2O_7$

L-E. Kalland and C. E. Mohn, Physical Chemistry Chemical Physics, 2020, 22, 13930-13941

DOI: 10.1039/d0cp00921k

PCCP

PAPER

Cite this: *Phys. Chem. Chem. Phys.*, 2020, **22**, 13930

First principles calculations on order and disorder in $La_2Ce_2O_7$ and $Nd_2Ce_2O_7$†

Liv-Elisif Kalland [a] and Chris E. Mohn[b]

Received 18th February 2020,
Accepted 7th May 2020

DOI: 10.1039/d0cp00921k

rsc.li/pccp

In this paper, we highlight the connection between the local structure and collective dynamics of the defective fluorites $La_2Ce_2O_7$ and $Nd_2Ce_2O_7$. The local and average structure is explored by investigating a large number of different structural models and snapshots from Born–Oppenheimer Molecular dynamics calculations. Both compounds show a strong preference for local oxygen vacancy order similar to that found in the C-type structure. This suggests that previous studies, where $Nd_2Ce_2O_7$ and $La_2Ce_2O_7$ are viewed as disordered defective fluorites, or as a pyrochlore for the latter, did not capture the nature of local order in the disordered phase. We observe more collective chains of migrating oxygen in $Nd_2Ce_2O_7$ – a manifestation of a stronger preference for a dynamic local oxygen vacancy order – than in $La_2Ce_2O_7$. The stronger preference for ⟨210⟩ vacancy–vacancy alignments can explain why long range ordering is identified by distinct C-type like superlattice peaks in neutron diffraction patterns for $Nd_2Ce_2O_7$ whereas they appear to be almost invisible in $La_2Ce_2O_7$.

1. Introduction

The local structure of a disordered oxide is of key importance in order to understand many of its chemical and physical properties, such as ionic conductivity and hydration. Popular structural models, however, often assume that the structure of a crystalline disordered material can be represented by an ''average'' model where the disordered ions are distributed randomly over a sublattice. Although such models are useful as a starting point for many properties, they do not capture changes in the environment a diffusing ion will experience as it jumps from one position to another one. Such changes in the local structure are therefore essential to understanding diffusion processes in disordered oxides.[1,2] Many $A_2B_2O_7$ compounds, where A is a trivalent lanthanide and B is a tetravalent cation, are conveniently classified as fully ordered perfect pyrochlore structures or as oxygen deficient disordered flourites (see Fig. 1(c) and (a), respectively). Minervini *et al.*[3] suggested that a tolerance factor, $R = r_A/r_B$ (r_A is the ionic radius for an 8-fold coordinated trivalent A cation and r_B is the ionic radius for a 6-fold coordinated tetravalent B cation), can be used to predict whether an $A_2B_2O_7$ compound should be classified as a perfect pyrochlore structure ($R > 1.4$) or if it will be disordered (and hence be classified as a disordered fluorite). $La_2Ce_2O_7$, for example, has attracted considerable interest since it displays both high oxygen ion and proton conductivity,[4,5] but its crystal structure is poorly understood. Since the tolerance factor for $La_2Ce_2O_7$ is 1.33, which is slightly less than 1.4, one would expect that it displays a disordered (oxygen deficient) fluorite structure. Although Vanpoucke *et al.*[6] suggested that $La_2Ce_2O_7$ exhibits an ordered pyrochlore structure,[6] most works support this prediction[4,7–9] and the relatively high oxygen conductivity of ''undoped'' $La_2Ce_2O_7$ also suggests that it has a highly disordered oxygen structure.

Oxygen disordered oxides often display high oxygen ion conductivity, and it is therefore interesting to see how their structure changes when incorporating a smaller lanthanide cation and how in turn these structural changes affect ionic conductivity. The tolerance factor decreases to about 1.22 when La^{3+} is replaced with Nd^{3+} and this suggests that $Nd_2Ce_2O_7$ is a disordered fluorite as well (all $Ln_2Ce_2O_7$ compounds are actually predicted to be disordered fluorites). However, this prediction contradicts several X-ray studies where the presence of weak superlattice peaks indicates structural deviation from the fluorite structure.[7] Neutron diffraction studies confirmed this and observed distinct Bragg peaks for $Nd_2Ce_2O_7$, which indicates long range crystalline order.[10,11] The peak positions are consistent with the C-type structure (see Fig. 1d) which could possibly be explained by the presence of strong but partial oxygen vacancy interactions as suggested for heavily yttria doped ceria.[12,13] Long range oxygen order is thus observed once La^{3+} is substituted by Nd^{3+} in $La_{2-x}Nd_xCe_2O_7$, but interestingly, notable modulations of the background scattering between the fluorite peaks of $La_2Ce_2O_7$ are found in the same region as the superlattice Bragg peaks were found for

[a] *Department of Chemistry, Centre for Materials Science and Nanotechnology, University of Oslo, FERMiO, Gaustadalléen 21, Norway. E-mail: l.e.kalland@kjemi.uio.no*
[b] *Centre for Earth Evolution and Dynamics, Department of Geosciences, University of Oslo, Norway*

† Electronic supplementary information (ESI) available. See DOI: 10.1039/d0cp00921k

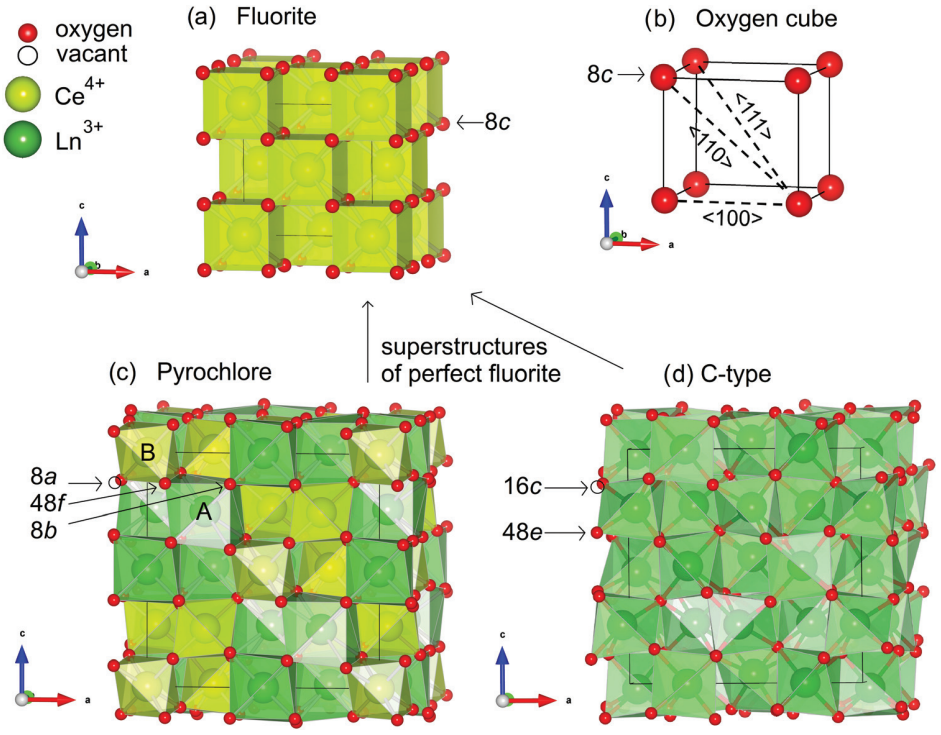

Fig. 1 Polyhedral representations of: (a) the fluorite structure for CeO_2, (Z = 2, space group $Fm\bar{3}m$) where Ce^{4+} is 8 fold coordinated, (b) the primitive oxygen cube where the oxygen sits at the 8c site in the fluorite structure, (c) the pyrochlore structure ($A_2B_2O_7$/$Ln_2Ce_2O_7$, Z = 8, space group $Fd\bar{3}m$) where Ce^{4+} is 6-fold and Ln^{3+} is 8-fold coordinated and (d) the C-type fluorite (Ln_2O_3, Z = 16, space group $Ia\bar{3}$) where Ln is 6-fold coordinated. The cubic C-type structure and the pyrochlore structure are both oxygen deficient ordered superstructures of the perfect cubic fluorite and structurally very similar. The "cube" in (b) is used to define the alignments of vacancy–vacancy pairs as ⟨100⟩, ⟨110⟩ and ⟨111⟩. Note that since the "oxygen cubes" alternate between having a cation in the centre and not, the ⟨111⟩ vac–vac pairs may be aligned with a cation in the centre or not.

$Nd_2Ce_2O_7$.[10] This suggests that $La_2Ce_2O_7$ may also have some local order that resembles the order found in the C-type structures.

In this work, we shall investigate the local structure and ionic conductivity of $La_2Ce_2O_7$ and $Nd_2Ce_2O_7$ using density functional theory (DFT). We will attempt to provide a local structural view on the nature of vacancy ordering in $La_2Ce_2O_7$ and $Nd_2Ce_2O_7$ and briefly discuss how these local motifs affect the conductivity of $La_2Ce_2O_7$ and $Nd_2Ce_2O_7$.

To investigate the structural properties of these two compounds, a large number of different configurations of cations and oxygen are analysed representing possible ordered phases or structural "snapshots" of the disordered phase. We investigate both the "static" structure found by searching for the lowest energy minimum of a given configuration of cations and oxygen ions, and the dynamic structure that are "snapshots" taken directly from the molecular dynamic (MD) trajectories. The static structure we investigate includes well known structural models (see the next section for a description) as well as quenched configurations from high temperature MD runs to search for new (low energy) structures.

2. Computational methods and details

The DFT calculations in this work were performed using the generalized gradient approximation (GGA) represented by the Perdew–Burke–Ernzerhof (PBE) functional[14] together with a projector augmented wave (PAW)[15] as implemented in the VASP code.[16] In all calculations, we have used a 3 × 3 × 3 Monkhorst–Pack for the integration in the Brillouin zone and an energy cut-off of 500 eV for the structural optimisations. In the MD simulations, we used the gamma point only, an energy cut-off of 400 eV and a step length of 2 fs.

We present results obtained from structural optimisations performed using a 88 atoms supercell (*i.e.* a 2 × 2 × 2 cubic supercell) constructed from fluorite unit cells. This supercell has the same size as a single unit cell of the pyrochlore and the C-type structure. The MD runs are carried out in a 3 × 3 × 3 (297 atoms) supercell in the *NVT* ensemble. To obtain sufficient statistics to calculate the diffusion coefficient from the mean square displacement (MSD), the MD simulations ran for 45.8 ps for the $La_2Ce_2O_7$ system and for 76.2 ps for $Nd_2Ce_2O_7$.

The nature of oxygen and vacancy configurations are explored by identifying vacant tetrahedral cavities centred at the 8c site of the cubic fluorite structure and by calculating the distance and direction between pairs of vacancies. The notation ⟨100⟩, ⟨110⟩, ⟨111⟩, ⟨200⟩, ⟨210⟩, ⟨211⟩ and ⟨220⟩ is used to label the crystallographic different vac–vac alignments, as illustrated in Fig. 1(b).

The configurations (before optimisation) are grouped together by structural similarities in the oxygen and cation sublattices. A "random" oxygen sublattice is labelled "Orand*X*", where X = 1–4

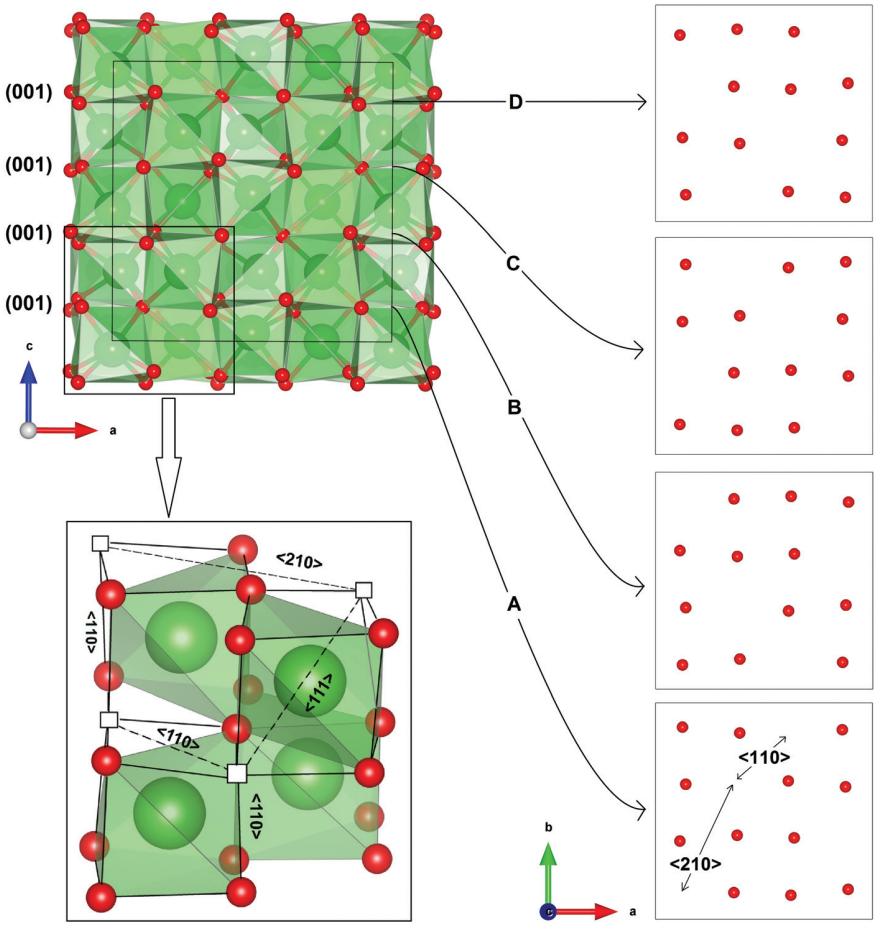

Fig. 2 Different crystallographic *ab* planes (or (001) planes) in the C-type structure (space group $Ia\bar{3}$). The different vac–vac pair alignments found in the C-type, *i.e.* the ⟨110⟩, ⟨111⟩ and ⟨210⟩ motifs, are shown at the bottom left.

c-direction	Original C-type	"Ctype1"	"Ctype2"	"Ctype3"	"Ctype4"
	D	Full	Full	Full	Full
	C	C	B	Full	Full
	B	Full	Full	B	C
	A	A	A	A	A

Fig. 3 Different stacking sequences (along the *c*-axis) of the C-type related oxygen configurations "Ctype*X*" constructed by combining the *ab*/(100)-planes shown in Fig. 2.

represents different configurations. Similarly, "Ctype*X*" denotes different ordered oxygen sublattices that are crystallographically related to the C-type structure, as shown in Fig. 2 and 3. The "Vac111" configuration is also related to the C-type structure, but the plane contains only one vacancy per *ab* plane and thus has only ⟨111⟩ pairs (see Fig. 4(c)). The oxygen configuration, termed "Withers", is an ordered oxygen configuration suggested by Withers *et al.* for $Y_xCe_{1-x}O_{2-\delta}$ ($x = 0.5$)[13] (see Fig. 4(e)). In addition, the configuration denoted as "Vac200" is constructed by repeating the oxygen configuration of a single fluorite unit cell with one vacant 8c site in all crystallographic directions. This configuration will consequently contain only ⟨200⟩ alignments of vacancies. The cation sublattice has been labelled using a similar notation, where "Rand*X*" represents different random cation configurations with X = 1–4. "Fluorite" is an ordered configuration with equal cations in the crystallographic (100)-planes and the "Pyro" configuration has the cations ordered as in the pyrochlore structure.

We constrained the simulation cell to remain cubic during the geometry optimisation, which also makes structural analysis[17]

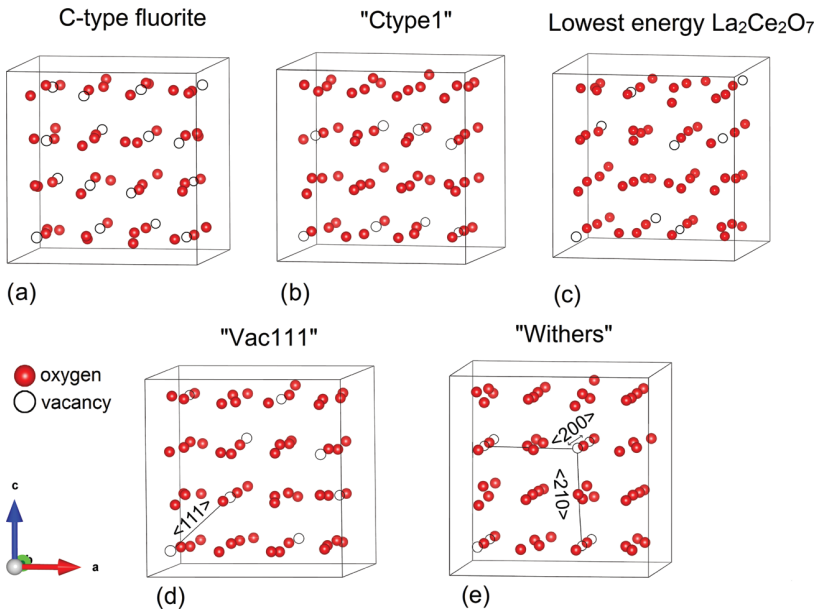

Fig. 4 Oxygen sublattice (shown after relaxation in our DFT calculations) of (a) the C-type structure where all 16c sites are vacant, (b) the C-type related structure termed "Ctype1", where half of the 16c sites are filled, (c) the most stable (*lowest energy*) configuration for $La_2Ce_2O_7$, which has a pyrochlore cation structure, (d) the "Vac111" with vac–vac pairs with a ⟨111⟩ alignment where half of the 16c sites are filled, and (e) the "Withers" – model.

and comparison between the different configurations, easier. Calculations show that the relative order of the different optimised configurations does not change when we compare with the results obtained by full structural optimisation allowing both the cell volume and the cell shape to relax.

The Hubbard type $+U$ correction is frequently used when investigating compounds containing 4*f* electrons since GGA and LDA may fail to describe the correlated nature of the f-electrons. DFT+U is essential if the goal is to study the electronic conductivity and charge transfer processes. However, in this work, our objective is to study the structural properties rather than the electronic properties, and it can be computationally challenging to use DFT+U if "+U" has to be (re)optimised for different compositions and configurations. Test calculations carried out by VanPoucke *et al.*[18] using a $+U$ correction term for cerium, did not change the relative stability of the investigated configurations for $La_2Ce_2O_7$. We have, nevertheless, performed DFT+U calculations on a few configurations for $Nd_2Ce_2O_7$ and $La_2Ce_2O_7$, to ensure that the relative energies between the different configurations calculated using GGA are qualitatively in agreement with those from GGA+U calculations. In these tests, we used U = 5 eV for Ce and U = 6.5 eV for Nd, which are the same values as in several previous studies (for Ce[18–20] and for Nd[21–23]). The energy difference between GGA and GGA+U is similar for all configurations. Some low energy configurations of $La_2Ce_2O_7$ became even lower in energy and closer to the lowest energy configuration, but the relative order between the energies of the configurations was in general not changed (see Tables 1 and 2 in the additional information). We therefore do not use a $+U$ correction term to DFT in our structural investigation for $La_2Ce_2O_7$ and $Nd_2Ce_2O_7$.

3. Results and discussion

Nature of vacancy order in $La_2Ce_2O_7$ and $Nd_2Ce_2O_7$

Comparison of the energy-minima of the different groups of oxygen configurations in Fig. 5 shows that the oxide ions prefer to order in both $La_2Ce_2O_7$ and $Nd_2Ce_2O_7$. Although we do not show all optimised configurations in Fig. 5, the oxygen-order is similar for both compounds arranged with increasing energy: E(Ctype1) < E(Vac111) < E(Withers) < E(Ctype2) < E(Ctype3, Ctype4) ≈ E(Orand$X$).

All random oxygen configurations, such as "Orand1", have a high energy of $> k_BT$ (even at T = 2000 K) and several of them relax to a different oxygen-configuration. The ordering in the oxygen sublattice is more pronounced than the ordering in the cation sublattice (as seen in Fig. 5), which is not surprising since exchanging a vacancy with an oxygen distorts the local structure to a greater extent compared to exchanging two (aliovalent) cations.

Many of the "unstable" high energy configurations shown in Fig. 5 have either cations with coordination numbers below 6 or contain several nearest neighbour ⟨100⟩ vacancy pairs. These are particularly unfavourable in agreement with what we reported earlier.[10] Configurations with a high fraction of ⟨210⟩ alignments, on the other hand, are found to be very favourable as there are many ⟨210⟩ vacancy pairs in all low energy configurations. More difficult to predict is the energy of configurations with many ⟨200⟩ or ⟨220⟩ vacancy pairs, because even though they appear to be "strained" and therefore often tend to relax to ⟨210⟩ pairs, we find that the ordered oxygen configuration called "Withers", which contains both ⟨200⟩ and ⟨220⟩ motifs, is surprisingly low in energy! However, the "Withers" configuration also contains many ⟨210⟩ vacancy pairs, which lowers its total energy, and so in general the ⟨200⟩ and ⟨220⟩ vacancy pairs appear to be energetically unfavourable.

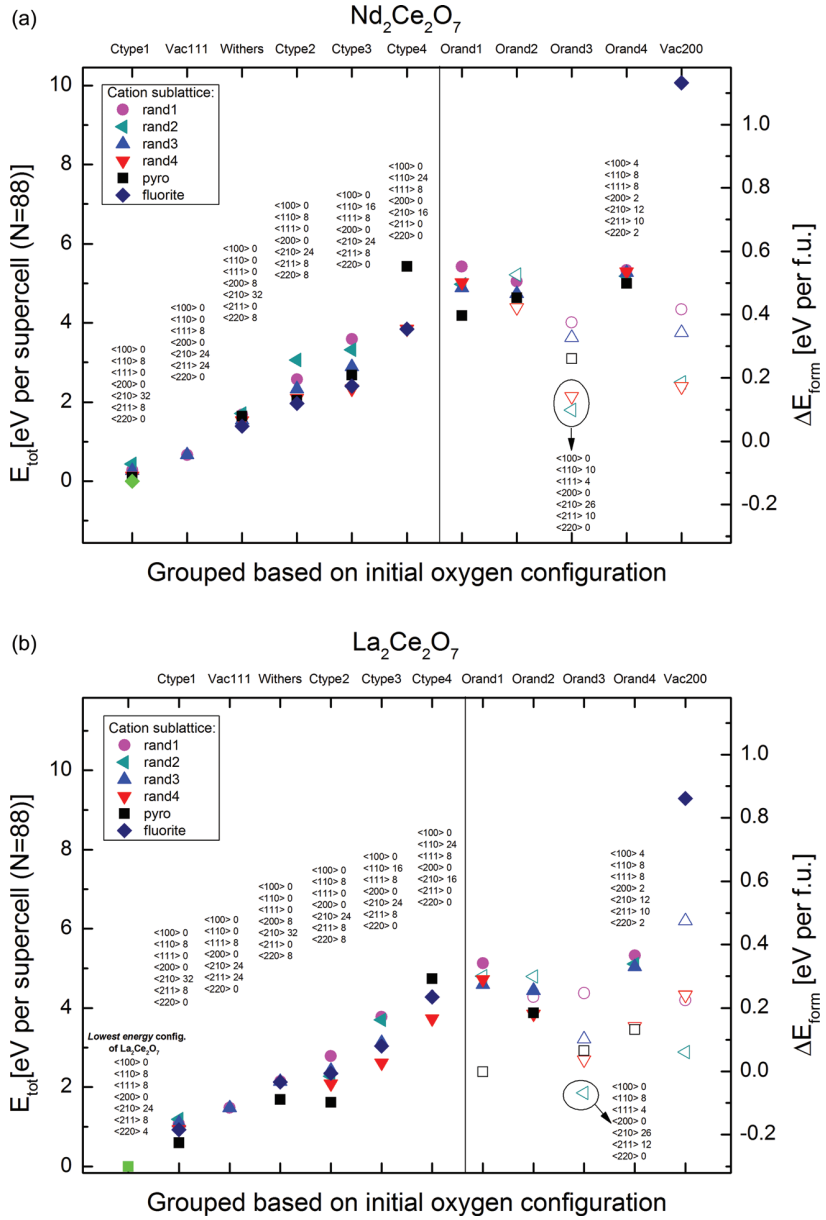

Fig. 5 Total energies relative to the lowest energy configuration, for different arrangements of oxygens and cations for (a) $Nd_2Ce_2O_7$ and (b) $La_2Ce_2O_7$ calculated using a supercell of 88 ions. The structure configurations are grouped based on the initial oxygen configuration (before structural optimisation). The 6 first groups (''Ctype1'', ''Vac111'', ''Withers'', and ''Ctype2-4'') are crystallographically ordered, and the next 4 groups (''Orand1-4'') represent ''disordered'' oxygen sublattices with *P*1 symmetry in the oxygen sublattice. The last group, ''Vac 200'', is initially ordered but relaxes to a disordered oxygen configuration in combination with almost all cation sublattices and is therefore grouped together with the disordered configurations. Configurations where the initial oxygen configuration relaxes to a new configuration during the structural optimisation are shown as open symbols whereas those that retain their ordered pattern during the structural optimisations are shown as filled symbols. The lowest energy configuration for each compound is highlighted by a bright green colour. The numbers of vacancy pairs in the 88 ion simulation cell are listed.

The two oxygen configurations with lowest energy (when omitting, for now, the *lowest energy* configuration of $La_2Ce_2O_7$), ''Ctype1'' and ''Vac111'', are similar in the sense that they both can be described as ordered oxygen excess C-type structures. We can visualize the crystallographic connection between these two oxygen structures and the C-type structure by filling up 8 of the 16 vacant oxygen positions in the C-type structure and aligning the 8 remaining vacant 16c site in an ordered manner (as shown in Fig. 4(b) and (d)). We can recognize the patterns of vacancies in the ''Ctype1'' and ''Vac111'' through a comparison with the C-type structure. ''Ctype1'', for example, contains ab-planes with vacancies aligned as they are in the C-type structure (see Fig. 4(b) and Fig. 2 for comparison). Both ''Ctype1'' and ''Vac111'' contain a large number of ⟨210⟩ vacancy pairs, but ''Ctype1'' has more ⟨210⟩ vac–vac pairs than ''Vac111'' and has the lowest energy of the two. The next two oxygen configurations

in Fig. 5, ''Withers'' and ''Ctype2'', contain both ⟨200⟩ and ⟨220⟩ vacancy motifs, which might be one of the main reasons why their energies are slightly higher than the ''Ctype1'' and ''Vac111'' configurations. The four most favourable ordered configurations presented (''Ctype1, ''Vac111'', ''Withers'' and ''Ctype2'') have the vacancies more homogenously distributed compared to ''Ctype3'' and ''Ctype4''. The latter two have all the vacancies clustered together to one side of the simulation box (see Fig. 2 and 3). This again results in fewer favourable ⟨210⟩ vac–vac alignments but in more ⟨110⟩ and ⟨111⟩ pairs giving a low coordination number of some cations that is not favourable (*i.e.* more than 8 ⟨110⟩ or ⟨111⟩ pairs in our 88 ion super cells).

It may seem surprising that the ''Vac111'' configuration is so low in energy since the pyrochlore structure, which contains only ⟨111⟩ motifs, is a highly unfavourable configuration, as we will discuss more in detail later. It is thus important to note that the ''Vac111'' configuration presented in the graphs only has ⟨111⟩ vacancy pairs aligned in ''oxygen cubes'' without a cation in the cube centre, which is opposite to the pyrochlore structure shown in Fig. 1(c). If the oxygen sublattice of the ''Vac111'' configuration is shifted, and the ⟨111⟩ pairs are aligned with cations in the cube centre positions (*i.e.* if we transform the entire anion lattice by 1/4 × ⟨100⟩), the energy of the configuration formed by such a translation is increased substantially by about 1 to 1.5 eV per supercell of $La_2Ce_2O_7$ and by about 1.5 to 2 eV for $Nd_2Ce_2O_7$. This energy increase is largely independent of the type of cation in the cube centre, but reflects that the electrostatic interaction between the cation and anion sublattices, in some cases, may strongly influence the total energy. When the ⟨111⟩ pairs are aligned through an oxygen cube with a cation in the cube centre, the remaining oxygens in the cube will relax forming an octahedron around the cation. However, this oxygen configuration will still be very strained since the octahedron is deformed and stretched to fit into an otherwise cubic oxygen sublattice. The energy of these configurations is therefore much higher compared to the ''Vac111'' configurations with ⟨111⟩ pairs that are aligned without cations in the cube centre positions.

To sum up, from a comparison of low and high energy groups of configurations, we identified a number of constraints on local oxygen/vacancy order for both $La_2Ce_2O_7$ and $Nd_2Ce_2O_7$: (1) a high fraction of ⟨210⟩ vacancy pairs is beneficial and is best achieved when vacancies are ordered in C-type related ''long range'' patterns, (2) ⟨100⟩ pairs should be avoided, and (3) ⟨111⟩ vac–vac alignments are only favourable when aligned in an oxygen cube without a cation in the cube centre. (4) The vacancies should also be evenly ''spread out'' in a way that is consistent with cation coordination numbers between 6 and 8. (5) C-type related ordering of vacancies is found to be energetically favorable independent of the cation arrangement.

Cation ordering

We find that there is one (ordered) cation arrangement that is clearly favoured over others for both $La_2Ce_2O_7$ and $Nd_2Ce_2O_7$. This may seem surprising since most structural analyses do not capture any cation ordering. For $Nd_2Ce_2O_7$, the lowest energy cation configuration is an ''ordered fluorite'' (shown as diamonds in Fig. 5), where the cations are evenly distributed in such a way that they all have the same local oxygen environment regardless of cation type. The lowest energy configurations for $La_2Ce_2O_7$ have the pyrochlore cation sublattice (squares in Fig. 5) (see Fig. 1(c) for a description of the pyrochlore structure). The reason why the cation sublattice with the lowest energy for $La_2Ce_2O_7$ and $Nd_2Ce_2O_7$ is different, is due to the difference in size mismatch between Nd/Ce and La/Ce: $La_2Ce_2O_7$ does not order in an ordered ''fluorite'' cation configuration because the large size mismatch between the cations would create a substantial strain along the {100}-planes in the direction where identical cations are aligned. The pyrochlore cation configuration is a better ''packing alternative'' for $La_2Ce_2O_7$ as well as for any $A_2B_2O_7$ compound with an even larger tolerance factor *R*. However, the tolerance factor *R* for $La_2Ce_2O_7$ is smaller than 1.4 and, as predicted by Minervini *et al.*,[3] we confirm that the pyrochlore structure is unfavourable since the oxygen sublattice is not pyrochlore ordered.

By comparing all configurations, we found an average coordination number close to 7 for all cations in the group of low energy configurations (see Fig. A in additional information where we plot the minimized energies *versus* coordination number of the cations). This supports that the ordering schemes found in the cation and oxygen sublattices are not directly linked through specific preferences in coordination numbers of the cations. In contrast, Liu *et al.*[24] found that differences in cation oxygen bond lengths indicate a lower coordination number for Gd than for Ce in $Gd_2Ce_2O_7$ (comparable to the $Nd_2Ce_2O_7$ compound) and for Ce than for La in $La_2Ce_2O_7$. From Fig. A in the additional information, there is a possible indication that Nd has a slightly lower average coordination number than Ce^{4+}, as can be seen by comparing a group of low energy configurations. In this group, Nd has an average coordination number close to 6.9. However, in the configuration with lowest energy, both cations still have an average coordination number of 7. Thus, the possible preference of Nd having a lower coordination number than Ce is not strong and is not linked to a specific ordering between cations and anions. Also, for $La_2Ce_2O_7$, several of the low energy configurations where cations are pyrochlore ordered including the *lowest energy* configuration have an average coordination number of 6.5 for Ce and 7.5 La. This indicates that Ce better accommodates a lower coordination number than La in $La_2Ce_2O_7$ when the cations are pyrochlore ordered. We will now turn to discuss the nature of the oxygen sublattice when the cations are ordered in the pyrochlore manner.

Why $Ln_2Ce_2O_7$ does not exhibit the pyrochlore structure

A number of previous structural analyses of $La_2Ce_2O_7$ have started with the perfect pyrochlore structure and explored various anti-Frenkel defects.[6,25,26] The most favourable Frenkel defect is created by moving a vacancy from the 8a to the 48f site:

$$v^{\times}_{i(8a)} + O^{\times}_{O(48f)} = v^{\bullet\bullet}_{O(48f)} + O^{//}_{i(8a)} \quad (1)$$

We therefore map, in Fig. 6, the energy for the different oxygen configurations with a fixed cation pyrochlore sublattice, as a function of the number of vacant crystallographic 8a positions of the pyrochlore (see the description of the structure in

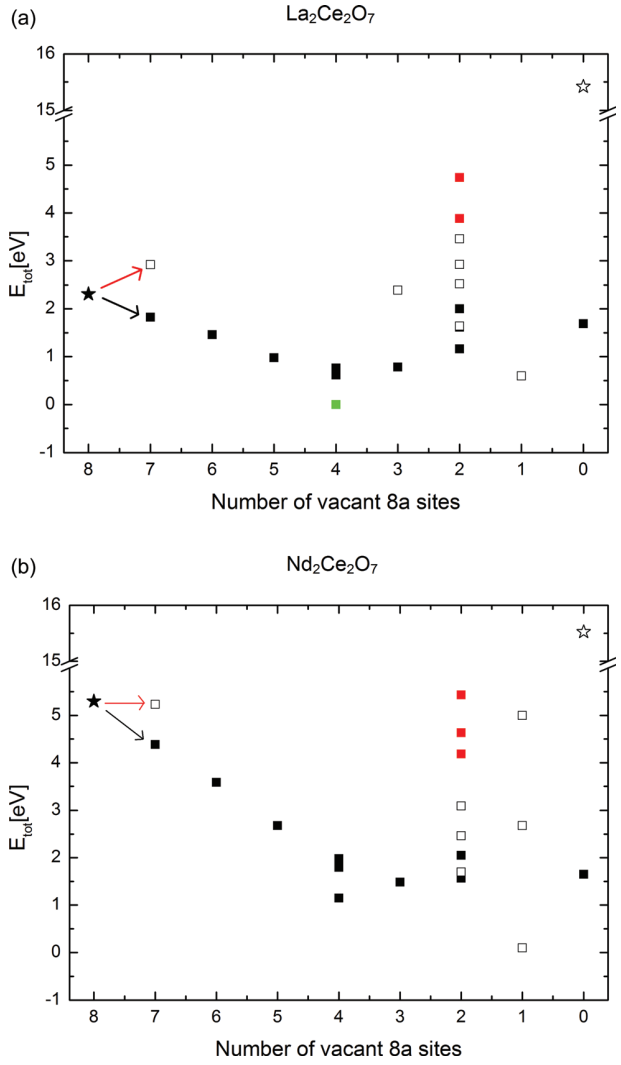

Fig. 6 Energies per 88 ion super cell as a function of the number of vacant 8a positions for (a) $La_2Ce_2O_7$ and (b) $Nd_2Ce_2O_7$. The cation sublattice is fixed to that of a pyrochlore. The filled black star represents the energy of the perfect pyrochlore structure where the oxygen sublattice also has a pyrochlore structure. Starting with the pyrochlore structure (space group $Fd\bar{3}m$, see Fig. 1(c)) with 8 vacant 8a positions, we can either move a vacancy to a 48f site (indicated by a black arrow for a single anti-Frenkel defect) or to a 8b site (indicated by a red arrow for a single anti Frenkel defect). The black filled squares represent configurations where one or several vacancies are moved from the 8a site to a 48f site only, whereas the open square represents configurations where at least one of the vacancies is moved to an 8b site. The red squares represent cations with less than 6 oxygens in the 1st coordination shell, and the open star represents the inverse pyrochlore structure where all 8b positions are vacant.

Fig. 1(c)). From Fig. 6, we immediately see that there are several anion configurations that are more stable than the pyrochlore structure (marked as a black star) for $La_2Ce_2O_7$, as well as for $Nd_2Ce_2O_7$. It is evident that the anti-Frenkel defect formation described in eqn (1) is exothermal (marked as a black arrow in Fig. 6). However, the lowest energy configuration for each compund is not found by creating one or two such defects, but requires the creation of several defects. This underlines that the structure of $La_2Ce_2O_7$ should not be viewed as a Frenkel defective pyrochlore because these defects are too extended to provide a meaningful description of its crystal structure. In fact, the perfect pyrochlore structure is more than 2 eV higher (per 88 ion supercell) in energy than the configuration with the lowest energy shown in the figure and is therefore not a representative structural model for $La_2Ce_2O_7$ at any temperature. The pyrochlore structure is even more energetically unfavourable for $Nd_2Ce_2O_7$ since its energy is more than 5.5 eV higher (per supercell) than the configurations with the lowest energy.

The *lowest energy* configuration for $La_2Ce_2O_7$ (marked as a filled green square in both Fig. 5(b) and 6(b)) has an oxygen sublattice that strongly resembles that found in the C-type structure. The decrease in energy when moving a vacancy from an 8a site to an adjacent 48f site in the pyrochlore structure is easily understood since ⟨111⟩ vacancy pairs are effectively replaced by more energetically favourable ⟨210⟩ motifs (as illustrated in Fig. 7). We can thus link the favourable formation of several anti-Frenkel defects to the C-type related ordering of vacancies. The *lowest energy* configuration for $La_2Ce_2O_7$ is obtained when moving half of the vacancies from the 8a position: 8 ⟨110⟩, 8 ⟨111⟩ and 24 ⟨210⟩ vacancy pairs (in our 88 ion supercell) compared to 32 ⟨111⟩ and 24 ⟨220⟩ vacancy pairs (and 0 ⟨210⟩ motifs) in the pyrochlore structure. The change in energy is even larger for $Nd_2Ce_2O_7$ when we move half of the vacancies from the 8a site, and here we find that the well-ordered "Ctype1" configuration has the lowest energy with 8 ⟨110⟩ vacancy pairs, no ⟨111⟩ motifs and the highest possible number of ⟨210⟩ alignments (which is 32).

The oxygen sublattice in the *lowest energy* configuration of $La_2Ce_2O_7$ is structurally more similar to the "Ctype1" configuration than it is to the oxygen structure in pyrochlore. Any similarity to the pyrochlore structure in the oxygen sublattice is dictated by the cation being ordered in the pyrochlore manner. In fact, the energy is ∼2.5 eV higher per 88 atom supercell if this particular oxygen configuration is combined with a random cation sublattice instead of a pyrochlore cation sublattice. The coupling between the two sublattices in the *lowest energy* configuration of $La_2Ce_2O_7$ is also seen by the lower average coordination number for Ce^{4+} than for La^{3+} as previously discussed, which is not found for any other cation configuration‡. The (larger) size mismatch between La^{3+} and Ce^{4+} seems to favour the pyrochlore packing of the cations, and may provide a possible explanation for why the oxygen arrangement in the *lowest energy* configuration of $La_2Ce_2O_7$ is different from the "Ctype1" configuration. It is probably seen by the surprising stability of ⟨111⟩ vacancy pairs when aligned *with* a Ce^{4+} ion in the cube centre. The resulting octahedra around Ce^{4+} are thus accommodated more easily in the oxygen sublattice when the cations are ordered in the pyrochlore manner.

The size mismatch between La^{3+} and Ce^{4+} in $La_2Ce_2O_7$ is, however, obviously not large enough to favour the perfect pyrochlore structure and a C-type ordering of the vacancies emerges as a consequence of the strongly favourable ⟨210⟩ motifs. This explains why a pyrochlore structure is not a representative

‡ See Figure A in additional information for energy *versus* coordination number of the cations.

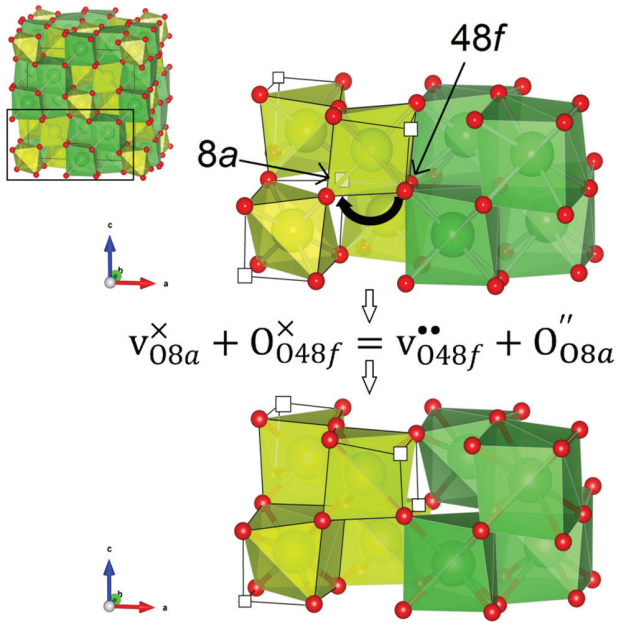

Fig. 7 Schematic illustration for the formation of an oxygen Frenkel defect where a vacancy is moved from an 8a site to a neighbouring 48f site. In this example, the number of ⟨111⟩ vac–vac alignments is strongly decreased and replaced by an increasing number of ⟨110⟩ and ⟨211⟩ vacancy pairs. The number of ⟨220⟩ pairs is decreased and the number of ⟨210⟩ alignments is increased. Alternatively, if the vacancy would have been moved to the 8b position (instead of a 48f site), a number of ⟨111⟩ vacancy pairs aligned in cubes containing Ce^{4+} in the centre position would have been replaced with ⟨111⟩ vacancy pairs located in empty cubes, and some ⟨220⟩ pairs would be substituted by unfavourable ⟨200⟩ vacancy pairs.

model for $La_2Ce_2O_7$ (or $Nd_2Ce_2O_7$) and we also stress that a perfect pyrochlore is not a suitable starting point for defining anion defects because the oxygen sublattice has an entirely different structure! For $La_2Ce_2O_7$, it seems that the lowest energy oxygen configuration entails a good compromise between the C-type related ordering of oxygens/vacancies and a pyrochlore cation ordering. However, we believe that the ordering of cations is difficult to capture experimentally due to kinetics, as we will discuss below.

Kinetic trapping limits cation ordering

When one synthesizes these compounds, the anion lattice will be able to relax and equilibrate fairly quickly upon cooling or quenching with relaxation times on the same order of magnitude as the residence time (~0.01 to 0.1 ns, see more in the next section when we calculate residence times of the oxygen ions from the MD trajectory). The diffusion of the cations is expected to be much slower.[27] The energetic gain of relaxing to the cation configuration with the lowest energy, is smaller compared to the enthalpic gain of forming a C-type vacancy order, especially for $Nd_2Ce_2O_7$. Also, since the C-type related ordering of vacancies appears to be low in energy for most cation sublattices, the presence of oxygen order does not provide a driving force for relaxing the cation sublattice to the most favourable cation configurations. A combination of the small enthalpy gain of locating the lowest energy cation configuration and slow cation diffusion, suggests that there is an extremely low probability of relaxing to a single ordered cation configuration at the timescales of the experiment. Such kinetic trapping has been discussed for various complex oxides with the fluorite-, pyrochlore- and perovskite structure.[28–30] Although we cannot rule out that the cations may order locally or even be quite long range ordered as expected from the ND (or XRD) diffraction patterns,[31] the findings in our previous experimental report on $La_2Ce_2O_7$ and $Nd_2Ce_2O_7$, do strongly suggest that the cations are disordered. We found no evidence for different coordination numbers for the two cations nor did we find any indications of order in the cation sublattice.[10] Also, test calculations carried out on both ordered and disordered cation sublattices using MD (within a modest sized 88 ion supercell) indicate that cation order does not strongly affect the anion mobility. Therefore, we decided to further investigate the nature of the oxygen structure and diffusivity in randomly chosen cation sublattices representing a plausible "frozen in cation disorder" scenario.

Nature of diffusion in $La_2Ce_2O_7$ and $Nd_2Ce_2O_7$

In Fig. 8, we plot the MSDs from MD runs at 1500 K for 3 × 3 × 3 super cells (297 atoms) of $La_2Ce_2O_7$ and $Nd_2Ce_2O_7$ where anions diffuse within a randomly chosen cation sublattice. The figure clearly shows that oxygen diffusion is faster in $La_2Ce_2O_7$ than in $Nd_2Ce_2O_7$.

From the MSDs we can calculate the diffusion coefficient for single ion diffusion and collective diffusion, D_{tracer} and $D_{\text{collective}}$:

$$D = \frac{1}{6t}|\text{MSD}|,$$

where t is the time and MSD is defined in the caption of Fig. 8. D_{tracer} for $La_2Ce_2O_7$ and $Nd_2Ce_2O_7$ is found to be 2.7×10^{-10} m^2 s^{-1}

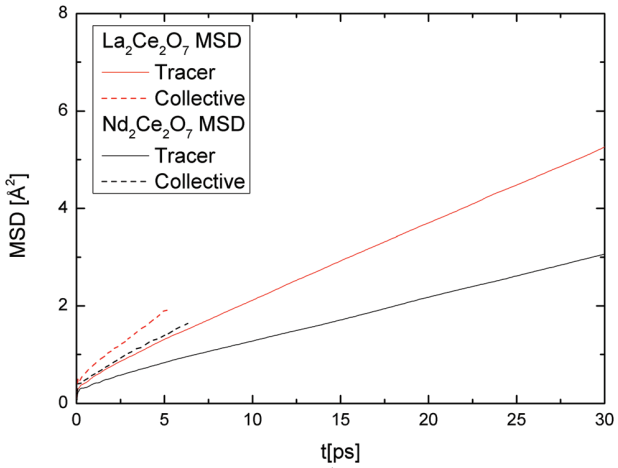

Fig. 8 Calculated tracer $\text{MSD}_{\text{tracer}} = \frac{1}{N}\sum_i \left|\vec{r_i}(t) - \vec{r_i}(0)\right|^2$ where r is the position of atom i and N is the number of atoms i, and collective $\text{MSD}_{\text{collective}} = \sum_i \left|\overrightarrow{R_i}(t) - \overrightarrow{R_i}(0)\right|^2$, where $\overrightarrow{R_i}(t) = \left(\overrightarrow{r_{i1}}(t) + \overrightarrow{r_{i2}}(t) \ldots \overrightarrow{r_{iN}}(t)\right)$, in 3 × 3 × 3 super cells of $La_2Ce_2O_7$ and $Nd_2Ce_2O_7$ at 1500 K in a random configurations of cations.

and 1.4×10^{-10} m^2 s^{-1} at 1500 K. A higher value for $La_2Ce_2O_7$ is in agreement with conductivity measurements showing a higher mobility of oxygen ions in $La_2Ce_2O_7$ than in $Nd_2Ce_2O_7$.[7] The diffusion coefficient can often be correlated with the degree of ion disorder (configurational entropy). However, when comparing two structurally similar compounds, such as $La_2Ce_2O_7$ and $Nd_2Ce_2O_7$, the diffusion coefficient cannot be used directly to measure the extent of local order since the lattice parameter is markedly larger in $La_2Ce_2O_7$ than in $Nd_2Ce_2O_7$. A larger lattice parameter leads to a longer hopping distance for an oxygen/vacancy and thus results in a higher value of diffusivity in $La_2Ce_2O_7$ than in $Nd_2Ce_2O_7$. The hopping frequency, Γ, on the other hand, found from a simple hopping model $\Gamma = \frac{n}{t} = 6\left(\frac{a}{4}\right)^{-2} D$, where n is the number of jumps and a is the lattice parameter, is a more meaningful parameter to measure the extent of local order in the two compounds. Γ is found to be 2.1×10^{10} s^{-1} for $La_2Ce_2O_7$ and 1.1×10^{10} s^{-1} for $Nd_2Ce_2O_7$ showing that oxygen jumps much more often in $La_2Ce_2O_7$ suggesting that $La_2Ce_2O_7$ has a higher mobility and is more disordered than $Nd_2Ce_2O_7$.

Also, the Haven ratio, $H = D_{tracer}/D_{collective}$, is correlated with local order (non-ideality) as it measures the extent of collective diffusion of oxygen ions. H quantifies the ratio between isolated single particle jumps and the centre of mass diffusion, which also include collective groups of migrating oxygens. To calculate the Haven ratio, we need $D_{collective}$, which is found from the $MSD_{collective}$ in Fig. 8 to be 4.5×10^{-10} m^2 s^{-1} and 3.2×10^{-10} m^2 s^{-1} for $La_2Ce_2O_7$ and $Nd_2Ce_2O_7$. The resulting H is about 0.60 and 0.44 for $La_2Ce_2O_7$ and $Nd_2Ce_2O_7$, respectively, and suggests that the oxygens move rather collectively in both compounds, but more so in $Nd_2Ce_2O_7$. This is entirely consistent with more anion order in $Nd_2Ce_2O_7$ than in $La_2Ce_2O_7$.

Dynamic disorder

To analyse the nature of dynamic disorder in $La_2Ce_2O_7$ and $Nd_2Ce_2O_7$, we plot in Fig. 9 oxygen vacancy pairs sampled from

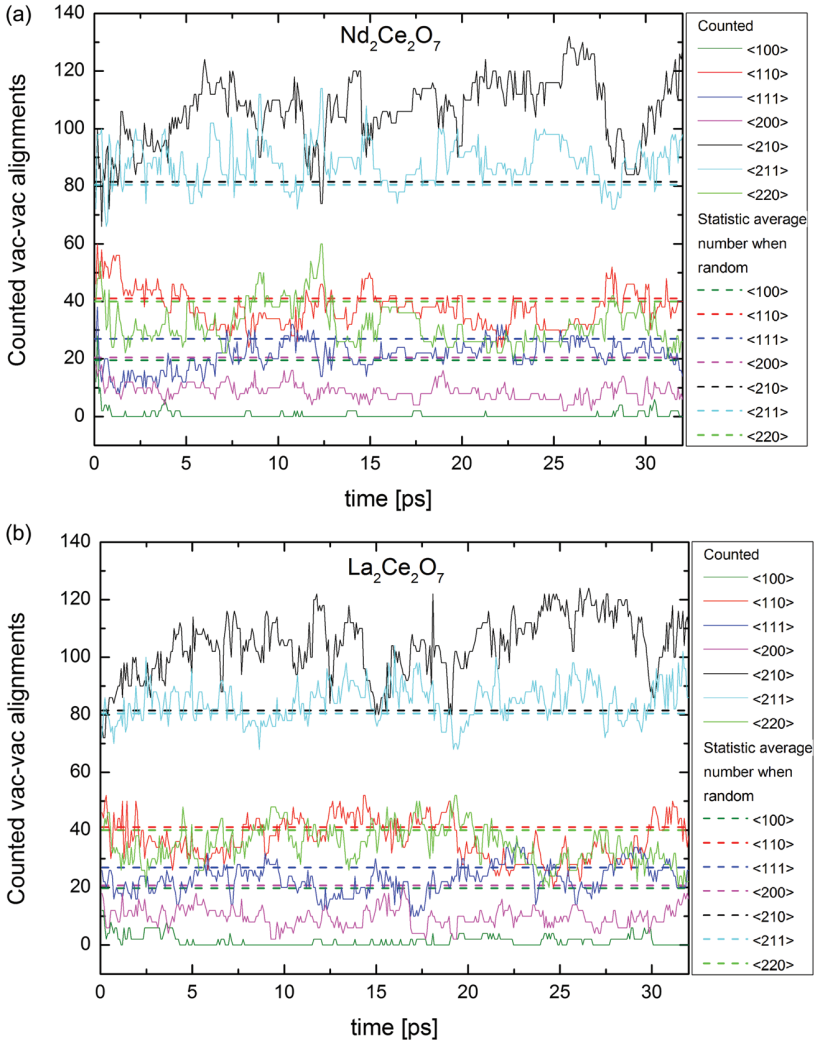

Fig. 9 Sampled vac–vac alignments in a 3 × 3 × 3 supercell of (a) $La_2Ce_2O_7$ and (b) $Nd_2Ce_2O_7$ fluorites during the first 32 ps of the MD simulations at 1500 K with a randomly chosen initial configuration of the oxygens and cations. The horizontal dashed lines with matching color codes represent the number expected from a random distribution of oxygen.

the MD runs at 1500 K within a randomly chosen sublattice of cations. The dynamically disordered structure has very similar distributions of vac–vac motifs compared to the ''static'' structures shown in Fig. 5. That is, the ones that are low in energy in the static picture are more frequently found in the MD runs and those that are high in energy are more rarely seen in the MD runs. Both compounds have a high number of ⟨210⟩ motifs compared to that expected from a random distribution of vacancies in our simulation box, which is consistent with results from the static optimisations that show that low energy configurations always contain many ⟨210⟩ vac–vac pairs linked to C-type related ordering. The number of ⟨210⟩ vacancy alignments is higher, and there are fewer ⟨220⟩ alignments in $Nd_2Ce_2O_7$ compared to $La_2Ce_2O_7$, showing a weaker tendency in the latter. Few ⟨100⟩ and ⟨200⟩ vacancy pairs are sampled for both compositions, which is also relatable to the C-type structure, however there are more of them in $La_2Ce_2O_7$ than in $Nd_2Ce_2O_7$, and they are stable for a longer time in $Nd_2Ce_2O_7$. This is consistent with $La_2Ce_2O_7$ being more oxygen disordered and possessing higher oxygen ion mobility as we discussed earlier.

Since an oxygen jumps in the crystallographic ⟨100⟩ direction in the fluorite structure, there will be many more possibilities for single particle jumps in $La_2Ce_2O_7$ than in $Nd_2Ce_2O_7$ since we see many more unfavourable ⟨100⟩ configurations in $La_2Ce_2O_7$. There is also a higher average number of ⟨110⟩ and ⟨111⟩ vacancy pairs in $La_2Ce_2O_7$. Finally, *all* other vacancy-pairs than ⟨100⟩ and ⟨200⟩ seem to be longer lived in $Nd_2Ce_2O_7$, as seen by the more and longer ''plateaus'' in the plot, which is in accordance with more collective diffusion and more long range order.

Linking the extent of local order and kinetic trapping

The nature of dynamical disorder is closely connected to the extent of local (static) order and non-ideality, which can be measured from the number of thermally populated low-energy configurations. Although $La_2Ce_2O_7$ appears to be more disordered (less non-ideal) than $Nd_2Ce_2O_7$ as discussed in the previous chapter from the MD runs, this is not evident when comparing directly the energy spectra of $La_2Ce_2O_7$ and $Nd_2Ce_2O_7$ since the spectra are quite similar. The main difference between the two energy spectra, as shown in Fig. 5 and 6, is that the energy gap between the lowest and next lowest energy configuration is much larger in $La_2Ce_2O_7$, which could indicate that $Nd_2Ce_2O_7$ would be more disordered than $La_2Ce_2O_7$. However, Fig. 5 and 6 do not show the multiplicity of each configuration and since the lowest energy configuration for $La_2Ce_2O_7$ has a lower symmetry than the lowest energy configuration for $Nd_2Ce_2O_7$, it will have several symmetrically equivalent oxygen configurations and $La_2Ce_2O_7$ will have more thermally accessible configurations than $Nd_2Ce_2O_7$. This implies in turn that $La_2Ce_2O_7$ has higher configurational entropy than Nd_2Ce_2O and is thus more disordered. In addition to this, GGA+U calculations reported in Table 2 in the additional information show that the configurations with the next lowest energies for $La_2Ce_2O_7$ configurations lie much closer in energy to the lowest energy one than what was found using GGA (without +U). These configurations will be more thermally accessible for $La_2Ce_2O_7$, which provides additional support for the ND results, showing that $La_2Ce_2O_7$ is the most disordered of the two.[10]

However, the argument above assumes that the cations are able to fully relax to reach the equilibrium cation configuration. If we assume that the cations are entirely disordered due to kinetic trapping, we should remove all ordered cation configurations including the *lowest energy* configuration for $La_2Ce_2O_7$, which is the green square in Fig. 5(b). Then, the two compounds should actually have very similar diffraction spectra, but this contrasts the experimental observations mentioned above.[10] In this case, static disorder therefore does not explain why $La_2Ce_2O_7$ is more disordered than $Nd_2Ce_2O_7$ and the higher degree of disorder in $La_2Ce_2O_7$ observed experimentally can only be explained by dynamic oxygen disorder. In $Nd_2Ce_2O_7$, we observe more configurations with a large number of ⟨210⟩ vacancy pairs during the MD runs, and these motifs are natural ''building blocks'' to form partial long range order connectivity patterns consistent with the C-type structure. In $La_2Ce_2O_7$, we suggest that C-type related oxygen ordering is more short ranged in nature, with ⟨110⟩ and (empty) ⟨111⟩ vacancy pairs occurring more often during the MD runs. This could explain why diffraction peaks characteristic for C-type order are seen in $Nd_2Ce_2O_7$ whereas such order is only visible as modulations of the (diffuse) background scattering for $La_2Ce_2O_7$.[10]

4. Concluding remarks

Here, we explored the local structure of the fluorite structured $La_2Ce_2O_7$ and $Nd_2Ce_2O_7$ through a comparison of a large number of cation configurations in the static limit and from Born–Oppenheimer Molecular dynamics calculations using DFT. We found that anion ordering is more pronounced than cation ordering. Both compounds have a strong preference towards a C-type related order of oxygen vacancies, and this order is largely independent of the ordering or disordering of the cations. The C-type like order is identified by a high fraction of ⟨210⟩ vacancy pairs, and ⟨100⟩ pairs are unfavorable as opposed to the ⟨110⟩ and ⟨111⟩ vacancy pairs. However, ⟨111⟩ vac–vac configurations are only favorable when aligned in an oxygen cube without a cation in the cube centre. The vacancies should also be distributed in a way that is consistent with cation coordination numbers between 6 and 8.

Lattice static calculations show that there is an energetic advantage of particular ordering in the cation sublattice which is explained by maximising the close packing of the cations. Whereas the lowest energy configuration of $Nd_2Ce_2O_7$ has the ordered configuration named ''fluorite'', the larger size difference between La^{3+} and Ce^{4+} in $La_2Ce_2O_7$ is better suited to the pyrochlore cation structure (see Computational methods and details for description). However, we argue that the cations might be ''frozen in'' and hence disordered under experimental conditions. We also stress that although the cation sublattice in the *lowest energy* configuration of $La_2Ce_2O_7$ possesses the pyrochlore structure, the perfect pyrochlore is not the most stable configuration for $La_2Ce_2O_7$ (nor for $Nd_2Ce_2O_7$).

Both long range and short range vacancy interactions will influence the properties such as conductivity, and the nature of oxygen diffusion is here studied within a random cation sublattice based on our assumption of a ''frozen in'' disordered cation sublattice. $La_2Ce_2O_7$ is here found to have higher oxygen diffusion than $Nd_2Ce_2O_7$. Collective chains are more dominant in $Nd_2Ce_2O_7$ than in $La_2Ce_2O_7$ with Haven ratios – which measure the single particle to collective diffusion – of about 0.44 and 0.60, respectively. A lower Haven ratio is consistent with stronger order in the former.

Our present results show that previous computational models where $La_2Ce_2O_7$ has been viewed as a pyrochlore with one or two Frenkel defects, are not representative structural models of this compound. On the other hand, when modelling $La_2Ce_2O_7$ or $Nd_2Ce_2O_7$ as a disordered fluorite with a random distribution of vacancies, one ignores the fact that these compounds have a preference towards (local or long range) C-type related order of the oxygen sublattice. C-type oxygen order is found to be more dominant in $Nd_2Ce_2O_7$ than in $La_2Ce_2O_7$, and the observed higher amount of $\langle 210 \rangle$ vacancy pairs in the former suggests that the stacking of ''Ctype1'' (and other low energy) configurations forms more long range order in $Nd_2Ce_2O_7$ than in $La_2Ce_2O_7$.

Conflicts of interest

There are no conflicts of interest to declare.

Acknowledgements

The authors gratefully knowledge the Norwegian Metacentre for Computational Science (Notur) for providing computational resources under the project number nn4604k and nn2916k. This work was partly supported by the Research Council of Norway through its Centres of Excellence funding scheme project 223272.

References

1 C. E. Mohn, *et al.*, Order in the disordered state: local structural entities in the fast ion conductor $Ba_2In_2O_5$, *J. Solid State Chem.*, 2005, **178**(1), 346–355.
2 C. E. Mohn, N. L. Allan and S. Stolen, Sr and Ga substituted $Ba_2In_2O_5$. Linking ionic conductivity and the potential energy surface, *Solid State Ionics*, 2006, **177**(3–4), 223–228.
3 L. Minervini, R. W. Grimes and K. E. Sickafus, Disorder in Pyrochlore Oxides, *J. Am. Ceram. Soc.*, 2000, **83**(8), 1873–1878.
4 V. Besikiotis, *et al.*, Crystal structure, hydration and ionic conductivity of the inherently oxygen-deficient $La_2Ce_2O_7$, *Solid State Ionics*, 2012, **228**, 1–7.
5 W. Sun, S. Fang, L. Yan and W. Liu, Investigation on Proton Conductivity of $La_2Ce_2O_7$ in Wet Atmosphere: Dependence on Water Vapor Partial Pressure, *Fuel Cells*, 2012, **12**(3), 457–463, DOI: 10.1002/fuce.201100175.
6 D. E. P. Vanpoucke, *et al.*, Density functional theory study of $La_2Ce_2O_7$: Disordered fluorite versus pyrochlore structure, *Phys. Rev. B: Condens. Matter Mater. Phys.*, 2011, **84**(5), 054110.
7 H. Yamamura, *et al.*, Crystal Phase and Electrical Conductivity in the Pyrochlore-Type Composition Systems, $Ln_2Ce_2O_7$ (Ln = La, Nd, Sm, Eu, Gd, Y and Yb), *J. Ceram. Soc. Jpn.*, 2003, **111**(1300), 902–906.
8 H. Yamamura, H. Nishino and K. Kakinuma, Ac Conductivity for $Eu_2Zr_2O_7$ and $La_2Ce_2O_7$ with Pyrochlore-Type Composition, *J. Ceram. Soc. Jpn.*, 2004, **112**(1310), 553–558.
9 E. Reynolds, *et al.*, Structural and spectroscopic studies of $La_2Ce_2O_7$: Disordered fluorite versus pyrochlore structure, *Phys. Rev. B: Condens. Matter Mater. Phys.*, 2012, **85**(13), 132101.
10 L.-E. Kalland, *et al.*, C-type related order in the defective fluorites $La_2Ce_2O_7$ and $Nd_2Ce_2O_7$ studied by neutron scattering and ab initio MD simulations, *Phys. Chem. Chem. Phys.*, 2016, **18**(34), 24070–24080.
11 T. Hagiwara, *et al.*, Formation of C-type rare earth structures in the $Ce_{1-x}Nd_xO_{2-\delta}$ system: a factor in the decrease in oxide-ion conductivity, *J. Ceram. Soc. Jpn.*, 2009, **117**, 1306–1310.
12 D. R. Ou, *et al.*, Oxygen vacancy ordering in heavily rare-earth-doped ceria, *Appl. Phys. Lett.*, 2006, **89**(17), 171911.
13 R. L. Withers, *et al.*, Microdomains, Solid Solutions and the ''Defect Fluorite'' to C-Type Sesquioxide Transition in CeO_2-$RO_{1.5}$ and ZrO_2-$RO_{1.5}$ Systems, *J. Solid State Chem.*, 1995, **120**(2), 290–298.
14 J. P. Perdew, K. Burke and M. Ernzerhof, Generalized Gradient Approximation Made Simple, *Phys. Rev. Lett.*, 1996, **77**(18), 3865–3868.
15 P. E. Blochl, C. J. Forst and J. Schimpl, Projector augmented wave method: ab initio molecular dynamics with full wave functions, *Bull. Mater. Sci.*, 2003, **26**, 33–41.
16 G. Kresse and J. Furthmueller, Efficient iterative schemes for ab initio total-energy calculations using a plane-wave basis set, *Phys. Rev. B: Condens. Matter Mater. Phys.*, 1996, **54**, 11169–11186.
17 A. Spek, Structure validation in chemical crystallography, *Acta Crystallogr., Sect. D: Biol. Crystallogr.*, 2009, **65**(2), 148–155.
18 D. E. P. Vanpoucke, *et al.*, Aliovalent doping of CeO_2: DFT study of oxidation state and vacancy effects, *J. Mater. Chem. A*, 2014, **2**(33), 13723–13737.
19 T. Zacherle, *et al.*, Ab initio analysis of the defect structure of ceria, *Phys. Rev. B: Condens. Matter Mater. Phys.*, 2013, **87**(13), 134104.
20 M. Nolan, *et al.*, Density functional theory studies of the structure and electronic structure of pure and defective low index surfaces of ceria, *Surf. Sci.*, 2005, **576**(1), 217–229.
21 J. K. Lang, Y. Baer and P. A. Cox, Study of the 4f and valence band density of states in rare-earth metals. II. Experiment and results, *J. Phys. F: Met. Phys.*, 1981, **11**(1), 121–138.
22 F. Chen, *et al.*, Structure and luminescence properties of a Nd^{3+} doped Bi4Ge3O12 scintillation crystal: new insights from a comprehensive study, *J. Mater. Chem. C*, 2017, **5**(12), 3079–3087.
23 J. Feng, *et al.*, Electronic structure, mechanical properties and thermal conductivity of $Ln_2Zr_2O_7$ (Ln = La, Pr, Nd,

Sm, Eu and Gd) pyrochlore, *Acta Mater.*, 2011, **59**(4), 1742–1760.

24 X. Liu, *et al.*, Local structural changes in $Ce_{1-x}Ln_xO_{2-\delta}$ (Ln = La, Gd) solid electrolytes, *Solid State Ionics*, 2020, **347**, 115213.

25 Q. Zhang, *et al.*, Structural Stability of $La_2Ce_2O_7$ as a Proton Conductor: A First-Principles Study, *J. Phys. Chem. C*, 2013, **117**(40), 20379–20386.

26 T. S. Bjørheim, V. Besikiotis and R. Haugsrud, Hydration thermodynamics of pyrochlore structured oxides from TG and first principles calculations, *Dalton Trans.*, 2012, **41**(43), 13343–13351.

27 M. Martin, Diffusion in Oxides, in *Diffusion in Condensed Matter: Methods, Materials, Models*, ed. P. Heitjans and J. Kärger, 2005, Springer Berlin Heidelberg, Berlin, Heidelberg, pp. 209–247.

28 A. S. Nowick, 3 – Atom Transport in Oxides of the Fluorite Structure, in Diffusion in *Crystalline Solids*, ed. G. E. Murch and A. S. Nowick, 1984, Academic Press, pp. 143–188.

29 Y. Liu, R. L. Withers and L. Norén, The pyrochlore to 'defect fluorite' transition in the $Y_2(Zr_yTi_{1-y})_2O_7$ system and its underlying crystal chemistry, *J. Solid State Chem.*, 2004, **177**(12), 4404–4412.

30 S. Švarcová, *et al.*, Structural instability of cubic perovskite $Ba_xSr_{1-x}Co_{1-y}FeyO_{3-\delta}$, *Solid State Ionics*, 2008, **178**(35), 1787–1791.

31 F. Brisse and O. Knop, Pyrochlores. II. An investigation of $La_2Ce_2O_7$ by neutron diffraction, *Can. J. Chem.*, 1967, **45**(6), 609–614.

Paper III

Structure, hydration, and proton conductivity in 50% La and Nd doped CeO_2 – $La_2Ce_2O_7$ and $Nd_2Ce_2O_7$ – and their solid solutions

L-E. Kalland, A. Løken, T. S. Bjørheim, R. Haugsrud and T. Norby, Solid State Ionics, 2020, 354, 115401-115408

DOI: 10.1016/j.ssi.2020.115401

Solid State Ionics 354 (2020) 115401

Contents lists available at ScienceDirect

Solid State Ionics

journal homepage: www.elsevier.com/locate/ssi

Structure, hydration, and proton conductivity in 50% La and Nd doped CeO_2 – $La_2Ce_2O_7$ and $Nd_2Ce_2O_7$ – and their solid solutions

Liv-Elisif Kalland[a,*], Andreas Løken[a,b], Tor S. Bjørheim[a], Reidar Haugsrud[a], Truls Norby[a]

[a] Centre for Materials Science and Nanotechnology, Department of Chemistry, University of Oslo, FERMiO, Gaustadalléen 21, NO-0349 Oslo, Norway
[b] Jotun Performance Coatings, Jotun A/S, NO-3202 Sandefjord, Norway[1]

ARTICLE INFO

Keywords:
TG-DSC
C-type structure
Fluorite structure
Hydration
Proton conductivity
Vacancy ordering

ABSTRACT

We have measured water uptake and hydration enthalpy in 50% La and Nd doped CeO_2, also to be taken as compositions in the series $La_{2-x}Nd_xCe_2O_7$ (x = 0.0, 0.5, 1.0 and 2.0) using combined thermogravimetry (TG) and differential scanning calorimetry (DSC), TG-DSC. The TG-DSC data unambiguously yield standard molar hydration enthalpies of ~−74 kJ/mol independent of water uptake. The interpretation of the TG results, however, does not fit a classical model of hydration of all oxygen vacancies. Instead, the hydration appears to be limited to a small fraction of the free vacancies. Hydration further decreases as the Nd content (x) and long-range order increases and regions of disorder decrease. We propose a new model explaining why hydration occurs only in a small fraction of the nominally free vacancies: The higher basicity of La/Nd compared to Ce promotes protonation at oxide ion sites with high coordination to La/Nd, and the observed water uptake and modelling suggests that mainly oxide ions fully coordinated to 4 La/Nd neighbours become protonated. The statistical variation of coordination around oxygen sites in a disordered fluorite oxide creates a limited number of such oxide ions sites which results in limited hydration. The model matches well the experimental results and DFT calculations of proton trapping at the fully La-coordinated sites for 50% La-doped CeO_2, and also rationalizes conductivity data.

1. Introduction

$Ln_2Ce_2O_7$ with Ln = La or other large lanthanides is sometimes referred to as 50% lanthanide-doped ceria since the structure remains related to the cubic ceria parent structure [1–3]. Adhering to the Kröger-Vink notation, the doping reaction can then be written as:

$$Ln_2O_3 = 2Ln'_{Ce} + 3O_O^{\times} + v_O^{\bullet\bullet} \quad (1)$$

This results in 1 oxygen vacancy per formula unit $Ln_2Ce_2O_7$. The structure may as such potentially incorporate one molecule of water, i.e., two protons, per vacancy if the material is fully hydrated:

$$H_2O_{(g)} + O_O^{\times} + v_O^{\bullet\bullet} = 2OH_O^{\bullet} \quad (2)$$

In support of this, $La_2Ce_2O_7$, which exhibits oxide ion conductivity in the dry state, has been reported to hydrate and exhibit proton conduction in the presence of water vapour [2]. From reaction (2) it is evident that a lower stability (higher energy) of the oxygen vacancy, or a higher stability (lower energy) of the hydroxide species, will result in more favourable hydration thermodynamics [4,5]. Hydration enthalpies in oxides can range from endothermic values such as in undoped ceria [6] to highly exothermic for a wide range of oxides including rare earth sesquioxides [7,8], pyrochlores [9], and perovskites [10,11].

High concentrations of defects, for instance by high doping levels, can induce a number of defect-defect interactions, and corresponding associates will affect the concentrations of free defects, the degree of hydration, and the apparent mobility of defects. These can comprise vacancy-vacancy pairs, vacancy-dopant pairs, vacancy-double dopant clusters, proton-dopant pairs and clusters, and long-range order of vacancies and dopant-vacancy constellations. Accordingly, lanthanide-doped ceria (Ln-CeO_2) shows a steep decrease in the oxide ion conductivity when doping levels increase above 10–20 mol% [1,3,12,13]. While ceria with moderate acceptor doping levels exhibits negligible protonation and bulk proton conductivity [5], ceria heavily doped with some large lanthanides, such as 50% La-doping corresponding to $La_2Ce_2O_7$, can be hydrated and shows significant proton conductivity at lower temperatures in wet atmospheres [2,14]. This we may qualitatively attribute to the higher basicity of the large lanthanides, notably La and Nd, relative to that of Ce.

* Corresponding author.
E-mail address: l.e.kalland@kjemi.uio.no (L.-E. Kalland).
[1] Current affiliation.

https://doi.org/10.1016/j.ssi.2020.115401
Received 19 December 2019; Received in revised form 18 June 2020; Accepted 29 June 2020

When comparing previous studies we find that the oxide ion conductivity, amount of hydration, and proton conductivity all decrease from $La_2Ce_2O_7$ to $Nd_2Ce_2O_7$ [2,14–16]. Structural investigations in the $La_{2-x}Nd_xCe_2O_7$ system showed indications of increasing long-range ordering of oxygen vacancies from La to Nd (increasing x) [17]. Ordering increases the stability of oxygen vacancies and one may expect this to affect the amount of water uptake through the compositional series investigated here.

Here, we investigate how the high doping level (basicity) and ordering impact hydration by a study of the water uptake and thermodynamics of hydration in the $La_{2-x}Nd_xCe_2O_7$ series (x = 0.0, 0.5, 1.0 and 2.0) using combined thermogravimetry and differential scanning calorimetry (TG-DSC), as well as electrical characterization. We compare the thermodynamic parameters obtained by fitting the water uptake data from TG-DSC to the classical model for acceptor doped oxides as described by for example Kreuer [10], and the results from measuring the hydration enthalpy directly by combined TG-DSC as demonstrated by Kjølseth et al. [11]. Conductivity measurements performed in wet and dry atmospheres determine the contribution of proton conductivity for the series. The observed levels of hydration and hydration enthalpies are discussed in relation to long-range structural order through the series and a new approach to local site and coordination energetics as a result of high doping levels.

2. Experimental details

Combined thermogravimetry (TG) and differential scanning calorimetry (DSC), TG-DSC, were conducted on powder samples with the compositions $La_{2-x}Nd_xCe_2O_7$ (x = 0.0, 0.5, 1.0, and 2.0). The powders were prepared by solid state reaction and heat treated in several cycles with a final temperature of 1400 °C yielding almost phase pure samples based on Rietveld analysis of long scan powder X-ray diffraction data (XRD). The Rietveld analysis determined the impurities to be 0.05 wt% of $La_{9.33}(SiO_4)_6O_2$ in the $La_2Ce_2O_7$ sample and 0.002–0.004 wt% of Nd_2O_3 in the Nd containing samples. Moreover, the structure of the samples was characterized using XRD and neutron powder diffraction (ND), and analysed using Rietveld and the reverse Monte Carlo method. For detailed descriptions of sample preparation, XRD and ND, and interpretations thereof, see [17].

TG-DSC measurements were performed using a Netzsch Simultaneous Thermal Analyzer (STA 449C Jupiter) connected to a water vapour generator providing an atmosphere of pH_2O = 1 atm. The powder samples were dried at 1000 °C for 60 min and thereafter equilibrated in dry N_2 (or O_2 for two of the measurement series) at the given temperature prior to the hydration by introduction of steam. The background was determined running an empty crucible under identical conditions and the background was subtracted from the measurements. Fig. 1 shows examples of DSC and TG curves upon hydration for the different compositions at 250 °C. The water uptake is determined from the mass change, while the heat exchange associated with the water uptake is extracted by integration of the DSC signal using a sigmoidal shape to account for the baseline shift. By dividing the heat exchange by concentration of water, we obtain the hydration enthalpy ΔH_{hydr} per mole of H_2O at the given temperature.

Before we turn to results, we mention two possible complications of the measurements, and how we have addressed them. First, since compositions containing high levels of Nd have been suggested to take up some oxygen under oxidizing conditions [15] due to the slight tendency of Nd^{3+} to be oxidized to Nd^{4+}, hydration measurements for $LaNdCe_2O_7$ and $Nd_2Ce_2O_7$ are also conducted in O_2 for comparison. We do not find significantly different water uptakes in O_2 vs N_2, and conclude therefore that oxidation does not affect the defect structure significantly, i.e., electron holes are minority defects.

Secondly, the measured water uptake for the end member $Nd_2Ce_2O_7$ is particularly low, and chemisorbed water or the formation of hydroxide phases of the Nd_2O_3 impurity phase could in principle account for a significant part of the total water uptake. Based on preliminary BET studies and estimates of the amount of Nd_2O_3 from XRD, the maximum water uptake from these would correspond to 0.007 and 0.012–0.024 mol H_2O per mol oxide, respectively. We rule out a major effect of hydroxide formation because at the fixed high water vapour pressure we apply, this should manifest itself as steps in the TG curve. Our data exhibit no steps, but rather a behaviour resembling hydration of an acceptor doped oxide as seen in many works (e.g. [10]). Based on this the measurements for $Nd_2Ce_2O_7$ will be discussed assuming that the mass changes are due to hydration, although we cannot rule out the possibility that adsorption and hydroxide formation influence the data for this compound.

Electrical characterization was carried out on pellets made by pressing the same powders as used for structural characterization using a 20 mm die, at 125 MPa pressure. All samples were sintered at 1400 °C for 5 h, heated with a ramp rate of 300°/h, and cooled with a ramp rate of 140°/h. After sintering the samples exhibited a relative density of approximately 60%. Electrodes were made by painting three layers of

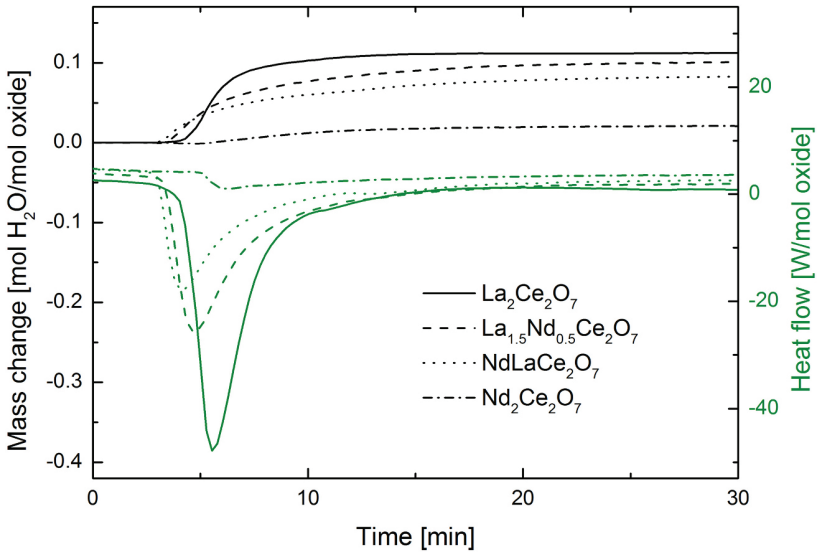

Fig. 1. TG and DSC curves upon hydration (pH_2O = 1 atm) at 250 °C for $La_{2-x}Nd_xCe_2O_7$ with x = 0.0, 0.5, 1.0 and 2.0.

platinum ink (Metalor Pt-ink 6926) on each side of the samples and dried. A Pt grid was added with the last Pt-layer, and the electrode was finally annealed according to the ink specifications.

Electrical characterization was performed by using a 2-point 4 wire setup mounting the samples in a ProboStat™ (NORECS, Norway) and connected to an impedance spectrometer (Solartron 1260 FRA). The conductivity data reported are measured at 10 kHz while impedance sweeps were recorded for some conditions covering the experimental window to ensure that the constant frequency conductivities reflect bulk properties.

3. Results and discussion

3.1. Water uptake and thermodynamic values

Fig. 2 shows the water uptake for each composition based on the relative mass changes measured by TG-DSC (squares). All the compositions hydrate to some extent. This can be taken to be hydration of a nominally undoped oxide by introduction of two defects, for instance oxygen interstitials and protons, or it can be taken to represent hydration of oxygen vacancies present to charge compensate acceptor dopants, as described above. In any case, the expected maximum hydration is the same in the $Ln_2Ce_2O_7$ series, corresponding to one mole of water per mole of oxide. However, attempts to fit the data to this model with a fixed maximum hydration level of 1 mol/mol oxide result in very poor fits, even when using data only above 250 °C. The fitted standard hydration entropies are reasonable (of the order of −130 J/mol K) but the standard hydration enthalpies in the order of −40 to −50 kJ/mol are, as we shall see later, much less negative than corresponding values from TG-DSC, which are of the order of −70 kJ/mol. Hence, this model appears inapplicable and is not pursued further here.

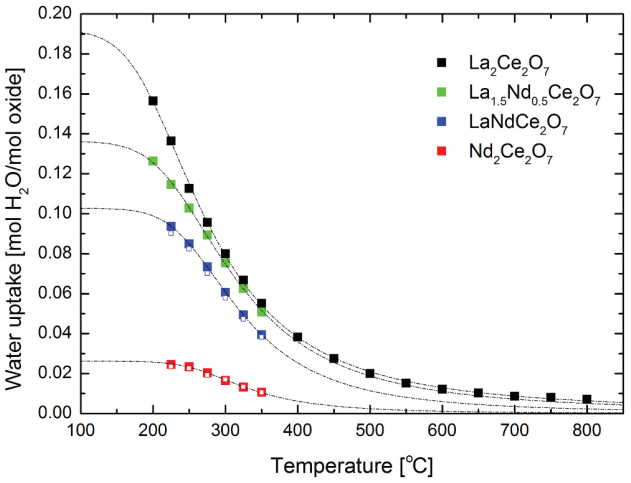

Fig. 2. Measured water uptake for each of the compositions (solid and open squares, respectively, for N_2 and O_2 atmospheres) along with curve-fitted lines based on a defect chemical model with variable effective acceptor level and corresponding maximum water uptake appearing as the plateaus at low temperatures.

Instead, we analyse the data in a first approach according to a model where the maximum hydration is a variable quantity which we fit to the data along with the standard entropy and enthalpy of hydration. We solve three equations, namely the equilibrium coefficient for the reaction in Eq. (2),

$$K_{Hydr} = \exp\left(-\frac{\Delta H^{\circ}_{hydr}}{RT}\right)\exp\left(\frac{\Delta S^{\circ}_{hydr}}{R}\right) = \frac{[OH^{\bullet}_{O}]^2}{[v^{\bullet\bullet}_{O}][O^{x}_{O}]p_{H_2O}} \quad (3)$$

the constancy of the sum of charges from available oxygen vacancies and hydroxide ions, corresponding to an effective variable acceptor level (a model used earlier in similar studies of acceptor doped oxides [18,19]),

$$[Acc'_{eff}] = 2[v^{\bullet\bullet}_{O}] + [OH^{\bullet}_{O}], \quad (4)$$

and the oxide ion site balance made up from effectively neutral structural empty oxygen sites, available charged oxygen vacancies, and hydroxide ions,

$$[O^{x}_{O}] = 8 - ([v^{x}_{O}] + [v^{\bullet\bullet}_{O}] + [OH^{\bullet}_{O}]) \quad (5)$$

where the three variables ΔH°_{hydr}, ΔS°_{hydr} and $[v_O^{\bullet\bullet}]$ are the standard hydration enthalpy and entropy and the molar concentration of available, or free, oxygen vacancies, respectively. In this approach, the neutral (structural) empty oxygen sites vary between 1 per formula unit for a fully ordered system and 0 for a fully disordered one, expressed by the level of effective acceptors; $[v^{x}_{O}] = 1 - \frac{1}{2}[Acc'_{eff}]$. The molar concentration of protons $[OH_O^{\bullet}]$ is given by the measured water uptake $[OH_O^{\bullet}] = 2[H_2O]$ (from Eq. (2)), and p_{H_2O} is set to the value used for the hydration isobars, namely 1 atm.

Resulting saturation levels, enthalpies and entropies are listed in Table 1 along with the standard deviation resulting from the curve fitting. The modelled curves corresponding to the derived parameters are included in Fig. 2.

When analysing the combined TG-DSC data we obtain a mean value and standard deviation when comparing the evaluated enthalpies for each temperature within a specified temperature range. The extracted molar enthalpies of hydration and the standard deviation (based on the difference between results at different temperatures) are included in Table 1 and Fig. 3. The uncertainty of the extracted parameters increases with increasing temperature and Nd-content, as the water uptake and accompanying heat exchange diminish. The data point at 350 °C, which forms an outlier enthalpy, is hence omitted when calculating the mean values for $Nd_2Ce_2O_7$.

The mean standard enthalpies of hydration determined by TG-DSC are remarkably similar for all the compositions, with an average value of −74 kJ/mol, however there seems to be a trend of decreasingly exothermic hydration enthalpies with increasing content of Nd. The same parameter extracted from fitting the measured water uptake (see Table 1) with a variable saturation limit comes out at qualitatively

Table 1
Thermodynamic values from fitting of the measured water uptake and the extracted hydration enthalpies from TG-DSC. The uncertainties reflect standard deviation based on the data sets averaged and curve-fitted. Actual uncertainties including systematic errors will be larger.

Compound	Hydration parameters fitted to a model with limited effective acceptor level and water uptake saturation			Enthalpies from TG-DSC
	Saturation level [mol H_2O/mol $Ln_2Ce_2O_7$]	ΔS°_{hydr} [J/mol K]	ΔH°_{hydr} [kJ/mol]	ΔH°_{hydr} [kJ/mol] (200–350 °C)
$La_2Ce_2O_7$	0.191 ± 0.004	−128 ± 1	−57 ± 1	−77 ± 3
$La_{1.5}Nd_{0.5}Ce_2O_7$	0.136 ± 0.002	−134 ± 4	−63 ± 2	−74 ± 3
$LaNdCe_2O_7$	0.1027 ± 0.0005	−157 ± 1	−76 ± 1	−73 ± 3
$Nd_2Ce_2O_7$	0.0260 ± 0.0006	−188 ± 10	−89 ± 6	−72 ± 12

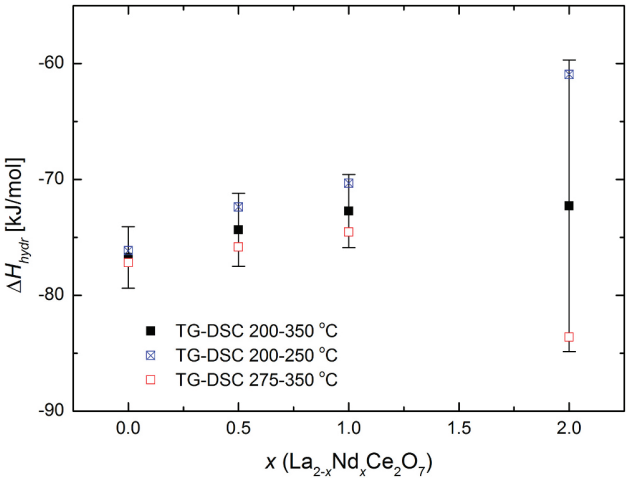

Fig. 3. Average enthalpies from TG-DSC as a function of x for all temperatures (black) with std. error and for temperatures above and below 250 °C (red 275–350 °C, blue 200–250 °C).

similar values, but the correlation between the three fitted parameters is large and the uncertainties are much bigger than those from the fitting statistics alone.

In comparison with the hydration enthalpy of approximately −77 kJ/mol for $La_2Ce_2O_7$ determined by TG-DSC in this work, Besikiotis et al. [2] reported −90 kJ/mol for the same material and method. However, they used a much lower p_{H_2O} = 0.025 atm, yielding lower changes in sample mass and heat flow upon hydration, i.e. larger uncertainties than in our current study. The hydration enthalpy of −80 kJ/mol obtained by Besikiotis et al. [2] by curve fitting of water uptake from TG is disregarded here because they assumed full hydration contrary to our observation of limited and variable maximum hydration, to be discussed in the next section.

The standard entropies of hydration extracted from fitting water uptake average at approximately −150 J/mol K, and are within the range of entropies typically found for hydration of oxides (−120 ± 40 J/mol K) [5].

In addressing the deviation between the hydration enthalpies determined directly by TG-DSC and by curve-fitting presented in Table 1, it is first important to recognize the major differences in the derivation of the two sets of thermodynamic data. The TG-DSC measurements directly reflect the enthalpies associated with the overall process in the materials when exchanging the surrounding atmosphere from dry to wet gas, whereas the TG data relies on curve fitting, carrying assumptions of a defect model representing hydration and with potentially correlated fitting parameters. However, fitting TG data as a function of temperature may serve to determine first approximated values of the saturation level for the different compositions. All in all, the standard molar hydration thermodynamic parameters take on rather consistent and reasonable values. Hence, the major parameter of interest remains the small and variable hydration limit, which we shall discuss further in the following.

3.2. Limited hydration of the heavily doped disordered fluorites – a new model

The fitted maximum levels for water uptake are far from the theoretical limit of 1 mol/mol $Ln_2Ce_2O_7$, indicating that the water uptake is thermodynamically limited to lower values, suggested from the experimental results to be around 0.2 (20%) in the case of $La_2Ce_2O_7$. Is there a way we can plausibly rationalize such a low maximum hydration of the nominally available oxygen vacancies in the disordered heavily doped, or oxygen deficient, fluorite structure as found in $La_2Ce_2O_7$?

Some defect interactions are perceivable in the investigated compositions, such as acceptor-vacancy association [1,20–22] and local vacancy-vacancy association due to high vacancy concentrations, as found in reduced ceria [23]. Depending on the strength of the association, the oxides could have oxygen vacancies with varying hydration affinities, determined by their local environment. Vacancies with endothermic hydration enthalpies will as such not hydrate and therefore lower the observed saturation level. Partial long-range order is found in the Nd-containing samples [17] and the oxygen ordering is, as we will discuss later, likely to stabilize the vacancies enough to efficiently inhibit hydration, but for now we will concentrate on the disordered fluorite structured $La_2Ce_2O_7$ (and the disordered fractions of the Nd-containing samples).

In a first approach, the limited hydration may be attempted rationalized by assigning a fraction of the vacancies to lower energies, i.e., that they are trapped in certain configurations of cations. If we assume that the structure is a disordered fluorite, both the oxygen and the cation sites are disordered, and each cation is on average 7-fold coordinated with oxygen, meanwhile each oxygen site is coordinated by four cations. Statistical analysis shows that an oxide with equal amounts of La^{3+} and Ce^{4+} like in $La_2Ce_2O_7$ ($x = 0$) has 16 different configurations of cations around each tetrahedrally coordinated oxide ion: The number of these configurations with 0, 1, 2, 3, and 4 La^{3+} ions is, respectively, 1, 4, 6, 4, and 1, summing up to 16. Of these, 2 are statistically vacant in $La_2Ce_2O_7$ (or $La_4Ce_4O_{14}$).

In this framework there is no way to assign any of these configurations with energetics for oxygen vacancies that give as limited hydration as observed. If we, for example, assume that one of the "end members" with either 4 La or 4 Ce coordinating the oxygen site trap oxygen vacancies strongly, this still leaves another vacancy available for hydration, corresponding to as much as 50% of the nominal amount – more than twice the experimental indication. If more of the 16 configurations trap oxygen vacancies, both vacancies will be trapped. If the trapping enthalpy is larger than the hydration enthalpy, they will remain unavailable for hydration and there will be no hydration. If the enthalpy is comparable or smaller, the hydration will however proceed and "unlock" the vacancies as temperature decreases or pH_2O increases, and the material will eventually hydrate fully.

Let us instead assume that one configuration – again one of the "end members" – has a favourably low energy for protons, i.e. acts as a strong trap for protons. Then hydration is limited to one proton per 16 oxide ion sites, which corresponds to one half water molecule – or half an oxygen vacancy filled. This is 25% of the 2 vacancies nominally available, which is strikingly close to the experimental indication of around 20%. A plausible "end member" site for these trapped protons is the oxygen site coordinated by 4 La^{3+} ions. While oxygen vacancies might have a slight preference for Ce^{4+} coordination or, vice versa, Ce^{4+} prefers oxygen vacancies because its small size favours low coordination numbers, the protonic defect may well neglect this aspect and instead be strongly attracted to the site surrounded by four of the basic lower valent La^{3+}.

We next show that the experimental water uptake of $La_2Ce_2O_7$ (or 50% La doped CeO_2) at pH_2O = 1 atm is well explained by the new model using rational parameters. It is herein assumed that all oxygen vacancies are free and unassociated with each other or any cation

configuration. Moreover, all hydration reactions are assigned a fitted standard entropy change of −108 J/mol K, well within what is normally found for reactions with loss of one molecule of gas, and hydration reactions in particular. In a first approach the hydration reaction is assigned a standard hydration enthalpy change of 0 for all oxygen sites except the 1 out of 16 which is assigned −64 kJ/mol of H_2O to fit the experimental data. This would mean that undoped CeO_2 is indifferent to hydration, but that the fully La-coordinated oxide ion traps protons with an enthalpy of −32 kJ/mol per proton. The model may hence equally well be represented by a general unfavourable hydration for the entire oxide, but with a proton trapping reaction to the La-coordinated site.

Indeed, CeO_2 is as such known not to hydrate, and DFT calculations have accordingly yielded a positive standard enthalpy of hydration for CeO_2 of +66 kJ/mol of H_2O [6]. If we take this enthalpy into the model for hydration of all sites except the fully La-coordinated one, we need a relatively more negative one for the fully La-coordinated one, i.e. a stronger trapping enthalpy now of the order of −70 kJ/mol per proton, to fit the experimental data. This is indeed in accordance with our preliminary ab initio DFT-calculations where we find an enthalpy difference of −70 kJ/mol for a proton on an oxide ion coordinated by 4 La^{3+} ions compared with 4 Ce^{4+} ions in a disordered fluorite $La_2Ce_2O_7$ lattice.

One may note that in the hydration reactions in the model applied, it does not matter which oxide ion site is filled with oxygen (the 4 La^{3+} coordinated one or any of the other ones) since they are per definition equal in this respect – it only matters where the protons end up.

The new model – whether it takes a CeO_2 with zero or positive hydration enthalpy as starting point – accounts for the main part of the modelled hydration, fitting qualitatively the measured hydration curve as well as the approach to the saturation level, as shown in Fig. 4. The upward tail at high temperatures is uncertain due to small hydration levels, but may reflect intermediate trapping energies for the less La-coordinated sites. The curve in Fig. 4 is indeed fitted with such a value for the 2 out of 16 sites with 1 Ce^{4+} + 3 La^{3+} coordination, yielding the hydration tail at higher temperatures due to the more favourable configurational entropy of 2 vs 1 out of 16 sites (see Fig. 4 caption for the exact parameters used in the modelled curve).

We note the qualitative agreement between the standard enthalpies of hydration of the order of approximately −64 kJ/mol of H_2O obtained here with the new model assuming zero hydration of CeO_2 and the −77 kJ/mol of H_2O obtained for $La_2Ce_2O_7$ by TG-DSC, as both represent apparent effective hydration of the material with limited saturation levels. However, as clear from the above, the knowledge of the endothermic hydration enthalpy of CeO_2 as such allows a more correct assessment of the enthalpies involved in the hydration (trapping of protons) to the dominating 4 La^{3+} site.

The trapping energy between a proton and an oxide ion coordinated by 4 Nd^{3+} is expected to be lower than for 4 La^{3+}, since the basicity of La is larger. This may explain the gradually decreasing negative apparent hydration enthalpy with increasing Nd-content from the TG-DSC results in this study (Table 1).

The present model points at a possibility that may have been overlooked in earlier works: The statistical variations of coordination around oxygen sites in a heavily doped oxide create a limited number of oxide ions with special properties, such as being so favourable sites for protons that an otherwise non-hydratable oxide displays a certain hydration. Applied to $La_2Ce_2O_7$ it means that 1/16 of the oxide ions may have this property and makes the material hydrate to 25% of the nominal acceptor (and oxygen vacancy) contents. It is interesting to note that the same principle then would be in effect also for less doped systems, but the resulting concentration of specially coordinated oxygen sites to be protonated would be drastically reduced. For instance, 1 and 10 mol% La-doped CeO_2 would have only $1 \cdot 10^{-8}$ and $1 \cdot 10^{-4}$ of the oxygen sites coordinated by 4 La^{3+} ions, resulting in the same numbers of H_2O per mole of CeO_2, in turn representing hydration of merely 2 ppm and 0.2% of the oxygen vacancies, which would easily pass unnoticed.

In general, the degree of hydration F_{hydr} from a complete coordination of an acceptor cation Acc in an oxide MO_b where the oxide ions are coordinated by a number C of cations M is according to our simple considerations expressed as

$$F_{hydr} = \frac{[H_2O]}{[v_O^{\bullet\bullet}]} = \frac{\frac{[OH_O^{\bullet}]}{2}}{[v_O^{\bullet\bullet}]} = \frac{\frac{[O_{coord}]}{2}}{[v_O^{\bullet\bullet}]} = \frac{\frac{bX_{O_{coord}}}{2}}{[v_O^{\bullet\bullet}]} = \frac{\frac{b[Acc_M^{/}]^C}{2}}{\frac{[Acc_M^{/}]}{2}} = \frac{b[Acc_M^{/}]^C}{[Acc_M^{/}]} = b[Acc_M^{/}]^{C-1} \quad (6)$$

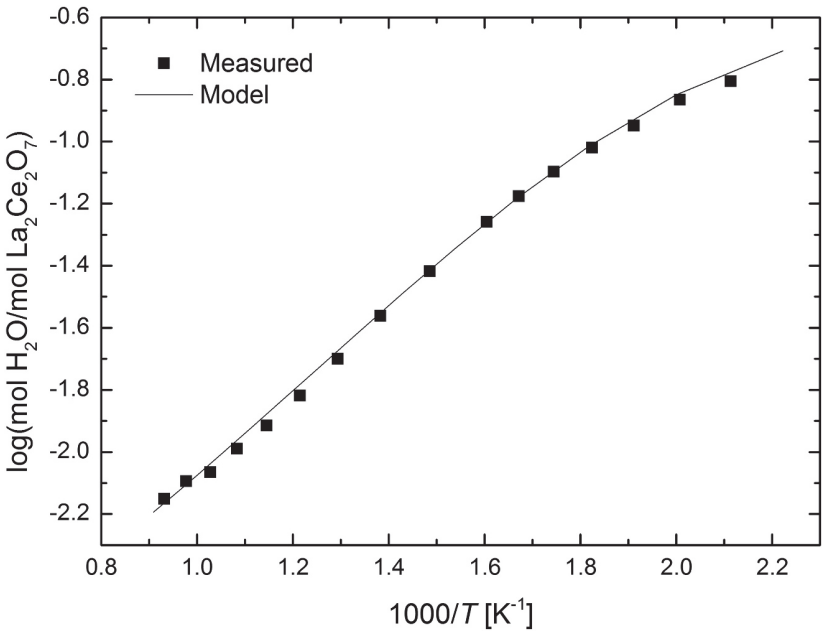

Fig. 4. Measured water uptake in $La_2Ce_2O_7$ vs 1000/T compared with modelled values, explained in the text, using standard entropy and enthalpy of hydration of, respectively, −108 J/mol K and +66 kJ/mol of H_2O, and trapping enthalpies of protons to the 1/16 sites coordinated by 4 La^{3+} and 2/16 sites coordinated by 1 Ce^{4+} + 3 La^{3+} of, respectively −65 and − 47 kJ/mol of protons.

where square parentheses denote molar fraction and X denotes site fraction. The number 2 emerges simply from electroneutrality and valence considerations of protons vs oxide ions. For fluorite oxides MO_2, $b = 2$ and $C = 4$, yielding the numbers calculated above. For perovskites AMO_3 doped on the M-site, $b = 3$ and $C = 2$. For instance, 10% doping of a very basic acceptor on the M-site of a perovskite with otherwise unfavourable hydration thermodynamics could be hydrated to 30% of the nominal level. This big effect for perovskites stems from the oxygen coordination C being as low as 2 in this case, and reminds us that the expression fails for cases predicting $F_{hydr} > 1$, which would be at > 33% acceptor doping for perovskites. Real cases of oxides with more favourable hydration thermodynamics will obviously reflect protonation of oxide ions of various coordination, yielding intermediate full hydration levels and apparent thermodynamic parameters.

Concluding this part we repeat the argument that stabilization of protons on oxide ions largely coordinated to basic acceptor dopants yields the dominating energy that enables hydration in the disordered fluorite, while it at the same time then may limit the amount of hydration well below the nominal one expected from the acceptor doping level.

3.3. Effect of vacancy ordering on hydration

Fig. 5 shows the actual water uptake as a function of x in $La_{2-x}Nd_xCe_2O_7$ for different temperatures (connected symbols) and the estimated maximum uptake - saturation values – from fitting the water uptake (dashed line) according to the standard hydration model for a variable content of effective acceptors and free vacancies. The actual as well as the maximum water uptakes are decreasing considerably with increasing x. We will here explore this in terms of the effect of long-range vacancy order.

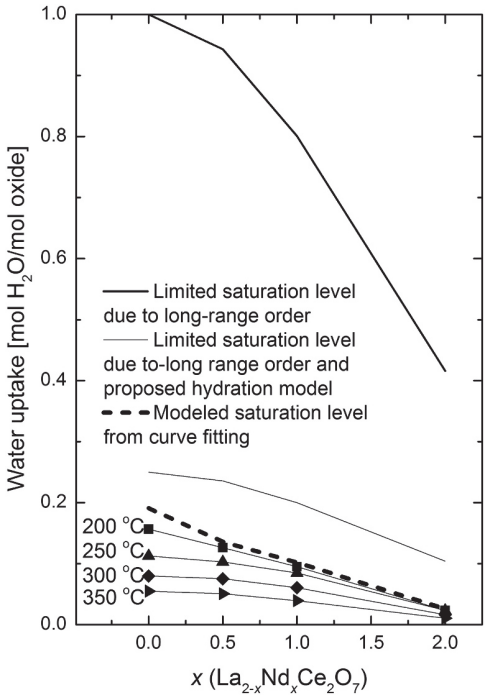

Fig. 5. The water uptake at 1 atm H_2O measured at different temperatures as function of composition ($La_{2-x}Nd_xCe_2O_7$ x = 0, 0.5, 1 and 2) as well as the estimated saturation level according to the degree of long-range order (thick solid line) and estimated saturation level based on the proposed models for limitations of hydration on both the disordered and ordered fractions (thin solid line) and the saturation level obtained by curve fitting of the water uptake data (dashed line).

In addition to the aforementioned local association forces between protons and La/Nd, we also have to consider long-range order in this compositional series. Our previous work on these compositions shows that $La_2Ce_2O_7$ is best described by the defect fluorite structure where the cations and oxygen vacancies are disordered [17]. The other end member, $Nd_2Ce_2O_7$, was shown to adopt a C-type structure with oxygen excess for more than 50% of the volume, while the other half adopted a defect fluorite structure [17]. Thus, there is an increasing tendency for partial long-range vacancy order as the Nd-content increases. The structural relaxation stabilizing the whole lattice during ordering effectively stabilizes the vacancies, making them harder, or impossible, to hydrate. This can therefore explain a further decrease in the observed water uptake and saturation level with increasing Nd-content in the composition, in correspondence with the measured TG data (cf. Fig. 5).

Based on this we rationalize the observed trends, for the sake of simplicity and illustration, by dividing the matrix of each composition containing Nd, into two parts;

1) a part of the volume having a disordered lattice only offering a fraction of hydration due to different local environments of host and acceptor dopant cations, as discussed above, and
2) a remaining part having a dominant long-range order between vacancies inhibiting both mobility and hydration.

The amount of the latter type of lattice increases with Nd content. We have used input from the structural investigations and estimated the relative amount of long-range order across the material series. By subtracting the amount of oxide related to the observed long-range order, we obtain an estimate of the remaining part of the oxide which is available for hydration, represented by the top thick black line in Fig. 5. Now assuming that only 25% of these free vacancies hydrate under the present conditions, we have calculated how the saturation level is expected to change across the $La_{2-x}Nd_xCe_2O_7$ series. We used $La_2Ce_2O_7$ ($x = 0$) as the starting point, where no long-range order has been observed, with a hydration saturation level of 0.25, and the estimated hydration level decreases as x and long-range order evolve (included in Fig. 5 as the thin black line). Although this does not reproduce the fitted saturation levels (dashed lines) completely, it qualitatively corresponds with the overall trend in the behaviour of the experimental data. The fact that the apparent level of saturation decreases with increasing Nd content is in line with this simple estimation, including both of the proposed models for limitations in the disordered and the ordered fractions of the sample.

The discrepancy between the estimated saturation level resulting from the combined model of long-range vacancy order and short range proton trapping (thin black line) and the saturation estimated from our measurements can be explained by additional locking of vacancies due to local vacancy association of the same type as giving long-range order. Such vacancy association occurs as pairs or clusters even in $La_2Ce_2O_7$ to some small degree, but will not be observed by diffraction (see previous work for elaboration [17]).

3.4. Correlations with electrical conductivity

The conductivity of all the samples, except $La_2Ce_2O_7$, increases with pO_2 in oxidizing atmospheres, more pronounced with increasing Nd content. This reflects p-type electronic conductivity from minority electron holes, which generally speaking can be ascribed to the slight tendency of Nd^{3+} to be oxidized to Nd^{4+}, evidenced also in previous work on $Nd_2Ce_2O_7$ [15]. Studies of oxide ion and protonic conductivity are hence done in Ar atmospheres, where the p-type conductivity is negligible.

Fig. 6 (left) shows the conductivity vs pH_2O for water levels up to ~2.5%. The conductivity increases with increasing water vapour and the effect increases with decreasing temperature, according to the exothermic hydration enthalpy. Moreover, the effects of water vapour

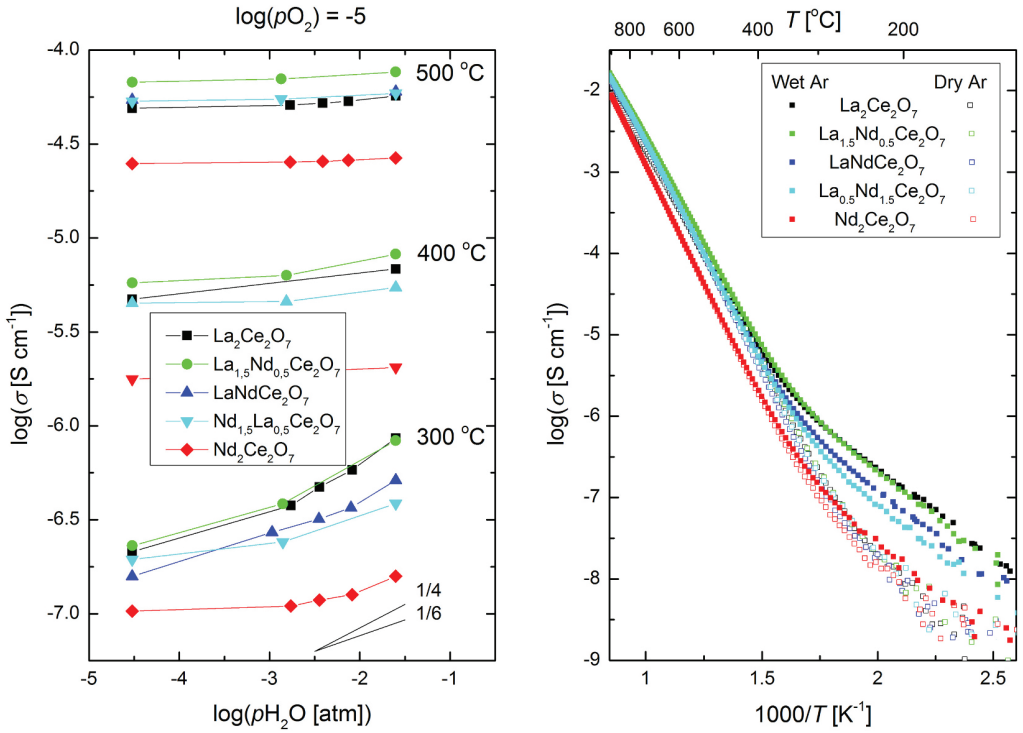

Fig. 6. Left: Isothermal conductivities in Argon with increasing pH_2O. Right: Isobaric conductivities in wet and dry Argon.

are stronger for the La-rich compositions. These observations are supporting the above discussion. Notably, the dependencies never reach neither the expected $pH_2O^{1/2}$ dependencies nor saturation, as the water vapour pressures are two orders of magnitude lower than the 1 atm used in the TG-DSC measurements and the temperatures are well higher than the saturation range.

Fig. 6 (right) shows the temperature dependencies in wet Ar. At high temperatures oxide ion conductivity predominates with apparent activation energies for $La_2Ce_2O_7$ increasing from 95 kJ/mol at the highest temperatures to around 103 kJ/mol at intermediate temperatures. This slightly non-linear Arrhenius-like behaviour may reflect a small tendency of association or local order. With increasing Nd contents, the activation energy increases further, to around 116 kJ/mol for $Nd_2Ce_2O_7$, in line with the increasing oxygen vacancy ordering.

At low temperatures the protonic contribution becomes dominating, in agreement with previous work [2,14,15]. Fitting the straight portions yields activation energies for proton conductivity increasing monotonously from around 43 kJ/mol for $La_2Ce_2O_7$ to around 50 kJ/mol for $Nd_2Ce_2O_7$. Assuming equilibrium in the minor proton concentration given by the trapping to specific sites, and that the mobility of protons is limited by untrapping and by free proton migration between traps, the effects of trapping on conductivity cancel, and the observed enthalpy will reflect only jumps of free untrapped protons, hence being 43 kJ/mol in $La_2Ce_2O_7$ and 50 kJ/mol in $Nd_2Ce_2O_7$ based on our measurements. The activation energies for conductivity and hence mobility of untrapped protons this way come out as roughly half that for oxygen vacancies in these materials.

4. Conclusions

The system $La_{2-x}Nd_xCe_2O_7$ (x = 0, 0.5, 1 and 2) displays a cubic disordered structure corresponding to 50% La-doped CeO_2 for $La_2Ce_2O_7$ (x = 0) and with more oxygen vacancy ordering as x increases [17]. $La_2Ce_2O_7$, or 50% La-doped CeO_2, hydrates, despite the fact that the moderately acceptor doped parent oxide CeO_2 does not. The hydration decreases with increasing Nd content x.

The amount and enthalpy of hydration of $La_{2-x}Nd_xCe_2O_7$ (x = 0, 0.5, 1 and 2) have been measured using TG-DSC. The observed hydration is far from the theoretical limit corresponding to 50 mol% acceptor doped ceria. We suggest herein a new model in which the statistical variation of coordination around oxygen sites in a heavily doped fluorite oxide creates a limited number of oxide ion sites that favour incorporation of a proton. If for instance only the one oxygen site coordinated by 4 La^{3+} ions in $La_2Ce_2O_7$ is protonated, this corresponds to hydration of only ¼ (25%) of the oxygen vacancies, close to the experimentally observed saturation limit. The hydration enthalpies for $La_{2-x}Nd_xCe_2O_7$ are found to be in the range − 77 to −71 kJ/mol based on the TG-DSC data, becoming slightly less exothermic with increasing Nd-content. The fitting of the TG data to a model of protonation of only statistically fully La^{3+} coordinated oxygen sites yields a proton bonding energy to this site of around −32 kJ/mol (corresponding to a hydration enthalpy for this site of −64 kJ/mol) for $La_2Ce_2O_7$ if the we assume a hydration enthalpy equal to 0 for the host compound CeO_2 otherwise. However, if we assume that CeO_2 has an unfavourably endothermic enthalpy of hydration (e.g. +66 kJ/mol H_2O based on DFT), a correspondingly stronger trapping of protons to the 4 La^{3+} coordinated oxide ion is required to fit the experimental data, e.g. close to −70 kJ/mol per proton.

Less La^{3+} coordinated oxide ions may have intermediate proton trapping energies, as indicated by our data also. The new model may be generally applicable to hydration of other heavily doped oxides with otherwise unfavourable hydration, and explain cases of hydration far from the nominal.

The proton conductivity exhibits an activation energy of 43 kJ/mol

for $La_2Ce_2O_7$ increasing to 50 kJ/mol for $Nd_2Ce_2O_7$ under conditions with minority proton concentrations, which then corresponds to the activation energy for mobility of free untrapped protons.

The observed decrease in water uptake with increasing Nd content x is interpreted to reflect an increasing tendency to long-range order that inhibits hydration of an increasing fraction of the vacancies.

Credit author statement

Liv-Elisif Kalland: Conceptualization, Methodology, Formal Analysis, Investigation, Writing - Original Draft, Writing –Review & Editing

Andreas Løken: Methodology, Formal Analysis, Writing – Review & Editing

Tor Bjørheim: Methodology, Formal Analysis, Writing – Review & Editing

Reidar Haugsrud: Conceptualization, Writing – Review & Editing, Supervision

Truls Norby: Conceptualization, Methodology, Writing - Original Draft (minor parts), Writing – Review & Editing, Supervision.

Declaration of competing interest

The authors declare that they have no known competing financial interests or personal relationships that could have appeared to influence the work reported in this paper.

Acknowledgements

The computations were performed on resources provided by UNINETT Sigma2 – the National Infrastructure for High Performance Computing and Data Storage in Norway.

References

[1] D.Y. Wang, D.S. Park, J. Griffith, A.S. Nowick, Solid State Ionics 2 (2) (1981) 95.
[2] V. Besikiotis, C.S. Knee, I. Ahmed, R. Haugsrud, T. Norby, Solid State Ionics 228 (2012) 1.
[3] T. Hagiwara, Z. Kyo, A. Manabe, H. Yamamura, K. Nomura, J. Ceram, Soc. Jpn. 117 (Dec.) (2009) 1306.
[4] T.S. Bjørheim, A. Løken, R. Haugsrud, J. Mater. Chem. A 4 (16) (2016) 5917.
[5] T. Norby, M. Wideroe, R. Gloeckner, Y. Larring, Dalton Trans. (2004) 3012.
[6] T. Zacherle, A. Schriever, R.A. De Souza, M. Martin, Phys. Rev. B 87 (13) (2013) 134104.
[7] R. Haugsrud, Y. Larring, T. Norby, Solid State Ionics 176 (39–40) (2005) 2957.
[8] Y. Larring, T. Norby, Solid State Ionics 97 (1–4) (1997) 523.
[9] T.S. Bjørheim, V. Besikiotis, R. Haugsrud, Dalton Trans. 41 (43) (2012) 13343.
[10] K.D. Kreuer, Annu. Rev. Mater. Res. 33 (2003) 333.
[11] C. Kjølseth, L.-Y. Wang, R. Haugsrud, T. Norby, Solid State Ionics 181 (39) (2010) 1740.
[12] J. Faber, C. Geoffroy, A. Roux, A. Sylvestre, P. Abélard, Appl. Phys. A Solids Surf. 49 (3) (1989) 225.
[13] H. Yahiro, Y. Eguchi, K. Eguchi, H. Arai, J. Appl. Electrochem. 18 (4) (1988) 527.
[14] W. Sun, S. Fang, L. Yan, W. Liu, Fuel Cells 12 (3) (2012) 457.
[15] S. Cheng. Master thesis, Department of Physics, University of Oslo, Oslo (2012).
[16] Z.G. Liu, J.H. Ouyang, K.N. Sun, Fuel Cells 11 (2) (2011) 153.
[17] L.-E. Kalland, S.T. Norberg, J. Kyrklund, S. Hull, S.G. Eriksson, T. Norby, C.E. Mohn, C.S. Knee, Phys. Chem. Chem. Phys. 18 (34) (2016) 24070.
[18] A. Løken, T.S. Bjørheim, R. Haugsrud, J. Mater. Chem. A 3 (46) (2015) 23289.
[19] K.D. Kreuer, S. Adams, W. Münch, A. Fuchs, U. Klock, J. Maier, Solid State Ionics 145 (1) (2001) 295.
[20] V. Butler, C.R.A. Catlow, B.E.F. Fender, J.H. Harding, Solid State Ionics 8 (2) (1983) 109.
[21] L. Minervini, M.O. Zacate, R.W. Grimes, Solid State Ionics 116 (3–4) (1999) 339.
[22] R. Gerhardt-Anderson, A.S. Nowick, Solid State Ionics 5 (1981) 547.
[23] S. Hull, S.T. Norberg, I. Ahmed, S.G. Eriksson, D. Marrocchelli, P.A. Madden, J. Solid State Chem. 182 (10) (2009) 2815.

5 Discussion

"Research is to see what everybody else has seen, and to think what nobody else has thought."

– Albert Szent-Györgyi

$La_{28-x}W_{4+x}O_{54+\delta}$ and $La_{2-x}Nd_xCe_2O_7$ crystallize in cubic, fluorite derived structures and are highly oxygen deficient with respect to the perfect fluorite. The nature and degree of oxygen vacancy ordering is intimately connected to the vacancy related materials properties. The size, valence and electronegativity of ions, together with the crystal structure, define the bond length between cations and anions, and the resulting size of the fluorite derived unit cell. The bond length also indicates the effective basicity of the cations (or cat-O complexes) which play an important role for the conductivity and hydration of the oxides. The aim in this discussion is to identify trends that describe and explain the change in defect related properties, correlated to oxygen vacancy ordering, as well as cation-oxygen bond lengths.

In the discussion and summarizing conclusions, we will refer to the $La_{2-x}Nd_xCe_2O_7$ series studied in Papers I-III without including (x = 0, 0.5, 1, 1.5 and 2). For discussion of general properties and trends for compounds containing also other lanthanide cations (Ln) we sometimes use $Ln_2Ce_2O_7$. LaWO will be used as a general expression for $La_{28-x}W_{4+x}O_{54+\delta}$ compositions within the range of stable ratios of La/W 5.3-5.7 [30, 90, 91], and we further include the La/W ratio when referring to a compound with specific stoichiometries (e.g. LaWO54 for the La/W ratio of 5.4). The term vacancy will refer to an oxygen vacancy unless stated otherwise.

5.1 Structure, defects and ordering in oxygen deficient fluorite oxides

The diffraction studies do not provide a perfect crystal structure, and none of these compounds is therefore completely ordered. The average structure obtained from Rietveld refinements - containing partial occupancy, and displacement factors - cannot determine all details of the local structure. Thus, *the compounds cannot be described fully by means of average structure models* when the goal is to understand their conductivity and hydration

properties. It is important to understand the local oxygen environment to be able to define the defect chemistry and reactions occurring. Therefore, we use computational modelling of the structure and compare with diffraction results to look at possible local structures in the materials that are consistent with the average structure models. We will in this section investigate how local structure of LaWO and $La_{2-x}Nd_xCe_2O_7$ influences the materials properties such as oxide ion conductivity and hydration which depend on oxygen vacancies.

In the LaWO-compositions studied, we find that the local oxygen structure differs strongly around W and La due to the large difference in cation size and electronegativity. Although all oxide ions are positioned close to the original fluorite oxygen positions (i.e. at the 8c Wyckoff position of the space group Fm-3m), W forms strongly bonded and regular WO_6 octahedra, contrary to La which has a distorted cubic coordination of oxides with coordination number between 6 and 8. In $La_{2-x}Nd_xCe_2O_7$, the cations are more similar in size and electronegativity, and the oxygen structure around the cations are almost identical, but with a varying degree of long range ordering of the vacancies. There are several similarities in the crystal structure of LaWO and $La_{2-x}Nd_xCe_2O_7$, but also important differences in their local structure. By comparing these, we find trends in the coordination polyhedra of cations and local vacancy ordering related to the size of the cations, and ratio of electronegativity or size between the cations, in the structure.

The compounds studied can also be viewed as doped systems, e.g. $Ln_2Ce_2O_7$ (Ln = La and/or Nd) could be written as $Ce_{1-x}Ln_xO_{2-0.5*x}$ and LaWO as $La_{28-x}W_{4+x}O_{54+3/2*x}$ [91]. These oxides have large amounts of vacant oxygen sites corresponding to 12.5% empty sites relative to the perfect fluorite structure (8c Wyckoff position of space group Fm-3m) for $Ln_2Ce_2O_7$ and LaWO has even more vacant sites. In both materials classes, the relatively high concentration of vacancies is far from the dilute limit, and interactions between them must be expected. For LaWO, the majority of the vacant sites are not considered as charged vacancies, since they are part of a strong local order around W.

Local structure and oxygen defects in LaWO

The average defective fluorite structure previously determined for LaWO with only one partially occupied oxygen position [30] does not describe the local oxygen sublattice in a way consistent with the observed proton uptake [41]. Our GULP and DFT study of LaWO with excess W ([91] and Paper III), however, solved the apparent limitation on hydration: W ions always obtain octahedral oxygen coordination and the W-O bonds are shorter and more regular (i.e. more strong and more covalent) than the La-O bonds. Since only 6 out of 8 nominal oxygen positions coordinating each W cation are occupied in order to obtain 6-fold octahedral coordination, tungsten strongly “trap”, or lock, two vacancies. For $La_{28}W_4O_{54}$ (LaWO70), 54 of the 64 oxygen positions in the parent fluorite structure are occupied and

8 of the vacancies are trapped around the four W cations. The remaining 2 vacancies are disordered and available for hydration. The local nature of WO_6 is the basis of the defect nomenclature proposed by Erdal et al., which defines the site restrictions and allows us to describe the concentration of "free" and charged vacancies without additional aliovalent doping [41]. The strong preference of tungsten for a specific coordination thus limits the number of available or free vacancies, but it also dictates site restrictions that have to be followed when W is substituting La.

For lower and stable La/W ratios, we find in Paper IV that the additional W in LaWO54 substitute for La and act as donors by substituting for La located at the La2 site in the fluorite lattice (which is one of two La sites, La1 and La2). This structural model for the excess W has been further validated for LaWO56 [92]. As we now will see, the local oxygen structure around the cations in LaWO is also the key to explain the La/W ratio stability range. In LaWO54, one La2 substituted by W results in filling 1.5 vacant oxygen sites, leaving only half a vacancy available for hydration. The connectivity between the WO_6 and La_2O_x coordination complexes makes it possible to substitute one La2 with W because the resulting two WO_6 octahedra will be sharing the 2 «trapped» vacancies. In this way, the average coordination number of La increases while W keeps its preferred octahedral coordination. Any further W substitution of La is restricted due to the lack of vacant oxygen positions available to be filled with new oxide ions. The instability of additional W substitution is encountered experimentally by the observed phase segregation when La/W < 5.3 [30]. These site restrictions make substitution of the La1 position with W unfavourable since La1 does not have any connectivity to W. The resulting configuration is forced to incorporate some oxygen in interstitial positions, consequently yielding a heavily distorted oxygen structure locally. The material is also not stable when La/W > 5.7 [30] supporting the idea that the stoichiometry of $La_{28}W_4O_{54}$ results in an unfavourably high vacancy concentration, since it results in heavy under-coordination of La. The effective coordination number of La becomes lower due to the strong W-O bonds to the oxygen shared with La2, making La2 even more vulnerable to under-coordination. This shows how the nature of the W-O bonds and W coordination number, explain the stability range of LaWO.

Partial C-type diffraction peaks due to ordered domains in $La_{2-x}Nd_xCe_2O_7$

NPD and XRD of the $La_{2-x}Nd_xCe_2O_7$ series give distinct Bragg peaks corresponding to the simpler fluorite structure but there are super lattice reflections in the Nd containing samples which indicates some long range order not captured in the simple fluorite structure. The additional diffuse and broadened Bragg peaks, however, have low intensity and correspond to only some of the peaks found in the C-type structure of RE_2O_3. They became more intense and sharper with increasing Nd-content in $La_{2-x}Nd_xCe_2O_7$. Rietveld refinements show that a combination of the disordered oxygen deficient fluorite structure and an oxygen excess

C-type structure is a good average model for the Nd containing samples of $La_{2-x}Nd_xCe_2O_7$. 50% statistical occupation of the 16c site of space group *Ia*-3 for the fraction fitted to the C-type structure, suggests that the partial long range ordering within the fluorite structure is related to the oxygen positions in this structure.

The most probable source of the super lattice diffraction peaks is formation of domains with long range ordering of vacancies and size effects from the domains could then explain the broadened superlattice reflections. To investigate this further, we looked for domains with vacancy order in the $La_{2-x}Nd_xCe_2O_7$ samples using HR-TEM, inspired by the work of Withers et al. [57]. Compared to the simple fluorite structure the electron diffraction patterns revealed extra satellite reflections as seen in the inset of Figure 5. The satellites around the 220 diffraction spot indicate the presence of domains as previously shown for $Ce_{1-x}Y_xO_{2-0.5x}$ (x = ~0.5) by Withers et al. [57]. Figure 5 shows dark field (DF) images obtained from two regions along the edge of a crystal oriented close to the [-111] zone axis. The main reflection 220 (consistent with both disordered fluorite structure and C-type supercell structure as 220 and 440 respectively), has high intensity and it is hard to distinguish any features within the corresponding dark field image. However, both the satellites (indexed as 220 + 0 ½ ½ and 220 + -½ 0 ½ with respect to a simple fluorite cell) show clear intensity variations within their dark field discs as seen in Figure 5. This is a clear indication of domains with sizes of a few 10ths of nm and, hence, the presence of nanodomains.

Nanodomains with distorted fluorite structure have similarly been identified in La and Sm doped ceria by HR-TEM [93]. These nanodomains most likely contain C-type related vacancy order but not the C-type structure itself, which has a different stoichiometry, namely RE_2O_3. The nature of the C-type related vacancy ordering is thoroughly discussed based on DFT calculations in Paper II, and will be further addressed in the next section.

C-type related vacancy ordering has also been proposed for LaWO57 as a possible origin of diffuse scattering indicative of long range ordering [91]. The amount of vacancies increases with increasing La/W ratio in LaWO, which can lead to more vacancy ordering. This is further supported by the observation of superstructures with HR-TEM in samples where the more reducible Mo substitute W, and is believed to stem from oxygen vacancies ordering as the amount increase upon increasing substitution [94].

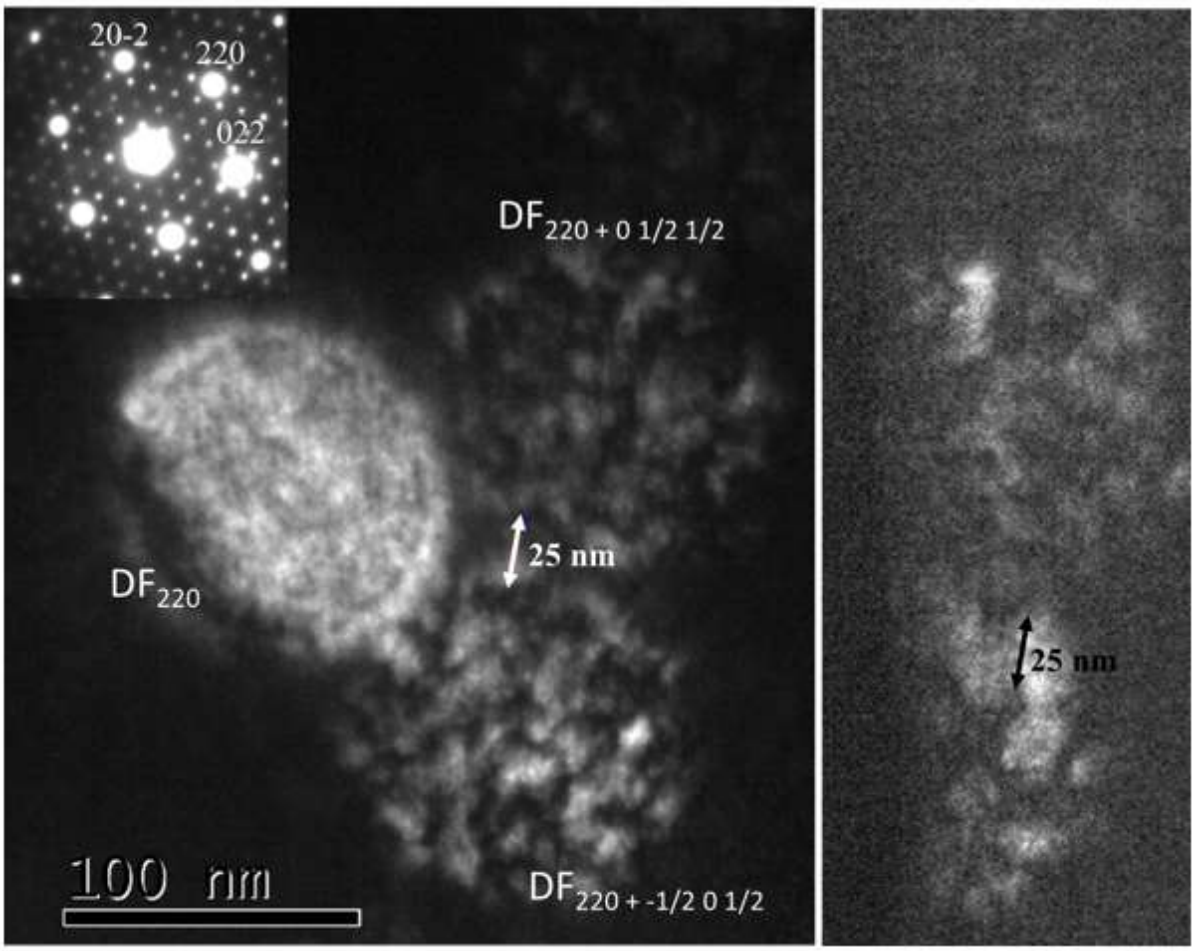

Figure 5 HR-TEM dark field images along the edge of a crystal oriented close to the [-111] zone axis of a $Nd_2Ce_2O_7$ sample, capturing the main 220 reflexion and two satellites (indexed as 220 + 0 ½ ½ and 220 + -½ 0 ½ with respect to a simple fluorite cell).

C-type related ordering, a new type of oxygen ordering in defective fluorites

The C-type related ordering found in Ln2Ce2O7 is built up by vacancy pairs that form more long range patterns. We refer the reader to the second page of Paper II where the definitions, terminology and illustration of these vacancy motifs are presented.

The vacancies in the C-type structure are basically aligned in a <110> and <111> manner in the primitive oxygen cubes representing a building block of the cubic fluorite lattice (see Fig. 1 in Paper II where this cube is shown). We also find a clear preference of these alignments, especially the <110> motif, in $La_2Ce_2O_7$ and $Nd_2Ce_2O_7$, but the "longer" <210> vacancy alignment is actually more favoured over the <110> motif, and more so for $Nd_2Ce_2O_7$ than $La_2Ce_2O_7$. A higher number of <210> alignments in the oxygen configuration is correlated with lower energy. The highest number is obtained when <210> vacancies "connect" the shorter <110> and <111> alignments into an ordered pattern in the

same manner as for the C-type structure (see Fig. 2 in Paper II). There are some small differences in the nature of the local ordering between $La_2Ce_2O_7$ and $Nd_2Ce_2O_7$ which is correlated to the cation radius and radius ratio rLn^{3+}/rCe^{4+} although both compounds have a preference for C-type related ordering according to our DFT results. In $La_2Ce_2O_7$ the shorter vacancy pairs, <110> and <111>, occur slightly more frequently during an MD run, which could be related to the observation of less long range order in $La_2Ce_2O_7$ than in $Nd_2Ce_2O_7$. Also, the oxygen sublattice of the lowest energy configuration in $La_2Ce_2O_7$ is only partly ordered in the C-type manner even though all vacancy pairs are aligned in favourable <110>, <111> and <210> configurations. Since the cations in this configuration are ordered in the pyrochlore manner, the effect of the size difference between the two cations seems to be emphasized resulting in the smaller Ce^{4+} being coordinated in octahedrons (<111> vacancy alignment) more frequently than when the cations are organized in other ordered or disordered configurations. This illustrates that $La_2Ce_2O_7$ is closer to, but still far from, the pyrochlore stability range than $Nd_2Ce_2O_7$, according to the prediction model from Minervini et al. [28], which states that the cation radius ratio, rA^{3+}/rB^{4+}, of a $A_2B_2O_7$ pyrochlore must be above 1.4 in order to form a stable pyrochlore structured oxide.

Configurations where all vacancies are ordered in the C-type related manner are more favourable than the random oxygen configurations, independent of the cation arrangements. This indicates that the vacancy ordering is not driven by strong differences in size and electronegativity between the cation types contrary to the cation-anion ordering in the pyrochlore and perovskite structures. In $La_2Ce_2O_7$ and $Nd_2Ce_2O_7$ the cations are much more similar and comparable to the situation in C-type structured Ln_2O_3, where the oxygen ordering is the result of the densest and most symmetric ionic arrangement possible of Ln and O. This also takes into account the coordination based on stoichiometry. We find evidence that the reasons for long range ordering in $Ln_2Ce_2O_7$ could be similar.

When relaxing all cell parameters in $Nd_2Ce_2O_7$ during DFT optimizations the volume obtained for C-type related ordered configurations is slightly smaller than for disordered configurations, indicating that these ordering patterns allow for a better close packing and denser structure. The more disordered configurations thus have more free volume which enhances ionic conductivity, but gives a higher (less negative) lattice energy, making disorder less energetically favourable than long range order. When comparing $La_2Ce_2O_7$ and $Nd_2Ce_2O_7$, the latter has the smaller lattice constant due to the smaller cation size and shorter Cat-O bonds. Since we observe more long range vacancy ordering in $Nd_2Ce_2O_7$ than in $La_2Ce_2O_7$, we may speculate whether ordering - giving denser arrangements of the ions and vacancies - is more important for $Nd_2Ce_2O_7$ than for $La_2Ce_2O_7$ due to the smaller unit cell volume. The authors of a previous study of the disorder-order transition in the $NdO_{1.5}$-

CeO_2 system also suggest that the structural relaxation due to oxygen vacancy ordering could be facilitated by the similar ionic radii of the cations (i.e. Nd^{+3} more similar to Ce^{+4} than La^{+3}) and the decreasing unit cell volume with increasing Nd-content [23]. Another recent work also proposes a maximum value for the size mismatch in order to obtain C-type ordering intergrown with disordered fluorite structure [58].

Based on the local structure of the low energy oxygen configurations, we can identify some structural constraints we believe rationalize why ordering and higher symmetry give a decrease in the lattice energy. Some ordered oxygen configurations can ensure uniform distribution of vacancies in the lattice and similar average coordination number for the cations throughout the whole lattice, better than random configurations. The fact that the <100> vacancy alignments, which are not a part of the favourable vacancy ordering patterns, are highly unfavourable can be explained by electrostatic repulsion, but equally well by the fact that the highly distorted coordination sphere created by aligning the vacancies as nearest neighbours do not "enclose" the cation in a satisfactory way. Heavy under-coordination of cations is also unfavourable for both La/$Nd_2Ce_2O_7$ and LaWO, and large differences in coordination numbers creates heavily distorted coordination polyhedrons. These could induce additional strain in the lattice [95, 96], which is avoided when the vacancies are ordered with a fairly even distribution.

Although the local oxygen structure around the La cations in LaWO regarding vacancy alignments was not studied extensively in our computational work in Paper IV, it is interesting to revisit the DFT findings in the attempt to identify any similarities with $La_{2-x}Nd_xCe_2O_7$. When looking at low energy configurations for LaWO54, it becomes clear that the <100> configurations of vacancy pairs around the 6-fold coordinated La_2 are unfavourable, which is the same as found for $La_2Ce_2O_7$ and $Nd_2Ce_2O_7$. We further find some indications that the <110> alignments of vacancy pairs in a cube around La are found more frequently than <111> vacancy pairs. The volume of the polyhedron formed when the vacancies are aligned as third nearest neighbours, i.e. in the <111> pairs, seems to be smaller and with slightly shorter La-O bonds than when vacancies pairs are <110> aligned. Shorter La-O bonds could be considered favourable since heavy under coordination of La is not favourable. However, such a coordination polyhedron seems to give less flexibility and contributes to a less cubic lattice, as is also seen in $La_2Ce_2O_7$ and $Nd_2Ce_2O_7$. There could be similarities to $Ln_2Ce_2O_7$ also regarding long range order of vacancies in LaWO; C-type related ordering was also mentioned as a possible origin of diffuse scattering indicative of some type of oxygen vacancy ordering observed for a LaWO57 [91].

In reduced ceria and also in many complex fluorites containing trivalent rare earths, the most frequently observed short range vacancy ordering is the <111> alignment of vacancies around a cation resulting in an octahedral oxygen coordination around the cation [51, 54].

The C-type related ordering, which contains a high fraction of <110> and <210> vacancy alignments is thus a new structural model describing vacancy ordering in oxygen deficient fluorites which is different to what has previously been suggested for most oxygen deficient cubic fluorites (except C-type structured Ln_2O_3, itself). It is possible that local and long range order related to the C-type structure could be recognized in other complex fluorite structures where trivalent Lanthanides are one of the cation constituents.

Effect of cation size on local oxygen structure

From the optimised low energy configurations from DFT calculations, we see a trend in the local oxygen structure correlated to the ionic radii of the cations or more specifically the Cat-O bond length:

$$\text{La-O}_{\text{LaWO}} > \text{La-O}_{\text{LCO}} > \text{Nd-O}_{\text{NCO}} > \text{Ce-O}_{\text{NCO}} \sim \text{Ce-O}_{\text{LCO}} > \text{W-O}_{\text{LaWO}}$$
$$\xleftarrow[\text{Increasing bond length}]{}$$

The smallest cation W obtains more covalent strong bonds creating well defined local order, whereas the largest cation La, allows for more disorder in the surrounding oxygen lattice. The La-O bond is longer in LaWO than in $La_2Ce_2O_7$ due to the strong W-O bonds, pulling the oxygen away from La, thus stretching the La-O bonds. The local structure of oxygen around La in LaWO is, accordingly, more distorted and the oxide ions are generally displaced further away from the initial 16c oxygen positions (or refined as 16e for LaWO) than in $La_2Ce_2O_7$. When the ratio between the radii of the cations is increased, it emphasizes the effect on the local oxygen structure which has been correlated to the size, for both the smaller and larger cation. This is also seen in the difference between the coordination of Ce in $La_2Ce_2O_7$ and $Nd_2Ce_2O_7$, where the Ce^{4+} cation is more frequently octahedrally coordinated in $La_2Ce_2O_7$ than in $Nd_2Ce_2O_7$.

By correlating local vacancy order around a cation to its size we then find that <111> ordering of vacancies is preferred for the smaller cations with higher electronegativity, giving less polar and ionic bonds. The <111> vacancy alignments are found in heavily oxygen deficient ZrO_{2-x} and CeO_{2-x} as well as for the smaller cation in the pyrochlore structures. The C-type related vacancy ordering is seen in fluorite derived cubic structures where there are larger cations with low electronegativity, such as Lanthanides (seen that the cations have similar size if there are more than one type). All in all, we can conclude that local vacancy ordering around cations in cubic fluorites can be correlated to the cation size and electronegativity.

5.2 Energetics of ordering in $La_{2-x}Nd_xCe_2O_7$

In Paper II we find that the C-type related ordering of oxygen vacancies gives an enthalpy gain for both $La_2Ce_2O_7$ and $Nd_2Ce_2O_7$ compared to other types of ordered and randomly generated configurations. Long range order is only observed for the Nd containing samples of the $La_{2-x}Nd_xCe_2O_7$ series and such long range order is found in certain domains in the sample. These observations leave us with two questions that are yet not thoroughly answered: Why do we only observe partial long range ordering of vacancies if this type of ordering is energetically favourable? Why do we experimentally observe more disorder in $La_2Ce_2O_7$ than in $Nd_2Ce_2O_7$?

Entropy of disorder

We attempt to answer the first of these questions in Paper II by sketching out two possible explanations by comparing of the optimised energies for different configurations calculated using DFT. One possible explanation is that the two lowest energy configurations of $La_2Ce_2O_7$ have lower symmetry than those of the "Ctype1" configuration, thereby having a higher degeneracy and are thus representing a more disordered system. However, these low energy configurations have an ordered cation sublattice and we argue that ordered cation configurations are unlikely to exist in the characterized samples. Firstly, the structure analysis in Paper I using ND gives no evidence of cation order. Secondly, there is a strong possibility that the cation lattice of $La_2Ce_2O_7$ and $Nd_2Ce_2O_7$ contains frozen-in disorder at room temperature where the diffraction studies are performed. If we do not take cation ordered configurations into consideration, the energy difference between vacancy disordered and ordered configurations is lower for $La_2Ce_2O_7$ than for $Nd_2Ce_2O_7$. On the other hand, many vacancy disordered configurations are not thermally available if we only look at the enthalpies from DFT. This suggests that a comparison of enthalpies between the different configurations only, does not give us the complete explanation to what we observe experimentally. We also need to consider entropy contributions to the Gibbs energy.

The Gibbs energy (including also entropy) of the systems we observe experimentally is thus important and although further studies are required to determine exact values of entropy contributions to these structures, we still can make some assumptions.

Vibrational entropy could contribute differently to the Gibbs energy for the two compounds. In general when increasing the volume and bond lengths the vibrational entropy contribution to the free energy increases, comparing identical atomic arrangements. Both compounds will most likely be stabilized as disordered fluorites at sufficiently high temperatures. However, a larger vibrational entropy of $La_2Ce_2O_7$ due to its larger lattice constants could stabilize more disordered oxygen configurations to lower temperatures for $La_2Ce_2O_7$ than for $Nd_2Ce_2O_7$. That is the configurational and vibrational entropies couples.

In the MD calculations we indeed find that dynamic disorder contributes to a higher degree of oxygen disorder in $La_2Ce_2O_7$ than in $Nd_2Ce_2O_7$.

Since the more disordered compounds usually have a higher configurational entropy contribution than ordered ones, the enthalpy difference between ordered and disordered configurations is likely to be smaller than what is apparent solely from DFT results. There might be more ways to organize the vacancies locally for $La_2Ce_2O_7$ than explored in our small 88 ion cell in Paper II (i.e. the <111> vacancy pairs less unfavourable when coordinating Ce^{4+}). That is, there could be more configurations close in energy to the lowest energy configuration than we have found during our calculations. More configurations close in energy indicate higher configurational entropy and would indicate that $La_2Ce_2O_7$ is more disordered at lower temperature than $Nd_2Ce_2O_7$.

Since long range order is favourable only at sufficiently low temperatures, low mobility could result in frozen-in disorder, as thoroughly discussed in Paper II. The thermal history of $La_{2-x}Nd_xCe_2O_7$ samples is therefore crucial for the degree of ordering present at low temperatures. Thermal history is also important for the LaWO system where higher oxygen deficiency related to higher La content (LaWO56 and LaWO57) is only stabilized at higher temperatures and the stoichiometry is frozen-in if cooled sufficiently fast to low temperatures [90].

Enthalpy of disordering

In this section we will sketch out a simplified model that can describe the order-disorder transition in a defect chemical manner which can help us connect the activation energy of oxide ion conductivity to the observed ordering of vacancies. The fact that we observe that the amount of domains with vacancy order increases with x in $La_{2-x}Nd_xCe_2O_7$, could be an indication of an equilibrium reaction between disordered vacancies and vacancies that are ordered, either in clusters with intermediate range or in nanodomains with long range order. We have seen no evidence of an abrupt phase transition and instead we expect a development of ordering with decreasing temperature. This can be linked to the C-type related ordering found from DFT calculations consisting of distinct vac-vac alignments, e.g. <110> and <210> building blocks which align to form (C-type related) ordered clusters and domains That is, we expect the disorder-order reaction to start with the formation of vacancy pairs, before more vacancies collectively combine to first form clusters, followed by (more) long range ordered patterns. This process is comparable to the association-dissociation process between defects forming and dissolving dimers, trimers and larger clusters, and a proposed disordering reaction equation could be:

$$\frac{1}{2}(v_O v_O)^{\bullet\bullet\bullet\bullet} = v_O^{\bullet\bullet}, \qquad (28)$$

where the reactant is ordered pairs of vacancies and the product two disordered vacancies. More generally for larger clusters and domains the reaction could be written as:

$$\frac{1}{\mathrm{n}}(n\mathrm{v_O})^{n(\bullet\bullet)} = \mathrm{v_O^{\bullet\bullet}} \qquad (29)$$

Since it will require energy to disorder vacancies with strong interaction, the enthalpy part, $\Delta H_{disorder}$, of the change in Gibbs energy, ΔG, for the disordering reaction is naturally endothermic. The concentration of disordered vacancies will increase with temperature depending on the enthalpy through the expression for the equilibrium constant, $K_{disorder}$:

$$K_{disorder} = K_{0,disorder} \exp\left(\frac{-\Delta H_{disorder}}{RT}\right) = \frac{[\mathrm{v_O^{\bullet\bullet}}]}{[n\mathrm{v_O^{n\bullet\bullet}}]^{1/n}} \qquad (30)$$

This "equilibrium reaction-model" is also able to rationalize the presence of some short to intermediate range order in $La_2Ce_2O_7$ at low temperatures (i.e. room temp) as proposed in Paper II based on DFT results and the modulations observed in the diffraction patterns in Paper I. As a part of the equilibrium model, one should also expect the presence of some short range order, in addition to domains with long range order also in the Nd containing compositions of $La_{2-x}Nd_xCe_2O_7$.

Based on the ordering observed of vacancies through $La_{2-x}Nd_xCe_2O_7$ we expect that $\Delta H_{disorder}$ increases with increasing x. The long range ordered vacancies are stabilized so much that they become immobile. This is supported by the observation of reduced conductivity through reduced fraction of contributing vacancies due to ordering in nanodomains [93]. Short range order, such as pairs and clusters, has weaker interactions but can also influence the stability and concentration and mobility of vacancies at low temperatures. Although, $\Delta H_{disorder}$ in the case of long range order is expected to be significantly higher than the energy needed to disorder short range ordered vacancies, we use the same term for simplicity. We do not aim to provide exact values, but use the enthalpy term to illustrate how it contributes to the activation energy of conductivity.

Only vacancies that are mobile can contribute to vacancy conductivity, or put differently, an oxide ion can only jump to a vacant position if the vacancy is considered disordered and available for an oxide ion to jump to. The concentration of available and disordered vacancies is temperature dependent and can be derived by using Equation (30). However, in order to simplify the expression we will consider the two limiting situations; where all vacancies are ordered and where all vacancies are disordered. We use the electroneutrality condition:

$$[\mathrm{Ln'_{Ce}}] = \frac{2}{n}[n\mathrm{v_O^{n\bullet\bullet}}] + 2[\mathrm{v_O^{\bullet\bullet}}] \qquad (31)$$

in order to relate the concentration of vacancies to the concentration of dopants. If we assume that almost all vacancies will be ordered at sufficiently low temperature, then:

$$[\mathrm{Ln}'_{\mathrm{Ce}}] = \frac{2}{n}[n\mathrm{v}_{\mathrm{O}}^{\mathrm{n}\bullet\bullet}] \qquad (32)$$

By expressing the concentration of $n\mathrm{v}_{\mathrm{O}}^{\mathrm{n}\bullet\bullet}$ in terms of the constant dopant concentration and inserting in to Equation (30) we obtain:

$$[\mathrm{v}_{\mathrm{O}}^{\bullet\bullet}] = n/2\left[\mathrm{Ln}_{\mathrm{Ce}}^{'}\right]^{1/n} K_{0,disorder} \exp\left(\frac{-\Delta H_{disorder}}{RT}\right) \qquad (33)$$

The $\Delta H_{disorder}$ will therefore contribute to the activation energy, E_A, for oxide ion conductivity in $La_{2-x}Nd_2Ce_2O_7$, in addition to the enthalpy of mobility, ΔH_{mob}, which is the enthalpy needed for a oxide ion jump in the case of disassociated or disordered vacancies: $E_A = \Delta H_{mob} + \Delta H_{disorder}$.

However if all vacancies are disordered, the concentration is constant for the given temperature range (i.e. all vacancies are disordered) and then E_A is reduced to only ΔH_{mob}. (This is also the case if the temperature is too low to activate disordering which results in the fraction of vacancies being ordered remains constant.) For the transition between these two situations, the expression for the vacancy concentration cannot be simplified and will be a quadratic expression. In order to keep the connection between ordering/disordering and the activation energy simple, we will none-the-less describe the apparent activation energy as the sum of ΔH_{mob} and $\Delta H_{disorder}$ for the temperature regions where E_A is not solely determined by ΔH_{mob}.

The correlation between vacancy-vacancy interaction and conductivity is similar to those previously used for acceptor-vacancy associations in the dilute limit, e.g. in doped ceria where they see variations in E_A with temperature [45-47]. In our work on $La_{2-x}Nd_xCe_2O_7$, we also see some variation in E_A with temperature, which may reflect effects of ordering, and the difference in $\Delta H_{disorder}$ for the different compositions is reflected in the conductivity data for the $La_{2-x}Nd_xCe_2O_7$ samples. Figure 6 presents the isobaric conductivities in dry argon in an Arrhenius representation (Paper III) for the two end members $La_2Ce_2O_7$ and $Nd_2Ce_2O_7$. The fitted activation energies and pre-exponentials for the $La_{2-x}Nd_xCe_2O_7$ samples are listed in Table 1 and included for the end members in Figure 6. Table 1 and Figure 6 show that the apparent E_A for $La_2Ce_2O_7$ *decreases* with increasing temperature, and even more than listed here, to 95 kJ/mol at the highest temperatures (as mentioned in Paper III). By contrast, E_A for $Nd_2Ce_2O_7$ apparently *increases* with increasing temperature within the temperature window of our conductivity measurements.

The change in the apparent activation energy of the conductivity for the La rich compositions (i.e. $La_{2-x}Nd_xCe_2O_7$ with x = 0, 0.5 and 1), going from higher to lower values

with increasing temperature, supports the presence of a disordering process which play a smaller role in the total activation energy at higher temperatures. This type of behaviour is seen both experimentally [45-47] and computationally [97] in ceria doped with moderate concentrations of rare earths (below the percolation threshold), due to trapping of vacancies through association between dopants and vacancies [10, 45, 46]. We expect intermediate range ordering of vacancies to exist only to a small extent in $La_2Ce_2O_7$, and is most likely not as energetically favourable as long range ordering of vacancies in Nd-rich compositions as previously mentioned. Therefore, we assume that most vacancies in $La_2Ce_2O_7$ will be disordered already at temperatures just above ~1000 ºC, resulting in ΔH_{mob} being the dominating contribution to the activation energy.

For $Nd_2Ce_2O_7$, the higher activation energy above 400 ˚C can be interpreted as a transition from a lower temperature region, where a large part of the vacancies are remain ordered and immobilized, to a higher temperature region where the temperature is sufficiently high to activate a gradual disordering of long range ordered vacancies. In the higher temperature region where $Nd_2Ce_2O_7$ show a higher E_A, the disordering increases the fraction of disordered vacancies. Below 400 ˚C the fraction of long range order is assumed to be approximately constant and $E_A = \Delta H_{mob}$ (unless disordering of vacancies ordered in short to intermediate range also contributes). MD calculations at 1227 ºC show that vacancies also diffuse in $Nd_2Ce_2O_7$, even if they are initially ordered. Therefore we expect that all long range order of the oxygen lattice will eventually break down, at even higher temperatures and the activation energy will again be reduced to $E_A = \Delta H_{mob}$ in a temperature region above the temperature window used here, for electrical characterization.

Table 1 The fitted activation energies and pre-exponentials from the conductivity data for $La_{2-x}Nd_xCe_2O_7$ at low and high temperatures (200 - 500 and 500 - 1000 ˚C). E_A has the units kJ/mol and the pre-exponential A has the units $Scm^{-1}K$.

Temp. range (ºC)	E_A	A	E_A	A	E_A	A	E_A	A	E_A	A
	$La_2Ce_2O_7$		$La_{1.5}Nd_{0.5}Ce_2O_7$		$LaNdCe_2O_7$		$La_{0.5}Nd_{1.5}Ce_2O_7$		$Nd_2Ce_2O_7$	
500-200	111	$1.2\cdot10^6$	114	$2.6\cdot10^6$	116	$3.3\cdot10^6$	113	$1.7\cdot10^6$	113	$6.6\cdot10^5$
1000-500	103	$5.6\cdot10^5$	103	$6.5\cdot10^5$	103	$5.5\cdot10^5$	111	$1.1\cdot10^6$	119	$2.1\cdot10^6$

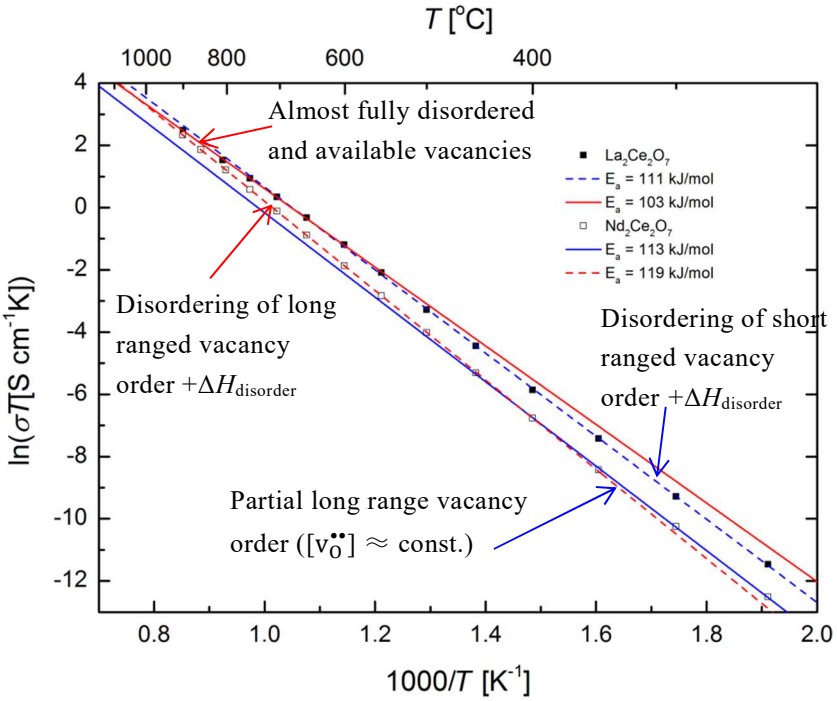

Figure 6 Measured conductivity in dry Argon for $La_2Ce_2O_7$ and $Nd_2Ce_2O_7$ plotted as $\ln(\sigma T)$ vs $1000/T$ and the linear fitting for high and low temperatures from which the E_a is derived from the slopes.

In fact, if we look closely at the temperature dependence of $La_{0.5}Nd_{1.5}Ce_2O_7$ we find that it exhibits three temperature regions as highlighted in Figure 7. The activation energy increases when the temperature rises above ~450 °C going from the first to the second region. As for $Nd_2Ce_2O_7$ this can be interpreted as the disordering contributing significantly to the E_A (between 450 and 700 °C) but with fewer long ranged ordered vacancies, needing less energy to fully disorder than $Nd_2Ce_2O_7$. Upon increasing the temperature above 700 °C, E_A decreases again (similar to $La_2Ce_2O_7$) indicating the start of a third temperature region where most vacancies are disordered. This observation strengthens the expectations of a similar development for $Nd_2Ce_2O_7$, at temperatures above the present temperature window.

Although the differences are quite small, the conductivity data show a gradual change in the apparent E_A and of the upper or lower temperature limit of the described regions when moving across the $La_{2-x}Nd_xCe_2O_7$ series. That the trends for the activation energy is changing in a consistent way through the $La_{2-x}Nd_xCe_2O_7$ series, support that there is temperature dependencies for the apparent activation energies which correlate to the different amount of observed vacancy ordering.

Also in LaWO it has been speculated whether there is an effect of temperature on the activation energy and vacancy ordering or clustering has been proposed as possible

explanation to higher activation energies at lower temperatures [98]. The activation energy of 85 kJ/mol found by fitting the conductivity data for LaWO56 at high temperatures [41] is significantly lower than the activation energy of 176 kJ/mol for oxide ion diffusion obtained by diffusion studies at lower temperatures on the same compound [98]. This is the similar type of temperature dependency on the activation energy as we have discussed here for $La_2Ce_2O_7$.

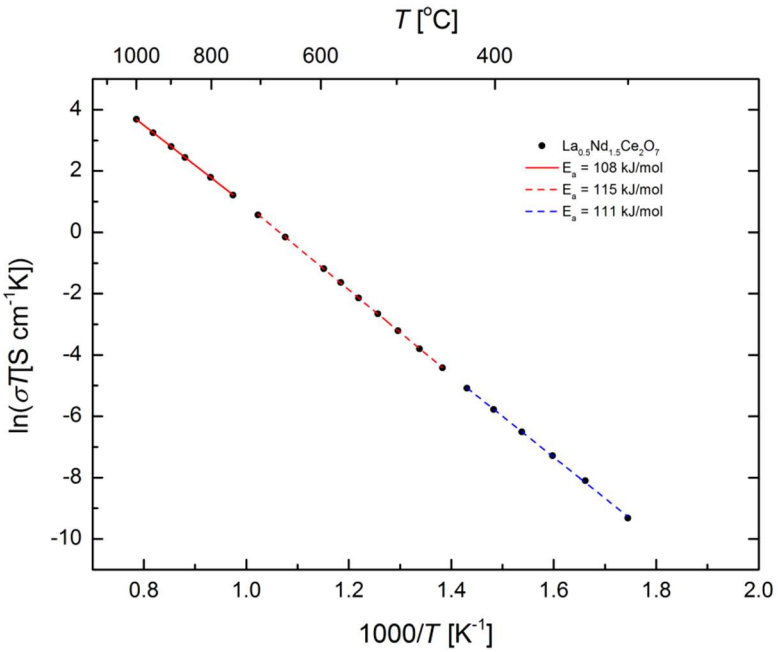

Figure 7 Arrhenius plot of the total conductivity in dry argon as a function of inverse temperature for $La_{0.5}Nd_{1.5}Ce_2O_7$.

We have shown that the conductivity data of $La_{2-x}Nd_xCe_2O_7$ support our model on a temperature dependent order-disorder equilibrium reaction similar to clustering of defects. This influences the activation energy for the measured conductivity. The trend in oxide ion mobility for these oxides will be addressed in Section 5.4 of this discussion.

5.3 The role of vacancy order and cation basicity on hydration

The hydration enthalpy reflects the change in energy between the dehydrated and hydrated state and will be influenced by the stability of the vacancies and the hydroxide defects (see Equation (7) in Section 2.2). In the current work we find the following two main factors affecting the hydration properties of $La_{2-x}Nd_xCe_2O_7$: *1*) long range ordering of vacancies which stabilizes vacancies limiting the number of vacancies that can contribute in the hydration equilibrium *and 2)* the basicity of La/Nd stabilizing the OH and giving more exothermic hydration enthalpy.

Vacancy ordering limiting hydration

Our preliminary DFT results suggest that long range ordering of vacancies in $La_{2-x}Nd_xCe_2O_7$ stabilizes vacancies to such a degree that the amount of vacancies available for hydration is reduced at low temperatures. Strong stabilization of vacancies through long range ordering is supported by the negative formation energy of the oxides found with DFT when configured with the C-type related vacancy order ("Ctype1") for $La_2Ce_2O_7$ and $Nd_2Ce_2O_7$.

Using DFT we estimate how the energy changes for a supercell by incorporating both one proton and one hydroxide defect at expected favourable positions in initially ordered and disordered configurations (additional details on the method are presented in Section 3.6). Although these preliminary test calculations cannot be used to accurately predict the hydration enthalpy, they will still point out some important observations. The first observation is that only when we allow the protons and oxide ions to relocate and relax after incorporation, using MD simulations, it results in hydrated configurations giving exothermic hydration enthalpies (see Figure 8). When able to relax through MD, the vacancies tend to order in C-type related manner like in the dehydrated configurations, reducing the total energy of the system. The results in Figure 8 show that the total energy varies significantly depending on the ordering of the oxygen sublattice both before and after hydration. The energy difference between disorder and ordered oxygen configurations is larger than the energy difference between dehydrated and hydrated state.

From these simulations, it is important to recognize that we have not found any hydrated configuration for any of the compounds studied that can provide exothermic hydration enthalpy when compared to the energy of the dehydrated "Ctype1" structure. *Consequently, vacancies that are part of long range ordered domains with C-type related order do not hydrate.* We may conclude that only the disordered vacancies in $La_{2-x}Nd_xCe_2O_7$ contribute to the effective vacancy concentration possible to hydrate.

The maximum hydration levels found for $La_{2-x}Nd_xCe_2O_7$ are, however, not limited by long range vacancy ordering alone. Our model where hydration of the *disordered* vacancies is driven and limited by proton trapping on La/Nd coordinated oxide ions, gives a reasonable fit to the maximum hydration relative to the amount of disordered domains (presented in Paper III and to be discussed shortly). However, there is still a small deviation between the maximum hydration based on these two models and the observed maximum hydration levels. This additional limitation in the hydration level at low temperatures could be explained by the presence of short range vacancy order in $La_{2-x}Nd_2Ce_2O_7$ in the domains that are otherwise considered disordered. Evolving short to intermediate range ordering as the temperature decreases, may give a slight decrease of the concentration of disordered vacancies as the hydration enthalpy changes to less exothermic values.

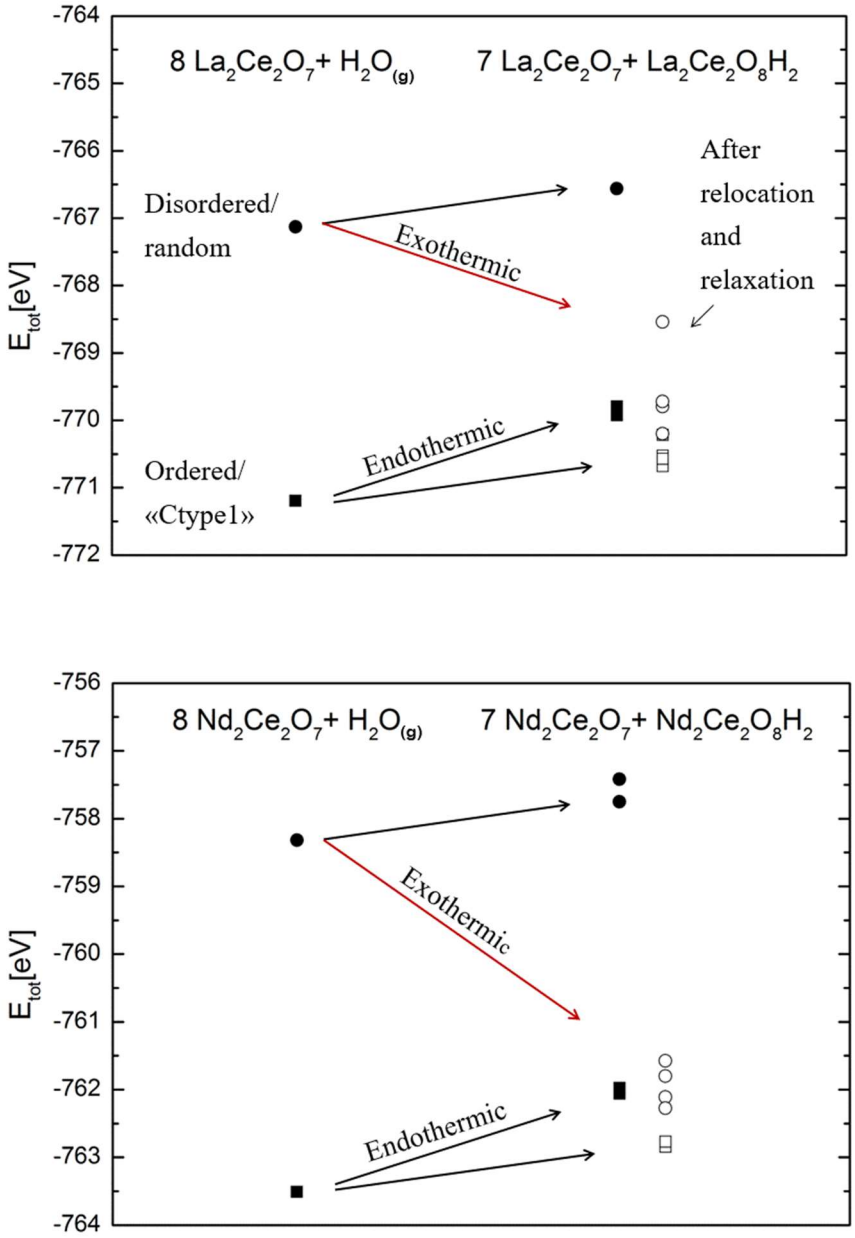

Figure 8 Total energy for one 88-ion supercell of $Ln_2Ce_2O_7$ (Z=8), summed with the energy of one molecule of H_2O to the left and further the total energy of a hydrated supercell configurations containing OH and H to the right. Ln = La is presented in the upper and Ln = Nd in the lower graph. Squared points are initially ordered oxygen configurations ("Ctype1"), and circles are oxygen configurations that are initially disordered (random configuration "Rand1"). We distinguish between the hydrated configurations to the right where filled points indicate configurations constructed by incorporating OH and H on chosen sites relaxed in the static limit, and the open, configurations obtained after oxide ions and protons are allowed to relocate and relax during MD runs.

Proton trapping due to the basicity of La

Using the preliminary DFT approach we have also looked into correlations between different placements of OH and the energy of hydrated configurations of $La_2Ce_2O_7$. By putting the protons at different positions and keeping the oxygen and cation arrangements fixed, we see that the energy of the configuration is lowered if: 1) protons are bonded to oxide ions which are only coordinated by La and 2) the La coordinating the protonated oxide ion has high average coordination numbers.

All oxide ions are coordinated by four cations. We can see from the results in Figure 9 that placing the proton on an oxide ion in a La tetrahedron generally is more favourable than in a Ce tetrahedron. This finding is the basis of the proposed model on H^+ being trapped on La-coordinated oxide ions (see page 4 of Paper III). The hydration is mostly driven by the basicity of the Ln cation, or more correctly the Ln-O complex. For all configurations, except one, the total energy of the hydrated supercell is correlated to the number of La coordinating the two oxide ions being protonated.

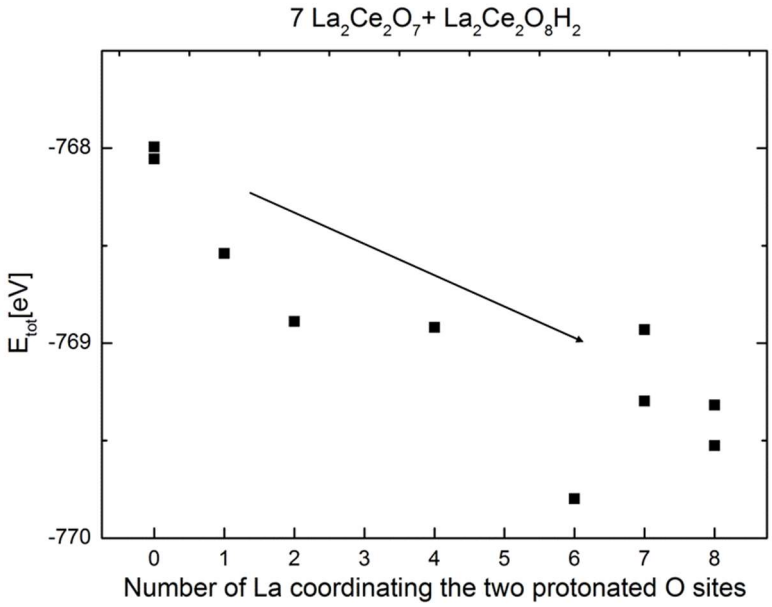

Figure 9 The total energy of a hydrated supercell relative to the number of La coordinating the two protonated oxide ions. The total number of cation coordinating the two protonated oxide ions always equals 8, and by subtracting the number on the x-axis from 8 the number of Ce coordinating the protonated oxide ion is obtained.

The exception is a very favourable configuration where only one of the two protons resides on an oxide ion in a La tetrahedron, and the other is on an oxide ion coordinated by both 2 Ce and 2 La. On the other hand, this configuration has, compared to any of the other configurations, a higher average coordination number for the La cations which are coordinating the oxide ions bonded to the protons. This observation also emphasizes the

importance of the effective basicity of the La-O: A higher oxygen coordination of the cation leads to weaker La-O bonds resulting in the complex becoming more basic.

Basicity of cations as key role in hydration

In LaWO and $La_{2-x}Nd_2Ce_2O_7$ we have until now concluded that only disordered vacancies contribute to the hydration process. As we have seen strong local vacancy order around W in LaWO, limits the concentration of vacancies available for hydration, whereas in $La_{2-x}Nd_xCe_2O_7$ the long range ordering of vacancies in domains does the same. DFT calculations also show that it is the oxide ions coordinated to the more basic cation La that will be bonded to protons in disordered $La_2Ce_2O_7$. Also in LaWO, we find from DFT that protons prefer to reside on oxide ions coordinated by the less acidic La cation, as we have commented on in a previous work [41]. The limited hydration in disordered $La_2Ce_2O_7$ seen in Paper III, called for an alternative model to the classic model where oxides are hydrated through hydration of existing vacancies and the concentration of vacancies determines the maximum hydration level. Therefore, we proposed a model where only statistically fully La^{3+} coordinated oxide ions are protonated (see page 4 of Paper III). That is, the basicity of La^{3+} enables the hydration in $La_2Ce_2O_7$ but also creates a site restriction for protons limiting the hydration. We assume that Nd ions in the disordered domains of $Nd_2Ce_2O_7$ plays the same role, although they have lower basicity. We will now assess this hydration model and how it is connected to observed trends in the hydration enthalpy of different relevant groups of oxides.

The hydration enthalpy of sesquioxides and pyrochlore structured oxides, has opposite correlations with Ln size as we now will see. For the sesquioxides (Ln_2O_3), Nd_2O_3 has smaller cation radius and lattice parameters and displays a more exothermic hydration enthalpy than La_2O_3 (-107 kJ/mol and -75 kJ/mol respectively [99]). For all the A-type and C-type sesquioxides the hydration enthalpy becomes more exothermic with smaller Ln cation sizes [36]. The hydration enthalpy of doped $Ln_2B_2O_7$ with the pyrochlore structure, shows the opposite trend than the sesquioxides with respect to the size correlation; the hydration enthalpy becomes less exothermic with smaller Ln size [32].

However, the stability of the pyrochlores increases with the larger rLn^{3+}/rB^{4+} [32], and for the sesquioxides the stability of the oxide increases with decreasing size [36]. Consequently, there is a correlation between the hydration enthalpy and the stability of the oxides for both oxide systems, which is rationalized by relating the oxides stability and the energy needed to form oxygen vacancies. Oxygen vacancies become more difficult to form the more stable the oxide is, resulting in less stable vacancies. Filling of vacancies then contributes significantly to exothermic enthalpy change when the oxide is hydrated. For all moderately doped oxides with high formation enthalpy for oxygen vacancies, it is likely that filling of

vacancies will contribute significantly, and the stability of introduced vacancies will explain trends of changing hydration enthalpy within a class of oxides.

For $La_{2-x}Nd_xCe_2O_7$, however, the correlation between oxide stability and hydration enthalpy fails to predict how the enthalpy of hydration will change through the series. First, if we consider $La_{2-x}Nd_xCe_2O_7$ to be 50% Ln doped CeO_2, the stability of the undoped oxide is the same for all compositions. The total energy of the doped oxide, $La_{2-x}Nd_xCe_2O_7$, should rather represent the stability of vacancies. Then the DFT results imply a more exothermic hydration enthalpy for $Nd_2Ce_2O_7$ since $La_2Ce_2O_7$ is found to be more stable than $Nd_2Ce_2O_7$ (see Paper II). This is not the case since the hydration enthalpy is found to be less exothermic when La is substituted by the smaller Nd cation. Although the concentration of vacancies is highly limited by vacancy ordering, the relative stability of the disordered oxygen lattice can thus not rationalize the trend for the value of hydration enthalpy observed in $Ln_2Ce_2O_7$.

Instead, we can correlate the hydration enthalpy in $Ln_2Ce_2O_7$ to the basicity of Ln^{3+} and the resulting bond length between Ln and oxide ions. Generally, a more basic oxide dissolves water more easily, and the basicity is a good correlation factor when looking at formation of oxyhydroxides from sesquioxides which happens more readily for the bigger La and Nd than for the smaller Ln cations in the period [100]. The sesquioxides on the other hand becomes less ionic and basic with decreasing Ln-O bond length [100], which notably is an argument for the hydration enthalpy of *doped* sesquioxides being dominated by the stability of the charge compensating vacancies, not basicity. Since basicity may rationalize how the hydration enthalpy changes in the $La_{2-x}Nd_xCe_2O_7$ series, we should try to understand any similarities to the formation of oxyhydroxides from sesquioxides, although we do not form $Ln(OH)_3$ in our $La_{2-x}Nd_xCe_2O_7$ samples.

Formation of $La(OH)_3$ and $Nd(OH)_3$ from Ln_2O_3 with the A-type hexagonal structure includes a phase transition as there are no obvious empty oxygen sites in the (undoped and perfect) hexagonal structure for interstitial OH groups. But, if Ln_2O_3 is in the C-type structure there will be room for some interstitial hydroxide groups on the empty 16c positions of the cubic fluorite. Interestingly, a study from Nagao et al. has shown that the crystal structure of Nd_2O_3 affects the hydration mechanisms, and C-type structured Nd_2O_3 has a higher reactivity towards water than A-type structured. Actually the C-type structure hydrates first to NdOOH which is structurally related to the C-type structure, before further transitioning to $Nd(OH)_3$ [100]. This would correspond to the incorporation of water as described in our hydration model where H+ associates to O connected to Ln^{3+} only, within the $Ln_2Ce_2O_7$ matrix. The filling of a vacant position (whether it is considered to create an interstitial or fill a vacancy) could be merely exothermic or even endothermic as long as the H+ trapping provides sufficient enthalpy gain to the hydration process. There are thus structural similarities between the C-type sesquioxides and their hydrated forms LnOOH.

This supports our model whereby basicity of oxygen surrounded by Ln^{3+} in disordered $Ln_2Ce_2O_7$ plays a key role in hydration of $Ln_2Ce_2O_7$ with a oxygen disordered cubic fluorite structure.

We can further argue that since the $Ln_2Ce_2O_7$ can be considered as a solid solution of Ln_2O_3 and CeO_2, it is possible to vary the stoichiometry (i.e. it is possible to vary the Ln to Ce ratio around 2:2 to some degree without encountering phase segregation), it is likely that filling vacancies in $Ln_2Ce_2O_7$ does not affect the stability of the oxide significantly or cause a large energy exchange during hydration. This further strengthens the idea that trapping of H^+ to oxide ions coordinated by Ln^{3+} in $Ln_2Ce_2O_7$ dominates the hydration enthalpy. Together with the fact that the resulting site limitations provide a better model for the maximum water uptake seen in $La_{2-x}Nd_xCe_2O_7$, we can conclude that our proposed hydration model based on basicity of Ln, explains the hydration in the disordered domains of the compositions.

La plays an important role for hydration of LaWO as well. DFT and calculations carried out using force field methods [72] show that the protons prefer oxide ions coordinated by La. The very acidic W creates feebly basic oxide complexes since W-O bonds are short and strong. The La-O bond on the other hand has a more ionic character.

It is thus a common feature for both LaWO and $La_2Ce_2O_7$ that H^+ is favourably bonded to an oxide ion surrounded by only La. Nd plays the same role in $Nd_2Ce_2O_7$. However, in LaWO filling of vacancies during the hydration reaction, most likely adds significant energy to the hydration enthalpy resulting in more exothermic values. Filling vacancies to avoid under-coordination of La is likely to be the driving force for the self-doping with W^{6+} in LaWO, as previously discussed. Thus, it is reasonable to expect that filling of vacancies gives a bigger contribution to the hydration enthalpy in LaWO than in $La_2Ce_2O_7$. LaWO, also, has several available oxide ions coordinated only by La^{3+} and unlike $Ln_2Ce_2O_7$ the number of available vacancies is what limits the hydration, not the available H^+ sites. The extra contribution to the hydration enthalpy in LaWO fits well with the measured hydration enthalpy being more exothermic than for $La_2Ce_2O_7$.

Table 2 Hydration enthalpy measured by TG-DSC, and the proposed energy contributions which significantly contributes to the hydration enthalpy.

	LaWO56	$La_2Ce_2O_7$	$Nd_2Ce_2O_7$
ΔH°_{hydr}	-90 kJ/mol ([43])	-77 kJ/mol	-72 kJ/mol
Main energy contribution	H^+ trapping + Filling of vacancy	H^+ trapping	H^+ trapping

The relatively high stability of disordered vacancies in highly oxygen disordered oxides tells us that the hydration enthalpy of such oxides is not dominated by the energy of filling of vacancies. It is rather the resulting stability of the OH formed which determines whether hydration will be more or less exothermic. The hydration model proposed in Paper III where the basic Ln^{3+} enables hydration, can be expected to be well suited for heavily oxygen deficient oxides that are able to accommodate high oxygen disorder. Strong interactions with the vacancies, such as the C-type related vacancy order in $Ln_2Ce_2O_7$, will impose additional limitations on hydration.

5.4 Ionic conductivity in defective fluorites

We have seen how varying degrees of vacancy ordering affects the concentration of "free" and mobile vacancies. Based on the discussion on how enthalpy of disorder affects the activation energy of oxide ion conductivity, we will now extract values for vacancy mobility and discuss how it changes between the compounds studied. We will further discuss how vacancy ordering and cation basicity affect the mobility and concentration of protons.

Oxide ion conductivity and mobility

Yttria stabilized zirconia (YSZ) and Gd doped ceria (GDC) are known as state-of-the-art oxide ion conductors [11]. $La_2Ce_2O_7$ also shows high oxide ion conductivity at high temperatures (~900 ºC) [14], close to the values reported for YSZ and slightly lower than GDC. The oxide ion conductivity measured experimentally for $La_{2-x}Nd_xCe_2O_7$ in this work is lower than reported previously [14], since the conductivity has not been corrected for the high porosity. The oxide ion conductivity for the different $La_{2-x}Nd_xCe_2O_7$ compositions does not differ much within the series, except for $Nd_2Ce_2O_7$ where it is approximately half an order of magnitude lower than $La_2Ce_2O_7$ and the other compositions at 400 °C (shown in Paper III). This is as expected due to the differences in long range order that results in different effective concentrations of oxygen vacancies contributing to oxide ion transport. The activation energy for the oxide ion conductivity is also higher in $Nd_2Ce_2O_7$ than $La_2Ce_2O_7$. This is in line with results from MD runs at 1500 K, showing more collective diffusion and a lower diffusion coefficient (D_{tracer}) for oxide ions in $Nd_2Ce_2O_7$ (Paper II). The higher activation energy found for $Nd_2Ce_2O_7$ compared to $La_2Ce_2O_7$, results in the total conductivity being more similar at high temperatures.

It is interesting to compare the vacancy mobility for the compounds studied to see how it changes with the size of the unit cell. We can compare $\Delta H_{mob,O}{}^{2-}$ by using the E_A from the temperature region where the concentration of disordered oxygen vacancies can be considered approximately constant, based on the discussion regarding the activation energy

of oxide ion conductivity in Section 5.2. For LaWO and $La_2Ce_2O_7$, it would be the activation energies for oxide ion conductivity at higher temperatures and for $Nd_2Ce_2O_7$ at lower temperatures, which best represents the activation energy for jumping, $\Delta H_{mob,O}^{2-}$, for oxide ions when jumping to a vacant oxygen position without disrupting vacancy order (i.e. all vacancies are disordered). On this basis we find a trend where the mobility of oxide ions decreases with decreasing size of the unit cell, as seen in Table 3. Note that this trend is opposite of what has been reported for CeO_2 with low doping levels where mismatch in cation size results in lower mobility [11]. On the other hand, it is in accordance with the oxide ion mobility decreasing with decreasing Ln size and lattice constant in LaWO [17].

Table 3 ΔH_{mob} evaluated from conductivity measurements. For $La_2Ce_2O_7$ twice of the lattice constant for a fluorite cell is given for best comparison

	LaWO56	$La_2Ce_2O_7$	$Nd_2Ce_2O_7$
$\Delta H_{mob,O}^{2-}$,	~85 (High *T*) [41]	~103 (95) (High *T*)	~113 (Low *T*)
Lattice const.	11.18 Å [30]	11.05 Å [Paper I]	10.88 Å [Paper I]

It is easy to argue that mobility of oxide ions/vacancies correlates with changes in cell size if the structure is otherwise comparable (e.g. cubic fluorite). The jumping distance in cubic defective fluorites is proportional to the lattice constant since oxide ions in fluorite jump to the nearest oxygen site in the <100> direction [50]. Larger lattice size also indicates longer and thus weaker Cat-O (or Ln-O) bonds, reducing the jumping barrier. Larger Ln and longer more ionic bonds are thus favourable for high oxide ion mobility, as well as, for effective concentration of charge carriers since larger Ln also seems to stabilize more disorder between the vacancies (according to the previous discussion). The diffusion coefficients found for oxide ions in $La_2Ce_2O_7$ and $Nd_2Ce_2O_7$ by MD calculations support this simple correlation.

LaWO displays lower oxide ion conductivity than $La_2Ce_2O_7$ and $Nd_2Ce_2O_7$ at high temperatures (at 800 ºC $La_2Ce_2O_7$ show a total ionic conductivity in the order of 10^{-2} S/cm [14] and LaWO53 to LaWO57 in the order 10^{-3} S/cm [41]), which is as expected due to the significantly lower concentration of available/mobile vacancies in LaWO as shown previously. A common feature for LaWO and $Ln_2Ce_2O_7$ studied here is that oxygen vacancies are quite mobile, despite all the structural barriers related to vacancy interactions, as already discussed. The high flexibility in the coordination sphere around La and the ionic and relatively weak bonds between oxide ions and La allow for distorted cubes and variations in the coordination number of each La cation. Furthermore, the relatively open fluorite structure allows for easy diffusion.

Proton conductivity and mobility

In our work, we find that the proton conductivity in $Ln_{2-x}Nd_xCe_2O_7$ decreases in magnitude with x and so does the maximum measured water uptake. More generally, we can say that proton conductivity decreases with smaller Ln in $Ln_2Ce_2O_7$, a trend which is supported by measurements performed in other studies, [14, 101, 102], as shown in Figure 10. The figure also show that additional Ca doping of $Ln_2Ce_2O_7$ results in lower proton conductivity than the pure $Ln_2Ce_2O_7$ compounds ($Sm_2Ce_2O_7$ [102], $Nd_2Ce_2O_7$ and $Gd_2Ce_2O_7$ [101]). The drop in conductivity followed by Ca doping, can be rationalized by additional concentration of charge compensating vacancies inducing more long range vacancy order, limiting the hydration further. As shown previously for LaWO, the La/W ratio determines the effective oxygen vacancy concentration and both the water uptake and proton conductivity decrease with increasing W content [41, 43] due to the resulting decrease in concentration of vacancies that are mobile and hydratable. The observed decrease in proton conductivity is thus mostly due to a lower proton concentration correlated with a lower concentration of "free" vacancies available for hydration.

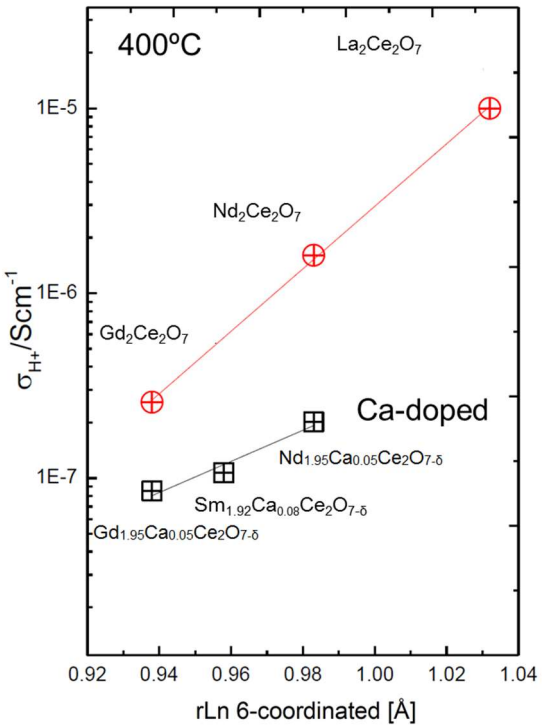

Figure 10 Proton conductivity in different fluorite structured $Ln_2Ce_2O_7$: $La_2Ce_2O_7$ from [14], $Gd_2Ce_2O_7$, $Gd_{1.95}Ca_{0.05}Ce_2O_7$, $Nd_2Ce_2O_7$ and $Nd_{1.95}Ca_{0.05}Ce_2O_7$ from [101], and $Sm_{1.92}Ca_{0.08}Ce_2O_7$ from [102].

The extent whereby vacancy ordering limits the water uptake, increases and the hydration enthalpy become less exothermic with smaller Ln in Ln2Ce2O7, explaining the decrease in proton conductivity through the series of lanthanide cerates seen in Figure 10. It is natural

to expect a trend where the proton mobility increases with Ln-O bond length and lattice constants, identical to what we found for the oxygen mobility for LaWO and $La_{2-x}Nd_xCe_2O_7$. The apparent activation energies determined by the σT *vs* $1/T$ Arrhenius plot of the proton conductivity in $La_{2-x}Nd_xCe_2O_7$, do in fact increase with the content of the smaller Nd, from ~43 kJ/mol for $La_2Ce_2O_7$ to around ~50 kJ/mol for $Nd_2Ce_2O_7$. However, if we compare the activation energy for proton conductivity in LaWO with $La_2Ce_2O_7$ and $Nd_2Ce_2O_7$ it does not correlated with decreasing lattice size (E_A for proton diffusion studied in LaWO56 is found to be 63 kJ/mol [98] and E_A from conductivity measurements is found to be ~60 kJ/mol [41]). The activation energy of proton diffusion is expected to be higher in LaWO than in $La_2Ce_2O_7$, since the proton conductivity of LaWO is higher at 200 °C while at the same time the proton concentration is found to be lower than in $La_2Ce_2O_7$. This indicates that the apparent activation energy for $La_{2-x}Nd_xCe_2O_7$ extracted from conductivity measurements contains additional contributions.

At the temperatures where proton conductivity is measured in $La_{2-x}Nd_2Ce_2O_7$, the concentration of protons is indeed not constant but rather decreasing with increasing temperature, according to TG-DSC measurements (Paper III). The apparent activation energy for the measured proton conductivity will thus include an energy contribution from formation of protons since the conductivity is proportional to the proton concentration (see Equation (19)). For $La_{2-x}Nd_2Ce_2O_7$ we propose that the hydration enthalpy is dominated by the energy gain of trapping H^+ on oxide ions coordinated by La and Nd in $Nd_2Ce_2O_7$ (see Paper III). As discussed in Section 5.3 we assume that filling vacancies does not contribute significantly to the hydration enthalpy. The hydration enthalpy can then be considered as the enthalpy of formation for 2 protons which contributes to the apparent activation energy $E_{apparent(H^+)}$. Consequently, there is an additional (negative) energy contribution to the apparent activation energy besides the enthalpy of mobility of protons, which can be derived from the hydration enthalpy:

$$E_{apparent(H^+)} = \Delta H°_{hydr}/2 + E_{A(H^+)} = \Delta H°_{hydr}/2 + \Delta H_{mob(H^+)} \quad (34)$$

where the latter is the activation energy for proton mobility. $E_{apparent}$ = 43 kJ/mol and $\Delta H°_{hydr}$ = -77 kJ/mol, results in $E_{A(H^+)} = \Delta H_{mob(H^+)}$ = 81.5 kJ/mol for $La_2Ce_2O_7$. Similarly, we obtain $E_{A(H^+)} = \Delta H_{mob(H^+)}$ = 85.5 kJ/mol for $Nd_2Ce_2O_7$ where $\Delta H°_{hydr}$= 71 kJ/mol and $E_{apparent}$= 50 kJ/mol.

The hydration model for $La_{2-x}Nd_xCe_2O_7$, also suggests that the same energy term can be interpreted as trapping energy of two protons (i.e. $\Delta H_{H^+trap} = -\Delta H°_{hydr}/2$). Thus, we can make a rough estimate of the enthalpy of mobility for untrapped protons $\Delta H_{mob(freeH^+)}$ by solving this equation:

$$E_{A(H^+)} = \Delta H_{mob(H^+)} = \Delta H_{mob(free\ H^+),0} + \Delta H_{H^+trap} = \Delta H_{mob(free\ H^+),0} - \Delta H°_{hydr}/2, \quad (35)$$

which subsequently give the approximation:

$$E_{apparent(H^+)} = \Delta H_{mob(freeH^+)} \quad (36)$$

The value of $E_{apparent(H^+)} = \Delta H_{mob(freeH^+)}$ thus represents the activation energy for "free" proton jumps, whereas $\Delta H_{mob(H^+)}$ takes the additional trapping of protons into account.

For LaWO, on the other hand, the activation enthalpy of proton diffusion is extracted directly from diffusion studies and we can trust that the activation energy of proton diffusion equals the enthalpy of mobility for protons ($E_A = \Delta H_{mob}$) which can be compared to the ΔH_{mob} derived for Ln2Ce2O7. The correlation between mobility and Ln-O bond lengths, and consequently lattice size, is identical with the correlation we obtained for the ΔH_{mob} for oxygen ions previously. It is also in accordance with the trends observed for cubic rare earth oxide series where the conductivity decreases with decreasing lattice [103]. Furthermore, it can explain why LaWO has higher proton conductivity than $La_2Ce_2O_7$ although $La_2Ce_2O_7$ contains more protons at ~200 ºC. The resulting activation energies for mobility of protons found are 20-30% lower than for oxygen vacancies, which we observe is typical in oxides.

Table 4 Apparent activation energies, for proton conductivity derived from conductivity experiments and $\Delta H_{mob(H^+)}$ for protons as derived by the model describing trapping of protons in Ln2Ce2O7.

	LaWO56	$La_2Ce_2O_7$	$Nd_2Ce_2O_7$
$E_{apparent}$ (kJ/mol) (from conductivity experiments)		43 kJ/mol [PaperIII]	50 kJ/mol [PaperIII]
~$\Delta H_{mob(H^+)}$ (kJ/mol) (derived from proposed hydration model for Ln2Ce2O7)	63 kJ/mol [98]	82 kJ/mol	86 kJ/mol

6 Summarizing conclusions

"Nothing in life is to be feared, it is only to be understood."

– Marie Curie

In this work we have investigated the relationship between local and average structure in LaWO and $La_{2-x}Nd_xCe_2O_7$ in order to explain their defect related properties - oxide ion conductivity, hydration and proton conductivity. LaWO and $La_{2-x}Nd_xCe_2O_7$ crystallize in cubic, fluorite derived structures, which are highly oxygen deficient with respect to the perfect fluorite. The local atomic structure in these oxides cannot be determined by average structure models without losing essential information needed to determine the defect situation. Combining computational and experimental methods provides complementary information about the structure in complex oxides, and is valuable in order to understand both local and average structure in fluorite related oxides.

In LaWO, strong covalent bonds between W and O, result in strong local ordering of vacancies around W. This limits the effective concentration of vacancies that are available for diffusion and hydration. In $La_{2-x}Nd_xCe_2O_7$ the high number of vacancies results in partial long range vacancy ordering in a C-type related manner for the Nd containing samples. Rietveld refinements of total scattering neutron diffraction on $La_{2-x}Nd_xCe_2O_7$ reveal that $La_2Ce_2O_7$ is best described as a disordered fluorite, whereas long range vacancy order evolves in the system with increasing Nd content. We find evidence of nanodomains with long range ordering in $Nd_2Ce_2O_7$ using HR-TEM. This corresponds perfectly with a model combining oxygen excess C-type and oxygen deficient fluorite structures giving the best fit in the Rietveld refinements. We therefore conclude that $La_{2-x}Nd_xCe_2O_7$ compounds where $x > 0$ consists of two types of domains at low temperatures, where vacancies are disordered in one and long range ordered in the other.

DFT calculations show that the C-type related ordering is favourable for both $La_2Ce_2O_7$ and $Nd_2Ce_2O_7$ and are a way of ordering vacancies in oxygen deficient, cubic fluorites not previously described. C-type related vacancy ordering is a good way to order vacancies for oxygen deficient fluorites with cations of relatively large size and low electronegativity such as Ln cations (given that different cations have similar size). However, in LaWO,

where the cations have different sizes, the long La-O bonds enable disorder in and distortion of the oxygen lattice surrounding La. The long La-O bond and slightly larger difference in cation sizes, also enable more disorder in $La_2Ce_2O_7$ compared to $Nd_2Ce_2O_7$. The local structure of short or long ranged vacancy ordering in cubic fluorites can thus be correlated with the size and electronegativity of the cations, the resulting lattice volume and whether the cations have equal sizes or not.

The enthalpy gain of long range ordering in $Nd_2Ce_2O_7$ is slightly higher than in $La_2Ce_2O_7$, which is correlated with the smaller lattice constants and shorter Cat-O bonds of the former. This is rationalized by C-type related vacancy ordering enabling a better close packing for the oxides with smaller cations and cell volume. Dynamic oxygen disorder is more significant for $La_2Ce_2O_7$ than $Nd_2Ce_2O_7$, and is an important explanation for the disorder observed in $La_2Ce_2O_7$. Configurational and vibrational entropy contribute to the difference in the extent of vacancy ordering between $La_2Ce_2O_7$ and $Nd_2Ce_2O_7$, resulting in disorder being stabilized to lower temperatures in $La_2Ce_2O_7$ than for $Nd_2Ce_2O_7$.

The apparent activation energies for oxide ion conductivity in $La_{2-x}Nd_xCe_2O_7$ which are found to change with temperature can be explained by the additional contribution from the enthalpy of disorder. We find that an equilibrium between order and disorder can be rationalized, where the degree of ordering increases with decreasing temperature for $La_{2-x}Nd_xCe_2O_7$. The enthalpy of disordering will influence the effective concentration of disordered vacancies available for oxide ion diffusion and hydration. At room temperatures and below there may be kinetic limitations to the ordering, hindering the whole sample from becoming fully ordered and creating frozen-in disorder.

From the experimental TG-DSC results, we find that the water uptake in $La_{2-x}Nd_xCe_2O_7$ is strongly limited being always less than 1 mol vacancy per formula unit, and increasingly so with increasing *x*. Based on the measurements and DFT computations we show that there are two important factors influencing the hydration reaction in $La_{2-x}Nd_xCe_2O_7$: 1) vacancy ordering and 2) basicity of the Ln cation. The first factor limits the effective concentration of vacancies, whereas the second influences the mobility of free vacancies and the hydration enthalpy through the strength of H+ trapping/LnO-H bonds.

In $La_{2-x}Nd_xCe_2O_7$, long range order limits the hydration by stabilizing the oxygen vacancies and making them unfavourable to hydrate. For the hydration of the oxygen disordered domains of $La_{2-x}Nd_xCe_2O_7$, the dominating energy contribution to the hydration enthalpy is trapping of H^+ on oxide ions coordinated by the more basic Ln, supported by DFT results. This hydration model imposes a site limitation for H^+ that fits well to the measured water uptake in the disordered $La_2Ce_2O_7$. The general trend for the hydration enthalpy of $Ln_2Ce_2O_7$ is that it becomes less exothermic with smaller Ln and shorter Ln-O bonds due to lower basicity. In LaWO the hydration enthalpy is more exothermic and filling of

vacancies is assumed to contribute significantly to the hydration enthalpy. Also, it is the number of available vacancies that imposes the hydration limit for LaWO, not the possible proton sites.

Our hydration model for $La_2Ce_2O_7$, is a good model for oxides that tolerate a high number of vacancies due to doping by basic acceptors (large cations such as La). The model is relevant for all oxides where vacancies are stabilized in a disordered lattice, since the importance of H^+ trapping to basic Ln-O complexes increases when filling vacancies contributes less to the hydration enthalpy.

The mobility for untrapped vacancies and protons increases with increasing fluorite lattice constants and Ln-O bonds. Accordingly, the mobility decreases in the order: LaWO > $La_2Ce_2O_7$ > $Nd_2Ce_2O_7$.

The high proton mobility of LaWO is due to the large cell volume and the percolating diffusion pathway between favourable proton sites. LaWO exhibits relatively high exothermic hydration enthalpy and proton mobility, making it a good proton conductor. The low concentration of mobile vacancies and the site restrictions reducing the possible sites to jump to, result in a lower oxide ion conductivity of LaWO than of $La_2Ce_2O_7$, even though the energy needed for vacancies to jump is lower.

In $La_2Ce_2O_7$ the relatively high stability of disordered oxygen vacancies offers a high effective concentration of vacancies yielding high oxide ion conductivity. However, the hydration enthalpy is less exothermic than for LaWO, and the hydration is strongly limited due to site restrictions for H^+. Consequently, $La_2Ce_2O_7$ only exhibits a minor contribution from protons to the total conductivity.

The concentration of free and disordered vacancies is strongly reduced with the Nd content in $La_{2-x}Nd_xCe_2O_7$ due to long range ordering of vacancies. Together with lower mobility, the reduced effective concentration of vacancies lowers the oxygen ion conductivity and limits the hydration compared to $La_2Ce_2O_7$, making $Nd_2Ce_2O_7$ both a poor oxide ion and proton conductor.

The findings in this thesis have led to general trends and insights which contribute to the understanding of defect related properties of oxides containing lanthanides in cubic fluorite related structures with oxygen disorder.

7 References

[1] C. Duan, J. Huang, N. Sullivan, R. O'Hayre, *Applied Physics Reviews* **7** (2020) (1) 011314.

[2] J. Kim, S. Sengodan, S. Kim, O. Kwon, Y. Bu, G. Kim, *Renewable and Sustainable Energy Reviews* **109** (2019) 606.

[3] H.-I. Ji, J.-H. Lee, J.-W. Son, K.J. Yoon, S. Yang, B.-K. Kim, *Journal of the Korean Ceramic Society* **57** (2020) (5) 480.

[4] L. Yang, S. Wang, K. Blinn, M. Liu, Z. Liu, Z. Cheng, M. Liu, *Science* **326** (2009) (5949) 126.

[5] Y. Larring, T. Norby, *Solid State Ionics* **136-137** (2000) (2) 139.

[6] C. Zhou, J. Sunarso, Y. Song, J. Dai, J. Zhang, B. Gu, W. Zhou, Z. Shao, *Journal of Materials Chemistry A* **7** (2019) (21) 13265.

[7] T. Norby, *Solid State Ionics* **125** (1999) (1-4) 1.

[8] S. Choi, C.J. Kucharczyk, Y. Liang, X. Zhang, I. Takeuchi, H.-I. Ji, S.M. Haile, *Nature Energy* **3** (2018) (3) 202.

[9] C. Duan, R.J. Kee, H. Zhu, C. Karakaya, Y. Chen, S. Ricote, A. Jarry, E.J. Crumlin, D. Hook, R. Braun, N.P. Sullivan, R. O'Hayre, *Nature* **557** (2018) (7704) 217.

[10] N. Jaiswal, K. Tanwar, R. Suman, D. Kumar, S. Upadhyay, O. Parkash, *Journal of Alloys and Compounds* **781** (2019) 984.

[11] S.J. Skinner, J.A. Kilner, *Materials Today* **6** (2003) (3) 30.

[12] C. Tandé, D. Pérez-Coll, G.C. Mather, *Journal of Materials Chemistry* **22** (2012) (22) 11208.

[13] D. Nishioka, T. Tsuchiya, W. Namiki, M. Takayanagi, K. Kawamura, T. Fujita, R. Yukawa, K. Horiba, H. Kumigashira, T. Higuchi, *Nanoscale Research Letters* **15** (2020) (1) 42.

[14] V. Besikiotis, C.S. Knee, I. Ahmed, R. Haugsrud, T. Norby, *Solid State Ionics* **228** (2012) 1.

[15] Z. Zhu, B. Liu, J. Shen, Y. Lou, Y. Ji, *Journal of Alloys and Compounds* **659** (2016) 232.

[16] W. Sun, S. Fang, L. Yan, W. Liu, *Fuel Cells* **12** (2012) (3) 457.

[17] R. Haugsrud, *Solid State Ionics* **178** (2007) (7-10) 555.

[18] R. Haugsrud, C. Kjølseth, *J. Phys Chem Solids* **69** (2008) (7) 1758.

[19] T. Shimura, S. Fujimoto, H. Iwahara, *Solid State Ionics* **143** (2001) (1) 117.

[20] V. Besikiotis, S. Ricote, M.H. Jensen, T. Norby, R. Haugsrud, *Solid State Ionics* **229** (2012) 26.
[21] H. Yamamura, H. Nishino, K. Kakinuma, K. Nomura, *Journal of the Ceramic Society of Japan* **111** (2003) (1300) 902.
[22] T. Hagiwara, Z. Kyo, A. Manabe, H. Yamamura, K. Nomura, *J. Ceram. Soc. Jpn.* **117** (2009) (Dec.) 1306.
[23] L. Li, R. Kasse, S. Phadke, W. Qiu, A. Huq, J.C. Nino, *Solid State Ionics* **221** (2012) 15.
[24] V. Grover, S.V. Chavan, P. Sengupta, A.K. Tyagi, *Journal of the European Ceramic Society* **30** (2010) (15) 3137.
[25] D.E.P. Vanpoucke, P. Bultinck, S. Cottenier, V. Van Speybroeck, I. Van Driessche, *Physical Review B* **84** (2011) (5) 054110.
[26] D.E.P. Vanpoucke, P. Bultinck, S. Cottenier, V. Van Speybroeck, I. Van Driessche, *Journal of Materials Chemistry A* **2** (2014) (33) 13723.
[27] E. Reynolds, P.E.R. Blanchard, Q. Zhou, B.J. Kennedy, Z. Zhang, L.-Y. Jang, *Physical Review B* **85** (2012) (13) 132101.
[28] L. Minervini, R.W. Grimes, K.E. Sickafus, *Journal of the American Ceramic Society* **83** (2000) (8) 1873.
[29] A. Magraso, C. Frontera, D. Marrero-Lopez, P. Nunez, *Dalton Transactions* (2009) (46) 10273.
[30] A. Magraso, C. Frontera, D. Marrero-Lopez, P. Nunez, *Dalton Trans.* (2009) (46) 10273.
[31] Q. Zhang, X. Zheng, J. Jiang, W. Liu, *The Journal of Physical Chemistry C* **117** (2013) (40) 20379.
[32] T.S. Bjørheim, V. Besikiotis, R. Haugsrud, *Dalton Trans.* **41** (2012) (43) 13343.
[33] F.A. Kröger, H.J. Vink, *Journal of Physics and Chemistry of Solids* **5** (1958) (3) 208.
[34] T. Norby, M. Wideroe, R. Gloeckner, Y. Larring, *Dalton Trans.* (2004) (Copyright (C) 2011 American Chemical Society (ACS). All Rights Reserved.) 3012.
[35] T. Zacherle, A. Schriever, R.A. De Souza, M. Martin, *Physical Review B* **87** (2013) (13) 134104.
[36] Y. Larring, T. Norby, *Solid State Ionics* **97** (1997) (1–4) 523.
[37] K.D. Kreuer, T. Dippel, Y.M. Baikov, J. Maier, *Solid State Ionics* **86-88** (1996) 613.
[38] A. Løken, T.S. Bjørheim, R. Haugsrud, *Journal of Materials Chemistry A* **3** (2015) (46) 23289.
[39] T.S. Bjørheim, M.F. Hoedl, R. Merkle, E.A. Kotomin, J. Maier, *The Journal of Physical Chemistry C* **124** (2020) (2) 1277.
[40] R. Haugsrud, Y. Larring, T. Norby, *Solid State Ionics* **176** (2005) (39–40) 2957.
[41] S. Erdal, L.-E. Kalland, R. Hancke, J. Polfus, R. Haugsrud, T. Norby, A. Magraso, *Int. J. Hydrogen Energy* **37** (2012) (9) 8051.

[42] R. Hancke, Z. Li, R. Haugsrud, *International Journal of Hydrogen Energy* **37** (2012) (9) 8043.
[43] R. Hancke, A. Magrasó, T. Norby, R. Haugsrud, *Solid State Ionics* **231** (2013) (0) 25.
[44] H. Iwahara, H. Uchida, N. Maeda, *Journal of Power Sources* **7** (1982) (3) 293.
[45] D.Y. Wang, D.S. Park, J. Griffith, A.S. Nowick, *Solid State Ionics* **2** (1981) (2) 95.
[46] R. Gerhardt-Anderson, A.S. Nowick, *Solid State Ionics* **5** (1981) 547.
[47] J. Faber, C. Geoffroy, A. Roux, A. Sylvestre, P. Abélard, *Applied Physics A Solids and Surfaces* **49** (1989) (3) 225.
[48] V. Butler, C.R.A. Catlow, B.E.F. Fender, J.H. Harding, *Solid State Ionics* **8** (1983) (2) 109.
[49] L. Minervini, M.O. Zacate, R.W. Grimes, *Solid State Ionics* **116** (1999) (3–4) 339.
[50] J. Koettgen, S. Grieshammer, P. Hein, B.O.H. Grope, M. Nakayama, M. Martin, *Physical Chemistry Chemical Physics* **20** (2018) (21) 14291.
[51] S. Hull, S.T. Norberg, I. Ahmed, S.G. Eriksson, D. Marrocchelli, P.A. Madden, *J. Solid State Chem.* **182** (2009) (10) 2815.
[52] S.P. Ray, D.E. Cox, *Journal of Solid State Chemistry* **15** (1975) (4) 333.
[53] T.R. Welberry, B.D. Butler, J.G. Thompson, R.L. Withers, *Journal of Solid State Chemistry* **106** (1993) (2) 461.
[54] H.J. Rossell, H.G. Scott, *J Phys (Paris) Colloq* **38 Colloq C-7** (1977) (12) c7. 28.
[55] Z.G. Liu, J.H. Ouyang, K.N. Sun, *Fuel Cells* **11** (2011) (2) 153.
[56] D.R. Ou, T. Mori, F. Ye, T. Kobayashi, J. Zou, G. Auchterlonie, J. Drennan, *Appl. Phys. Lett.* **89** (2006) (17) 171911/1.
[57] R.L. Withers, J.G. Thompson, N. Gabbitas, L.R. Wallenberg, T.R. Welberry, *Journal of Solid State Chemistry* **120** (1995) (2) 290.
[58] C. Artini, M.M. Carnasciali, J.R. Plaisier, G.A. Costa, M. Pani, *Solid State Ionics* **311** (2017) 90.
[59] C. Artini, G.A. Costa, M. Pani, A. Lausi, J. Plaisier, *Journal of Solid State Chemistry* **190** (2012) 24.
[60] H. Rietveld, *Journal of Applied Crystallography* **2** (1969) (2) 65.
[61] D. Keen, *Journal of Applied Crystallography* **34** (2001) (2) 172.
[62] M.G. Tucker, D.A. Keen, M.T. Dove, A.L. Goodwin, Q. Hui, *Journal of Physics: Condensed Matter* **19** (2007) (33) 335218.
[63] C. Kjølseth, L.-Y. Wang, R. Haugsrud, T. Norby, *Solid State Ionics* **181** (2010) (39) 1740.
[64] NorECs, ProboStat™.
[65] J.T.S. Irvine, D.C. Sinclair, A.R. West, *Advanced Materials* **2** (1990) (3) 132.
[66] S.M. Haile, D.L. West, J. Campbell, *Journal of Materials Research* **13** (1998) (6) 1576.

[67] J. Mizusaki, K. Waragai, S. Tsuchiya, H. Tagawa, Y. Arai, Y. Kuwayama, *Journal of the American Ceramic Society* **79** (1996) (1) 109.
[68] J. Fleig, *Solid State Ionics* **131** (2000) (1) 117.
[69] J. Fleig, J. Maier, *Journal of the American Ceramic Society* **82** (1999) (12) 3485.
[70] J.H. Harding, *Reports on Progress in Physics* **53** (1990) (11) 1403.
[71] B.G. Dick, A.W. Overhauser, *Physical Review* **112** (1958) (1) 90.
[72] J.D. Gale, *Journal of the Chemical Society, Faraday Transactions* **93** (1997) (4) 629.
[73] M.S. Islam, S. Lazure, R.-n. Vannier, G. Nowogrocki, G. Mairesse, *J. Mater. Chem.* **8** (1998) (3) 655.
[74] D.J. Driscoll, M.S. Islam, P.R. Slater, *Solid State Ionics* **176** (2005) (5-6) 539.
[75] P. Hohenberg, W. Kohn, *Physical Review* **136** (1964) (3B) B864.
[76] W. Kohn, L.J. Sham, *Physical Review* **140** (1965) (4A) A1133.
[77] G. Kresse, J. Furthmueller, *Phys. Rev. B: Condens. Matter* **54** (1996) 11169.
[78] Y. Wang, J.P. Perdew, *Physical Review B* **44** (1991) (24) 13298.
[79] J.P. Perdew, K. Burke, M. Ernzerhof, *Physical Review Letters* **77** (1996) (18) 3865.
[80] P.E. Blöchl, *Physical Review B* **50** (1994) (24) 17953.
[81] A. Spek, *Acta Crystallographica Section D* **65** (2009) (2) 148.
[82] D. Alfè, G.A. de Wijs, G. Kresse, M.J. Gillan, *International Journal of Quantum Chemistry* **77** (2000) (5) 871.
[83] P.G. Sundell, M.E. Björketun, G. Wahnström, *Physical Review B* **73** (2006) (10) 104112.
[84] C. Freysoldt, B. Grabowski, T. Hickel, J. Neugebauer, G. Kresse, A. Janotti, C.G. Van de Walle, *Reviews of modern physics* **86** (2014) (1) 253.
[85] F. Oba, M. Choi, A. Togo, I. Tanaka, *Science and Technology of Advanced Materials* **12** (2011) (3) 034302.
[86] S. Lany, A. Zunger, *Physical Review B* **78** (2008) (23) 235104.
[87] G. Kresse, J. Hafner, *Phys. Rev. B: Condens. Matter* **48** (1993) 13115.
[88] S. Nosé, *The Journal of Chemical Physics* **81** (1984) (1) 511.
[89] Y. Choi, D.S. Mebane, M.C. Lin, M. Liu, *Chem. Mater.* **19** (2007) (Copyright (C) 2011 American Chemical Society (ACS). All Rights Reserved.) 1690.
[90] A. Magrasó, R. Haugsrud, *Journal of Materials Chemistry A* **2** (2014) (32) 12630.
[91] A. Magraso, J.M. Polfus, C. Frontera, J. Canales-Vazquez, L.-E. Kalland, C.H. Hervoches, S. Erdal, R. Hancke, M.S. Islam, T. Norby, R. Haugsrud, *J. Mater. Chem.* **22** (2012) 1762.
[92] A. Magrasó, C.H. Hervoches, I. Ahmed, S. Hull, J. Nordström, A.W.B. Skilbred, R. Haugsrud, *Journal of Materials Chemistry A* **1** (2013) (11) 3774.
[93] T. Mori, J. Drennan, J.-H. Lee, J.-G. Li, T. Ikegami, *Solid State Ionics* **154-155** (2002) 461.

[94] M. Amsif, A. Magrasó, D. Marrero-López, J.C. Ruiz-Morales, J. Canales-Vázquez, P. Núñez, *Chemistry of Materials* **24** (2012) (20) 3868.
[95] C.E. Mohn, N.L. Allan, C.L. Freeman, P. Ravindran, S. Stolen, *J. Solid State Chem.* **178** (2005) (1) 346.
[96] E. Bakken, N.L. Allan, T.H.K. Barron, C.E. Mohn, I.T. Todorov, S. Stølen, *Physical Chemistry Chemical Physics* **5** (2003) (11) 2237.
[97] A. Tarancón, A. Morata, F. Peiró, G. Dezanneau, *Fuel Cells* **11** (2011) (1) 26.
[98] R. Hancke, *PCCP. Physical chemistry chemical physics* **14** (2012) (40) 13971.
[99] T. Norby, O. Dyrlie, P. Kofstad, *Solid State Ionics* **53-56** (1992) 446.
[100] M. Nagao, H. Hamano, K. Hirata, R. Kumashiro, Y. Kuroda, *Langmuir* **19** (2003) (22) 9201.
[101] S. Cheng, Master thesis, *Department of Physics*, University of Oslo, Oslo (2012).
[102] K.E.J. Eurenius, E. Ahlberg, C.S. Knee, *Dalton Transactions* **40** (2011) (15) 3946.
[103] T. Norby, O. Dyrlie, P. Kofstad, *Journal of the American Ceramic Society* **75** (1992) (5) 1176.